UNIVERSITY OF CALIFORNIA SAN DIEGO

Continuous monitoring of deep tissue with a stretchable ultrasonic patch

A dissertation submitted in partial satisfaction of the
requirements for the degree Doctor of Philosophy

in

Materials Science and Engineering

by

Hongjie Hu

Committee in charge:

Professor Sheng Xu, Chair
Professor Shengqiang Cai
Professor James Friend
Professor Tse Nga Ng
Professor Michael T. Tolley

2021

The dissertation of Hongjie Hu is approved, and it is acceptable in quality and form for publication on microfilm and electronically.

University of California San Diego

2021

TABLE OF CONTENTS

DISSERTATION APPROVAL PAGE iii

TABLE OF CONTENTS iv

LIST OF FIGURES vi

ACKNOWLEDGMENTS x

VITA xv

ABSTRACT OF THE DISSERTATION xviii

Chapter 1. The Development of The Stretchable Ultrasonic Array 1

1.1 Current Chanllenges in Ultrasonic Inspection Field. 1

1.2 Current Research in Flexible Ultrasonic Probes. 2

1.3 Design of The Stretchable Ultrasonic Array for Non Destructive Evaluation. 4

1.4 Design of The Stretchable Ultrasonic Array for Blood Pressure Waveform Monitoring. 9

1.5 Design of The Stretchable Ultrasonic Array for Tissue imaging. 13

1.6 Conclusion. 17

Chapter 2. The Characterization of The Stretchable Ultrasonic Array. 19

2.1 Acoustic Performance Characterization. 19

2.2 Mechanical Performance Characterization. 26

2.3 Characterization of Elastography. 31

2.4 Conclusion. 39

Chapter 3. Applications in Non Destructive Evaluation. 41

3.1 Two-Dimensional Imaging on Complex Surfaces. 41

3.2 Three-Dimensional Imaging on Complex Surfaces. 44

3.3 Conclusion. 46

Chapter 4. Applications on Monitoring of Human Vital Signs. 48

4.1 Motivation of The Central Blood Pressure Waveform. 48

4.2 Three-Dimensional Mapping of Deep Tissue Modulus. 51

4.3 B-mode imaging of the deep tissue and organs 73

4.4 Conclusion 75

Chapter 5. Summary 77

References 79

LIST OF FIGURES

Figure 1. Schematics of the stretchable ultrasonic transducer array. 5

Figure 2. Exploded view to illustrate each component in an element. 5

Figure 3. The optical image of four elements, showing the morphology of the piezoelectric material and bottom electrodes. 6

Figure 4. The optical image of four elements, showing the morphology of the backing layer and top electrodes. 6

Figure 5. Optical images of this stretchable device when bent around a developable surface, wrapped on a nondevelopable surface, and in a mixed mode of folding, stretching, and twisting, showing its mechanical robustness. 9

Figure 6. The device conforming to complex surfaces, demonstrating the mechanical compliance and robustness of the device. 10

Figure 7. Schematics of the stretchable ultrasonic device, with key components labelled. 11

Figure 8. Schematics of the stretchable ultrasonic array laminated on a soft tissue. 14

Figure 9. Resonant frequency, anti-resonant frequency, and calculated effective electromechanical coupling coefficient (K_{eff}) distribution of the elements (inset). 15

Figure 10. Evaluation of crosstalk between two adjacent elements and two alternate elements.. 16

Figure 11. Insertion loss of the transducers with and without the matching circuit. 17

Figure 12. The impedance and phase angle spectra of the 1-3 composite before and after processing, showing good electromechanical coupling of the fabricated transducer (k_{eff}~0.60; θ~50°). 20

Figure 13. Pulse-echo response and frequency spectra, with a short spatial pulse length (~1.94 ms), a high SNR (~20.24 dB), and a wide bandwidth (~47.11%). 21

Figure 14. The resonance and antiresonance frequency variations of the 100 transducer elements. 21

Figure 15. Average cross-talk levels between elements that are adjacent, two elements away, and three elements away, showing the outstanding anti-interference capacity of the device. 22

Figure 16. Schematics of spatial resolution measurement setup, with focal lengths of 20, 32, 37, and 52 mm, respectively. 23

Figure 17. Comparison of noise floors reconstructed by DMAS and DAS algorithms, revealing the benefits of the DMAS algorithm with only 0.01% energy ratio of noise to the reflector..... 24

Figure 18. Images of wire phantom combining the four tests with different *f* numbers, showing the capability of focusing at different depths and obtaining high resolution images. 24

Figure 19. Axial line spread functions for the center wire at different focal lengths. Resolution is defined as the line spread function width at an intensity of -6 dB..... 25

Figure 20. Lateral line spread functions for the center wire at different focal lengths..... 26

Figure 21. Experimental (Exp.) and simulation (Simu.) results of lateral and axial resolutions.. 26

Figure 22. The optical image (left) and corresponding finite element analysis (FEA) simulation (right) of a 2 × 2 array under 50% biaxial tensile strain, showing its excellent stretchability. 28

Figure 23. The optical image after releasing the biaxial strain of 50%. 28

Figure 24. Experimental and simulation results of a small array under biaxial tensile strain. 29

Figure 25. Electrical impedances of the transducer under different strain levels, showing the mechanical stability of the device..... 30

Figure 26. Electrical impedances under different bending curvatures. 30

Figure 27. Relative resistance changes of Cu serpentine under stretching..... 31

Figure 28. The device conforming to non-developable surfaces and under mixed modes of stretching and twisting. 31

Figure 29. Comparison of three different transmission modes..... 33

Figure 30. Simulations showing the SNR_e and CNR_e of the coherent plane wave compounding, mono-focus, and single plane wave transmission modes in a bilayer phantom. 34

Figure 31. The SNRe as a function of the step size of the steering angle. 34

Figure 32. The SNR_e and reconstruction time with different numbers of steering angles. 35

Figure 33. Factors affecting the step size and number of the compounding angle..... 35

Figure 34. Processing time for reconstructing images at different angle numbers..... 36

Figure 35. The SNR_e and normalized correlation coefficient (NCC) as 158 a function of applied strain. The shaded area with >0.8 NCC by a -3 dB strain filter shows the dynamic range. 37

Figure 36. Lateral and axial resolutions of the stretchable ultrasonic array based on the full width at half maximum (FWHM) of point spread functions (PSF). 37

Figure 37. Quantification of the contrast resolution based on the relationship between the CNR_e and modulus contrast of phantoms. 38

Figure 38. Two-dimensional images of a linear defect under complex surfaces..... 42

Figure 39. Reconstructed images based on simulation under flat, concave, and convex surfaces. 43

Figure 40. Schematics of the experimental setup, illustrating the spatial location and relative orientation of the two defects in the test subject. 45

Figure 41. The pulse-echo signal and 2D image of the two defects. 45

Figure 42. The reconstructed 3D image, showing complete geometries of the two defects. 46

Figure 43. The 3D image from different view angles, showing the relative positions and orientations of the two defects to the top surface, which match the design well. 46

Figure 44. Blood pressure measurements from the central to peripheral arteries and validation using a commercial tonometer. 49

Figure 45. Fabrication processes and optical images of tissue-mimic phantoms. 50

Figure 46. Characterizations on phantom models..... 53

Figure 47. Illustration of the normalized cross-correlation and least-squares strain estimator algorithms. 54

Figure 48. Displacement and strain curves at the central lines of different phantoms. 56

Figure 49. 3D strain images of an inclusion phantom by the stretchable and commercial ultrasonic probes. 57

Figure 50. 3D strain images of the commercial breast phantom by the stretchable and commercial ultrasonic probes. 58

Figure 51. Repetitive tests..... 59

Figure 52. Flow chart of the process for calculating the inverse elasticity problem. 60

Figure 53. The L-curve of calculating the inverse elasticity problem. 61

Figure 54. A 3D quantitative elastographic image of a porcine abdominal tissue by the stretchable ultrasonic array. 62

Figure 55. The averaged 3% discrepancy of the 16 pairs of measured and predicted displacement fields, with a high degree of correspondence between the reconstructed mechanical model by solving the inverse elasticity problem and the experimental conditions, suggesting a robust foundation for yielding the accurate modulus distributions. 63

Figure 56. A 3D MRE image of the porcine abdominal tissue..... 63

Figure 57. Bland-Altman analysis of the strain contrast of a commercial breast phantom for eight weeks..... 64

Figure 58. Serial monitoring of the modulus evolution of a bovine gluteobiceps muscle. 65

Figure 59. Time-dependent stiffness variation of a piece of bovine gluteobiceps muscle under heating..... 67

Figure 60. Multi-site mapping in human. 67

Figure 61. A 3D elastographic reconstruction of the upper arm..... 69

Figure 62. Soreness visual analog scale and testing protocol..... 70

Figure 63. Serial monitoring results of normalized modulus contrast and soreness intensity of the biceps brachii muscle before and after the eccentric exercise. 71

Figure 64. Coefficient of variation among all tests..... 72

Figure 65. Optical images of skin before and after monitoring..... 72

Figure 66. B-mode images of abdominal aorta from longitudinal view from both commercial and wearable ultrasonic probes..... 74

Figure 67. B-mode images of abdominal aorta from cross view from both commercial and wearable ultrasonic probes..... 74

Figure 68. B-mode images of liver from both commercial and wearable ultrasonic probes..... 75

ACKNOWLEDGMENTS

First, I would express my deepest and heartiest appreciation to my advisor Professor Sheng Xu, for allowing me to join the group five years ago, for leading me on the road of scientific research, for training my research skill, cultivating my critical thinking, and broadening my horizon. His rigorous attitude, profound knowledge, deep understanding, far-sighted vision, fiery passion, and admirable courage show me what a true scholar should be. As my role model, Professor Xu motivates me all the time to keep improving myself and to become a scientist like him one day in the future. It's my great honor to get training from him in my Ph.D. career. I hope my performance does live up to his opportunity once he gave me.

Second, I would like to thank Professor Shengqiang Cai, Professor James Friend, Professor Michael Tolley, Professor Tse Nga Ng, Professor Francesco Lanza di Scalea, Professor Matt Pharr, Professor Qifa Zhou, and Professor Assad Oberai for their precious suggestions, comments and support to my research projects. I would also like to provide my sincere appreciation to Dr. Zhe Wu, Dr. Ruimin Chen, Dr. Xuan (Peter) Zhu, and Dr. Dawei Song for selflessly sharing the guidance and experience without any reservation.

Third, I am very grateful to my team members, Yuxiang Ma, Mohan Li, Hao Huang, Ruixiang Qi, and Ray Wu, who helped me a lot in experiment designing, device fabrication, data collection and processing, problem debugging, and manuscript drafting. Those projects could not

have been done without their tremendous contributions. The happiest time in my Ph.D. career is when I do experiments with them.

Fourth, I would like to specially acknowledge my dear friends: Dr. Yue Gu, Dr. Chunfeng Wang, Dr. Yimu Chen, Dr. Yusheng Lei, Mr. Yang Li, Dr. Zhenlong Huang, Dr. Rui Kou, Dr. Qiguang He, Mr. Yang Wang, Mr. Lu Yin, Mr. Fangyu Zhang, Dr. Naiqing Zhang, Dr. Yangyucheng Yang, Dr. Haowen Ren, et al. I will always remember the time and unconditional efforts you spent on my research projects. I believe our friendship will last forever.

Fifth, I will also thank my labmates for the countless discussion and collaborations: Dr. Xiaoxiang Gao, Mr. Xiangjun Chen, Dr. Hong Ding, Dr. Lin Zhang, Mr. Muyang Lin, Mr. Sai Zhou, Mr. Zhiyuan Lou, Mr. Yitian Tong, Mr. Chengchangfeng Lu, Dr. Yangzhi Zhu et al.

Last but not least, I would like to thank my parents for raising me up, providing me with good educational environment, and supporting me to go abroad. I would like to thank my grandparents who are in their eighties, for their endless love and care to me for almost thirty years. Having away from my country over six years, their encouragement and concern have always been my power source all the time, which soothes my heart wounds, strengthens my faith, and pushes me moving forward. No word can express my deep gratitude to them. I would like to say thank you to my family and relatives. Your unconditional love and help truly make me feel lucky to grow up in such an ordinary but warm home.

Chapter One, in full, is a partial reprint of the materials: ‘Stretchable ultrasonic transducer arrays for three-dimensional imaging on complex surfaces, Hu, H., Zhu, X., Wang, C., Zhang, L.,

Li, X., Lee, S., Huang, Z., Chen, R., Chen, Z., Wang, C., Gu, Y., Chen, Y., Lei, Y., Zhang, T., Kim, N., Guo, Y., Teng, Y., Zhou, W., Li, Y., Nomoto, A., Sternini, S., Zhou, Q., Pharr, M., Lanza di Scalea, F., Xu, S., Science advances, 4.3 (2018): eaar3979'; 'Monitoring of the central blood pressure waveform via a conformal ultrasonic device, Wang, C., Li, X., Hu, H., Zhang, L., Huang, Z., Lin, M., Zhang, Z., Yin, Z., Huang, B., Gong, H., Bhaskaran, S., Gu, Y., Makihata, M., Guo, Y., Lei, Y., Chen, Y., Wang, C., Li, Y., Zhang, T., Chen, Z., Pisano, A., Zhang, L., Zhou, Q., Xu, S., Nature biomedical engineering 2.9 (2018): 687-695'; 'Three-dimensional mapping of deep tissue modulus by stretchable ultrasonic arrays, Hu, H., Ma, Y., Gao, X., Song, D., Li, M., Huang, H., Qian, X., Shi, K., Ding, H., Lin, M., Chen, X., Zhao, W., Qi, B., Zhou, Sai; Chen, R., Gu, Y., Chen, Y., Lei, Y., Wang, C., Wang, C., Tong, Y., Cui, H., Zhu, Y., Tian, X., Chen, Z., Lu, C., Eghtedari, M., Zhou, Q., Oberai, A., Xu, S., Submitted'; 'Soft wearable devices for deep tissue sensing, Lin, M., Hu, H., Zhou, S., Xu, S., Accepted'. The dissertation author was the first or co-first author of these papers.

Chapter Two, in full, is a partial reprint of the materials: 'Stretchable ultrasonic transducer arrays for three-dimensional imaging on complex surfaces, Hu, H., Zhu, X., Wang, C., Zhang, L., Li, X., Lee, S., Huang, Z., Chen, R., Chen, Z., Wang, C., Gu, Y., Chen, Y., Lei, Y., Zhang, T., Kim, N., Guo, Y., Teng, Y., Zhou, W., Li, Y., Nomoto, A., Sternini, S., Zhou, Q., Pharr, M., Lanza di Scalea, F., Xu, S., Science advances, 4.3 (2018): eaar3979'; 'Monitoring of the central blood pressure waveform via a conformal ultrasonic device, Wang, C., Li, X., Hu, H., Zhang, L., Huang, Z., Lin, M., Zhang, Z., Yin, Z., Huang, B., Gong, H., Bhaskaran, S., Gu, Y., Makihata, M., Guo,

Y., Lei, Y., Chen, Y., Wang, C., Li, Y., Zhang, T., Chen, Z., Pisano, A., Zhang, L., Zhou, Q., Xu, S., Nature biomedical engineering 2.9 (2018): 687-695'; 'Three-dimensional mapping of deep tissue modulus by stretchable ultrasonic arrays, Hu, H., Ma, Y., Gao, X., Song, D., Li, M., Huang, H., Qian, X., Shi, K., Ding, H., Lin, M., Chen, X., Zhao, W., Qi, B., Zhou, Sai; Chen, R., Gu, Y., Chen, Y., Lei, Y., Wang, C., Wang, C., Tong, Y., Cui, H., Zhu, Y., Tian, X., Chen, Z., Lu, C., Eghtedari, M., Zhou, Q., Oberai, A., Xu, S., Submitted'. The dissertation author was the first or co-first author of these papers.

Chapter Three, in full, is a partial reprint of the materials: 'Stretchable ultrasonic transducer arrays for three-dimensional imaging on complex surfaces, Hu, H., Zhu, X., Wang, C., Zhang, L., Li, X., Lee, S., Huang, Z., Chen, R., Chen, Z., Wang, C., Gu, Y., Chen, Y., Lei, Y., Zhang, T., Kim, N., Guo, Y., Teng, Y., Zhou, W., Li, Y., Nomoto, A., Sternini, S., Zhou, Q., Pharr, M., Lanza di Scalea, F., Xu, S., Science advances, 4.3 (2018): eaar3979'. The dissertation author was the first author of this paper.

Chapter four, in full, is a partial reprint of the materials: 'Monitoring of the central blood pressure waveform via a conformal ultrasonic device, Wang, C., Li, X., Hu, H., Zhang, L., Huang, Z., Lin, M., Zhang, Z., Yin, Z., Huang, B., Gong, H., Bhaskaran, S., Gu, Y., Makihata, M., Guo, Y., Lei, Y., Chen, Y., Wang, C., Li, Y., Zhang, T., Chen, Z., Pisano, A., Zhang, L., Zhou, Q., Xu, S., Nature biomedical engineering 2.9 (2018): 687-695'; 'Three-dimensional mapping of deep tissue modulus by stretchable ultrasonic arrays, Hu, H., Ma, Y., Gao, X., Song, D., Li, M., Huang, H., Qian, X., Shi, K., Ding, H., Lin, M., Chen, X., Zhao, W., Qi, B., Zhou, Sai; Chen, R., Gu, Y.,

Chen, Y., Lei, Y., Wang, C., Wang, C., Tong, Y., Cui, H., Zhu, Y., Tian, X., Chen, Z., Lu, C., Eghtedari, M., Zhou, Q., Oberai, A., Xu, S., Submitted'. The dissertation author was the co-first author of these papers.

VITA

2015 Bachelor of Science in Applied Chemistry

University of Science and Technology Beijing

2016 Master in Materials Science and Engineering

University of California San Diego

2021 Doctor of Philosophy in Materials Science and Engineering

University of California San Diego

PUBLICATIONS

(* authors contributed equally to the work)

Hu, H.*, Zhu, X.*****, Wang, C.*****, Zhang, L.*****, Li, X., Lee, S., Huang, Z., Chen, R., Chen, Z., Wang, C., Gu, Y., Chen, Y., Lei, Y., Zhang, T., Kim, N., Guo, Y., Teng, Y., Zhou, W., Li, Y., Nomoto, A., Sternini, S., Zhou, Q., Pharr, M., Scalea, F,. Xu, S., "Stretchable ultrasonic transducer arrays for three-dimensional imaging on complex surfaces", Science Advances, 2018, 4(3), eaar3979.

Wang, C.*****, Li, X.*****, **Hu, H.***, Zhang, L., Huang, Z., Lin, M., Zhang, Z., Yin, Z., Huang, B., Gong, H., Bhaskaran, S., Gu, Y., Makihata, M., Guo, Y., Lei, Y., Chen, Y., Wang, C., Li, Y., Zhang, T., Chen, Z., Pisano, A., Zhang, L., Zhou, Q., Xu, S., "Monitoring of the central blood pressure waveform via a conformal ultrasonic device", Nature Biomedical Engineering, 2018, 2(9), 687.

Yang, Y.*****, **Hu, H.***, Chen, Z.*****, Wang, Z., Jiang, L., Lu, G., Li, X., Chen, R., Jin, J., Kang, H., Chen, H., Lin, S., Xiao, S., Zhao, H., Xiong, R., Shi, J., Zhou, Q., Xu, X., Chen, Y., "Stretchable nanolayered thermoelectric energy harvester on complex and dynamic surfaces", Nano letters 20.6 (2020): 4445-4453.

Lin, M.*****, **Hu, H.***, Zhou, S.*****, "Soft wearable devices for deep tissue sensing", Nature Reviews Materials, accepted.

Hu, H.*, Ma, Y.*, Gao, X.*, Song, D.*, Li, M., Huang, H., Qian, X., Shi, K., Ding, H., Lin, M., Chen, X., Zhao, W., Qi, B., Zhou, S., Chen, R., Gu, Y., Chen, Y., Lei, Y., Wang, C., Wang, C., Tong, Y., Cui, H., Zhu, Y., Tian, X., Chen, Z., Lu, C., Eghtedari, M., Zhou, Q., Oberai, A., Xu, S., Nature Biomedical Engineering, submitted.

Gao, X.*, Chen, X.*, **Hu, H.***, Wang, X.*, Mu, J., Lou, Z., Zhang, R., Shi, K., Yue, W., Chen, X., Lin, M., Qi, B., Zhou, S., Lu, C., Gu, Y., Ding, H., Zhu, Y., Huang, H., Ma, Y., Li, M., Mishra A., Xu, S., Nature Elecronics, submitted.

Lei, Y.*****, Chen, Y.*, Zhang, R., Li, Y., Yan, Q., Lee, S., Yu, Y., Tsai, H., Choi, W., Wang, K., Luo, Y., Gu, Y., Zheng, X., Wang, C., Wang, C., **Hu, H.**, Li, Y., Qi, B., Lin, M., Zhang, Z., Dayeh. S., Pharr, M., Fenning, D., Lo, Y., Luo, J., Yang, K., Yoo, J., Nie, W., Xu, S., "A fabrication process for flexible single-crystal perovskite devices", Nature, 2020, 583, 790-795.

Chen, Y.*, Lei, Y.*****, Li, Y., Yu, Y., Cai, J., Chiu, M., Rao, R., Gu, Y., Wang, C., Choi, W., **Hu, H.**, Wang, C., Li, Y., Song, J., Zhang, J., Qi, B., Lin, M., Zhang, Z., Islam, A., Maruyama, B., Dayeh, S., Li, L., Yang, K., Lo, Y., Xu, S., "Strain Engineering and Epitaxial Stabilization of Halide Perovskites", Nature, 2020, 577, 209.

Lei, Y.*****, Chen, Y.*, Gu, Y., Wang, C., Huang, Z., Qian, H., Nie, J., Hollett, G., Choi, W., Yu, Y., Kim, N., Wang, C., Zhang, T., **Hu, H.**, Zhang, Y., Li, X., Li, Y., Shi, W., Liu, Z., Sailor, M. J., Dong, L., Lo, Y.-H., Luo, J., Xu, S., "Controlled Homoepitaxial Growth of Hybrid Perovskites", Advanced Materials, 2018, 30, 1705992.

Huang, Z.*****, Hao, Y.*****, Li, Y.*****, **Hu, H.**, Wang, C., Nomoto, A., Pan, T., Gu, Y., Chen, Y., Zhang, T., Li, W., Lei, Y., Kim, N., Wang, C., Zhang, L., Ward, J., Maralani, A., Li, X., Durstock, M., Pisano, A., Lin, Y., Xu, S., "Three-dimensional integrated stretchable electronics", Nature Electronics, 2018, 1(8), 473.

Wang, C.*****, Qi, B.*****, Lin, M.*****, Zhang, Z.*****, Makihata, M., Liu, B., Zhou, S., Huang, Y., **Hu, H.**, Gu, Y., Chen, Y., Lei, Y., Lee, T., Chien, S., Jang, K., Kistler, E., Xu, S., "Continuous monitoring of deep-tissue haemodynamics with stretchable ultrasonic phased arrays", Nature Biomedical Engineering 5.7 (2021): 749-758.

Chen, X.*****, Gao, X.*****, Nomoto, A.*****, Shi, K., Lin, M., **Hu, H.**, Gu, Y., Zhu, Y., Wu, Z., Chen, X., Wang, X., Qi, B., Zhou, S., Ding, H., Xu, S., "Fabric-substrated capacitive biopotential sensors enhanced by dielectric nanoparticles", Nano Research (2021): 1-5.

ABSTRACT OF THE DISSERTATION

Continuous monitoring of deep tissue with a stretchable ultrasonic patch

By

Hongjie Hu

Doctor of Philosophy in Materials Science and Engineering

University of California San Diego, 2021

Professor Sheng Xu, Chair

Ultrasonic imaging has been implemented as a powerful tool for noninvasive subsurface inspections of both structural and biological media. Current ultrasound probes are rigid and bulky and cannot readily image through nonplanar three-dimensional (3D) surfaces. However, imaging through these complicated surfaces is vital because stress concentrations at geometrical

discontinuities render these surfaces highly prone to defects. From the aspect of monitoring discontinuities render these surfaces highly prone to defects. From the aspect of monitoring of the human vital signs, although current ultrasonic technologies allow non-invasive deep tissue observation, unstable coupling with the tissue surface resulting from the bulkiness and rigidity of conventional ultrasound probes introduces usability constraints.

Based on those motivations, reports a stretchable ultrasound probe that can conform to and detect nonplanar complex surfaces. The probe consists of a large array of piezoelectric transducers that exploit an “island-bridge” layout with multilayer electrodes, encapsulated by thin and compliant silicone elastomers. The stretchable device can conform to the nonplanar surfaces of industrial components or human skin and enables non-invasive, continuous and accurate testing, which should facilitate its use in a variety of structural health monitoring and clinical environments.

In Chapter One, the introduction of the stretchable ultrasonic device and the current problems presented in this field will be introduced and discussed. The probe design and fabrication for different applications are introduced. Our work presents the first stretchable ultrasonic arrays for different types of measurement and monitoring. In Chapter Two, the acoustic and mechanical properties of the device will be introduced. Performances of the device for elastography and B-mode imaging will also be explained in detail. In Chapter Three, the first application of the device for nondestructive evaluation will be demonstrated. The device performance is demonstrated by reconstructing defects in 3D space with high spatial resolution through flat, concave, and convex surfaces. The results hold great implications for applications of ultrasound that require imaging

through complex surfaces. In Chapter Four, a variety of applications for monitoring of human vital signs, such as blood pressure waveform, tissue stiffness, and organ anatomy, are demonstrated, which opens up opportunities for wearable diagnostics in a variety of clinical environments.

Chapter 1. The Development of The Stretchable Ultrasonic Array.

1.1 Current Challenges in Ultrasonic Inspection Field.

Ultrasound imaging technologies have been widely used to visualize internal discontinuities in objects for nondestructive evaluation, structural health monitoring, and medical diagnosis because of their noninvasiveness, high accuracy, great sensitivity, and strong penetration capabilities[1,2]. Ultrasound probes with flat bases have been created to successfully accommodate different components of planar surfaces. However, these rigid probes cannot achieve a solid interfacial contact and therefore good coupling with irregular nonplanar surfaces, which are ubiquitous in real objects. Air gaps at these interfaces lead to large acoustic energy reflections and wave distortions, thereby creating unreliable testing results[3]. Ultrasonic couplants, such as water and gel, are typically used to remove the air gaps. However, an abundant use of the couplants will lead to a high-pass filter effect of the ultrasonic signals, causing significant canceling of small response echoes. Furthermore, extensive use of the couplants will bring about an ~80% incident energy transmission loss at the interface between the couplant and the subject because of the significant mismatch of their acoustic impedances[4]. In addition, these rigid and bulky probes cannot be applied to hard-to-reach locations such as small cavities and slits. Thus, components at these locations normally have to be disassembled for a reliable diagnosis. At the same time, the stress concentrations present at the geometrical discontinuities of load-bearing objects make these region particularly prone to defects[5]. Although many methods have been reported to solve this

interfacial coupling problem[6,7], a number of disadvantages of the existing approaches remain, such as limited specimen size[8], demanding probe offset[9], and bulky probe housing[10], all of which compromise the feasibility of in situ detection, detection accuracy and sensitivity, and operation convenience of ultrasonic measurements.

1.2 Current Research in Flexible Ultrasonic Probes.

Recent efforts have focused on developing flexible ultrasonic probes that can be divided into three main categories: using organic piezoelectric films as transducers, embedding piezoelectric ceramic into polymer substrates, and fabricating micromachined ultrasonic transducers. The organic piezoelectric films have good flexibility. However, the polymer piezoelectrets, typically polyvinylidene fluoride and its copolymer films[11], are not suitable to serve as transmitters because of their low electromechanical coupling coefficients (a parameter that characterizes the coupling between electrical energy and mechanical energy), low dielectric constants, and high dielectric losses[12]. Moreover, their low Curie points make them difficult to process, and high-temperature applications result in phase transformations, which completely degrade the piezoelectric properties[13]. The piezoelectric ceramics produce superior electromechanical performance and ease of processing. However, they cannot conform to curved surfaces without external forces because of the large elastic moduli of substrates[14,15]. The external force, usually applied manually, is often inconsistent. As a result, noise or even artifacts in the acquired pulse-echo signals can arise because of variations of the coupling conditions at the

transducer-specimen interface. Moreover, for some applications related to long-term structural condition monitoring, such as fatigue crack growth at hidden or hard-to-access places of aircrafts and steamboats, the mechanical robot cannot support the testing[16]. Micromachined transducers rely on the bending motion of a thin membrane, enabling a thin device profile and flexibility, but at the cost of electromechanical coupling properties. Both capacitive and piezoelectric micromachined transducers have been designed. In capacitive micromachined transducers[17,18], a membrane is attracted by an electrostatic force; the mechanical restoring force of the membrane resists deformation, which limits the vibration amplitude and thus the energy conversion efficiency. In piezoelectric micromachined transducers, a bi-layer unimorph structure[19,20] is composed of an active piezoelectric layer, working in d_{31} mode to provide actuation, and a passive layer, creating strain asymmetry along the thickness of the device. The passive layer cannot convert mechanical energy into electrical energy or vice versa[21], which compromises device sensitivity.

Flexible ultrasonic arrays can bend over developable surfaces (for example, a cylindrical surface)[22-24]; however, the human body surface is nondevelopable, which can lead to gaps between the arrays and the skin. Alternatively, stretchable ultrasonic arrays[25-28] can better adapt to the surface of the human body. Here, stretchable ultrasonic arrays are designed by integrating high-performance piezoelectric materials with an island-bridge structure. The islands are then interconnected by serpentine-shaped metallic bridges, followed by encapsulation in thin elastomers[28]. The serpentine conductive network offers >50% biaxial stretchability with minimal impact on transducer performance, enabling intimate contact with nondevelopable surfaces[27].

1.3 Design of The Stretchable Ultrasonic Array for Non Destructive Evaluation.

The schematic device structure is shown in Figure. 1. The piezoelectric transducers are arranged in a 10 × 10 array, connected by an island-bridge structured matrix. Each island hosts a rigid element. The wavy bridges can unfold to accommodate the externally applied strain, with limited strain in the components themselves. Therefore, the matrix is rigid locally but soft globally. Each element in the array is individually addressable. The soft probe can consequently reconstruct the target morphology in multi-section images. Figure 2 shows the exploded view of one element. Both the substrate and superstrate are silicone elastomer thin films, whose low modulus (~70 kPa) and large stretchability (~900%) offer an extremely compliant platform to accommodate a diverse class of building blocks, such as piezoelectric elements, metal interconnects, backing layers, and solder paste. The thickness of the elastomer substrate and superstrate is 15 mm to provide both high acoustic performance[29] and mechanical robustness of the device. The islands and bridges are patterned bilayers of Cu (20 mm)/polyimide (PI; 2 mm). The PI layer greatly enhances the bonding strength between the Cu and the elastomer. Piezoelectric 1-3 composites are chosen as the active material of the transducers (Fig. 3). Compared with an isotropic lead zirconate titanate (PZT), the anisotropic 1-3 composites have superior electromechanical coupling coefficients (thickness mode)

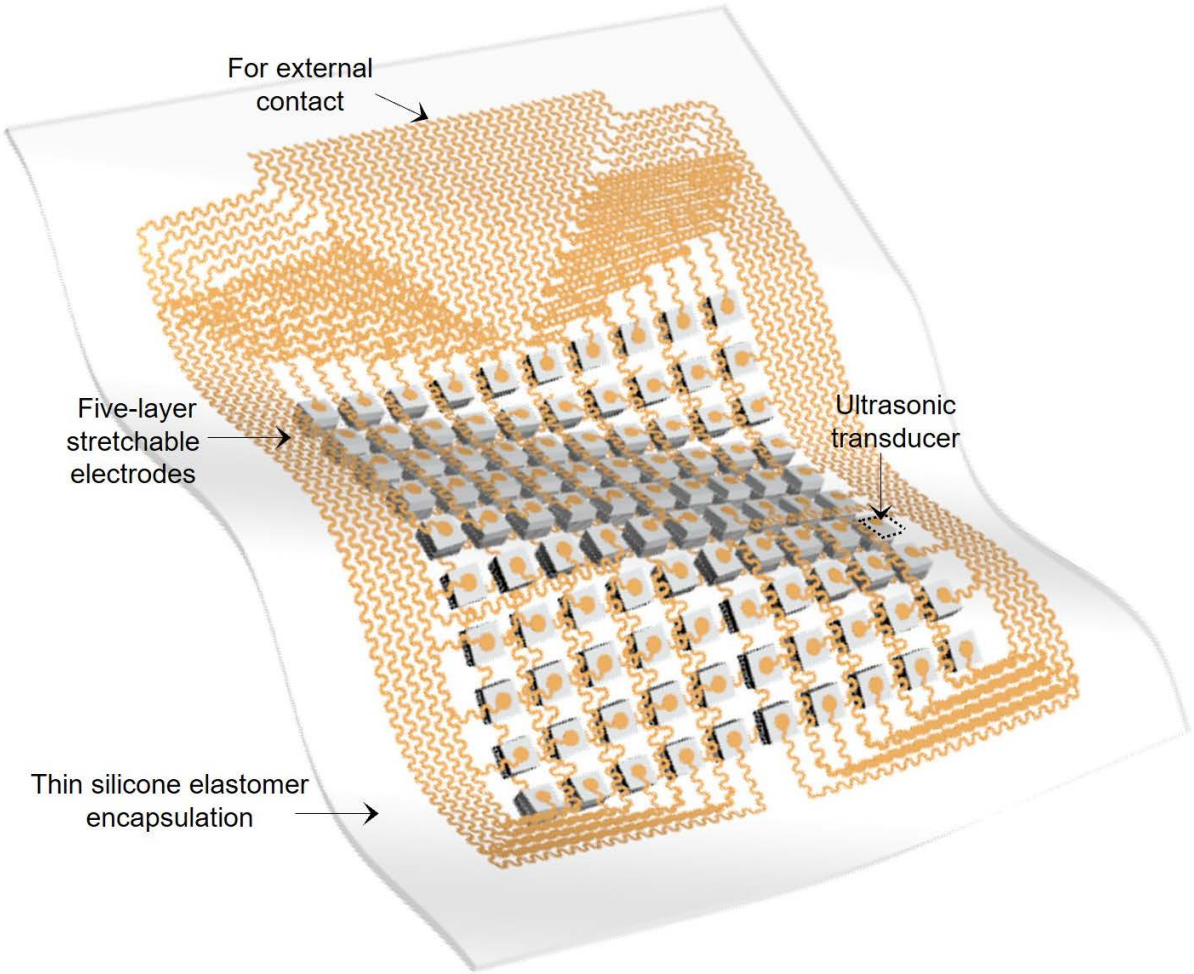

Figure 1. Schematics of the stretchable ultrasonic transducer array.

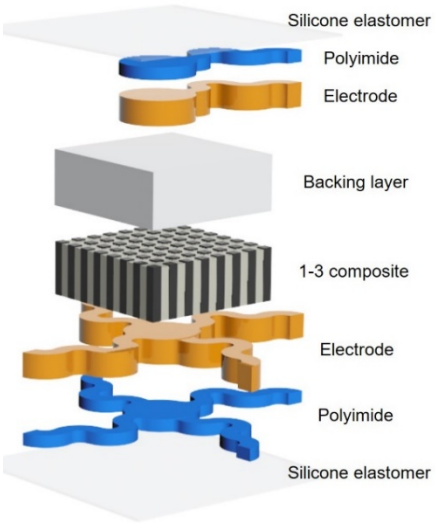

Figure 2. Exploded view to illustrate each component in an element.

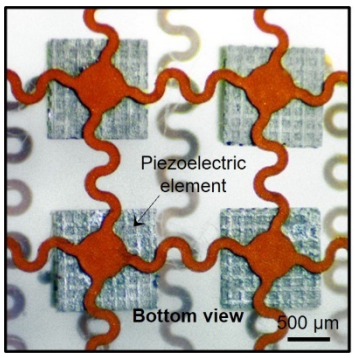

Figure 3. The optical image of four elements, showing the morphology of the piezoelectric material and bottom electrodes.

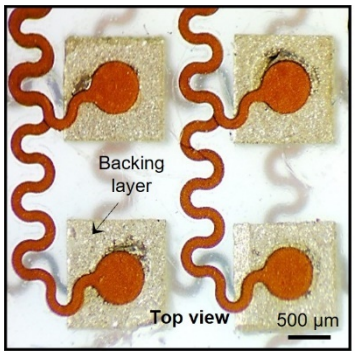

Figure 4. The optical image of four elements, showing the morphology of the backing layer and top electrodes.

that convert the majority of electrical energy to vibrational energy. In addition, the surrounding epoxy filler effectively suppresses transverse vibrations of PZT pillars[30], leading to enhanced longitudinal waves that go into the targeted objects. Molded blocks of a Ag-epoxy composite serve as the backing layer (Fig. 4). The backing layer effectively dampens the ringing effects (excessive vibrations) of the piezoelectrics, which shortens the spatial pulse length and broadens the bandwidth[31] and thus improves the image axial resolution. Ag epoxy and solder paste are used to build robust and electrically conductive 1-3 composite/backing layer and 1-3 composite/metal electrode interfaces, respectively. Because of the close acoustic impedances of the 1-3 composite

[~20 Mega-Rayleigh (MR)] and the targets to be tested (Al, ~18 MR), the matching layer is not necessary in this study[32,33].

On one hand, the pitch between adjacent transducer elements should be small to reduce side lobe and grating lobe artifacts in the acquired images[34]. On the other hand, sufficient space between the elements should be allocated to the serpentine interconnects for sufficient stretchability. A pitch of 2.0 mm (1.2 mm × 1.2 mm element footprint with a spacing of 0.8 mm) can achieve more than 30% reversible stretchability. The high spatial resolution (~610 mm), negligible cross-talk level between adjacent elements (~−70 dB), and artifact-free images validate this pitch design. Within these limited footprints, the island-bridge electrode layout design is critical, considering the large number of electrical connections needed for wiring the 10 × 10 array. An active multiplexing matrix under the ultrasound transducers could be a potential solution[24]. However, the structural support materials introduced by the multiplexing matrix will negatively affect device stretchability. Multilayered electrodes have been demonstrated[35], but the electrode design, passive dielectrics, and the substrate only makes the devices flexible, not stretchable. To individually address the 100 transducer elements, a minimum of 101 electrodes with a common ground electrode is needed. It is very challenging to place this large number of electrodes within limited footprints using conventional single-layer designs.

Thus, we invented a multilayered electrode design based on the “transfer printing” method, which greatly enhanced the level of device integration compared to single-layer designs. This design consists of five layers of “horseshoe”-configured serpentine electrodes. One electrode lies

at the bottom of the transducers as the common ground layer. The other 100 electrodes are well aligned and distributed into four layers on top of the transducers as stimulating electrodes. Thin films of silicone elastomer (35 mm thick) provide insulation and adhesion between adjacent layers. The central area of each layer is selectively protected using customized masks during fabrication to allow the islands (bonding pads) to be exposed to the array elements. Laser ablation is used to quickly pattern serpentine structures. This method has been mostly focused on rigid or flexiblevsubstrates, but has been seldom focused on silicone substrates for stretchable electronics. The challenges for using stretchable substrates are (i) controlling the laser power to fully ablate the pattern while avoiding the pattern delamination from the temporary PDMS substrate and (ii) tuning the surface tackiness of the temporary PDMS substrate to allow the subsequent transfer printing of the patterned electrodes. We solved these challenges and developed a fabrication protocol for stretchable electronics using laser ablation. Compared with microfabrication methods by lithography and etching[36,37], which require sophisticated fabrication processes, chemicals, shadow masks, and a clean room environment, laser ablation is time-efficient, low-cost, and offers high throughput. The as-fabricated final device is seen in Figure. 5, which highlights its excellent mechanical properties when conforming to developable (cylindrical) and nondevelopable (spherical) surfaces, and under mixed modes of folding, stretching, and twisting. The device can easily achieve conformal contact with various nonplanar surfaces of real components, such as pipeline elbows, wheel edges, and rail tracks. An anisotropic conductive film bonded to the Cu interconnects offers conductive access to external power supplies and data acquisition systems.

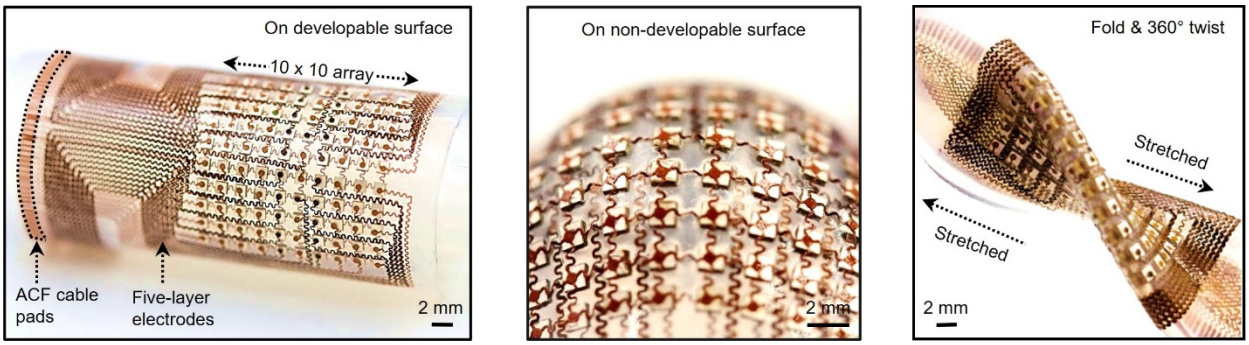

Figure 5. Optical images of this stretchable device when bent around a developable surface, wrapped on a nondevelopable surface, and in a mixed mode of folding, stretching, and twisting, showing its mechanical robustness.

1.4 Design of The Stretchable Ultrasonic Array for Blood Pressure Waveform Monitoring.

The device hybridizes high-performance rigid 1–3 piezoelectric composites with soft structural components. The anisotropic 1–3 composite possesses better acoustic coupling with the soft biological tissue than isotropic piezoelectric materials. By combining geometrical and electrical designs, our device can reach an ultrathin thickness of 240 μm, three orders of magnitude thinner than existing medical ultrasonic probes. The elastic and failure strain levels are up to 30% and 60%, respectively. The 1–3 piezoelectric composite with a thickness of 200 μm has a working frequency of 7.5 MHz, which enables a 400 μm axial resolution that is comparable with available medical ultrasonic probes at the same working frequency. The 1–3 composite has piezoelectric microrods embedded in a periodic configuration in a passive epoxy matrix, which substantially increases the longitudinal coupling coefficient k_{33} by suppressing shear vibrating modes. The rigid piezoelectric transducer element has a 0.9×0.9 mm^2 footprint to allow sufficient penetration depth into the tissue, while adding minimal mechanical loading to human skin (Fig. 6).

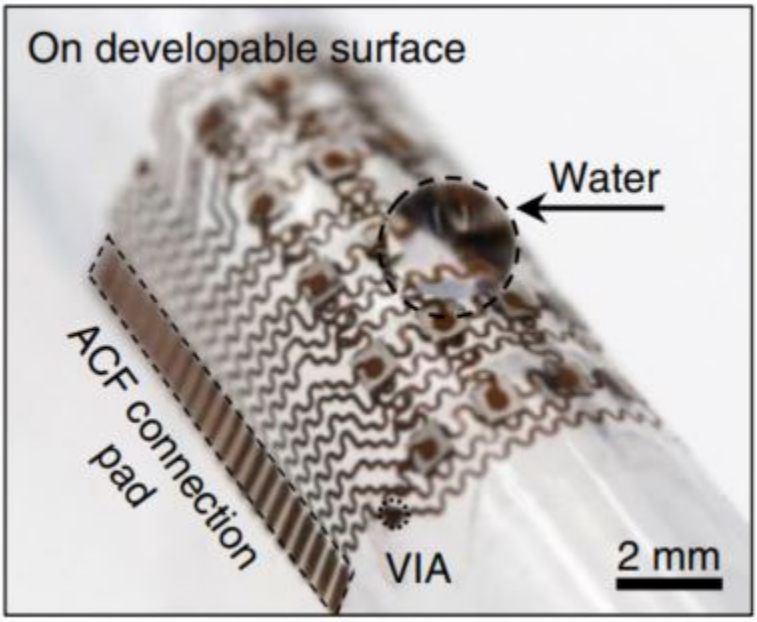

Figure 6. The device conforming to complex surfaces, demonstrating the mechanical compliance and robustness of the device.

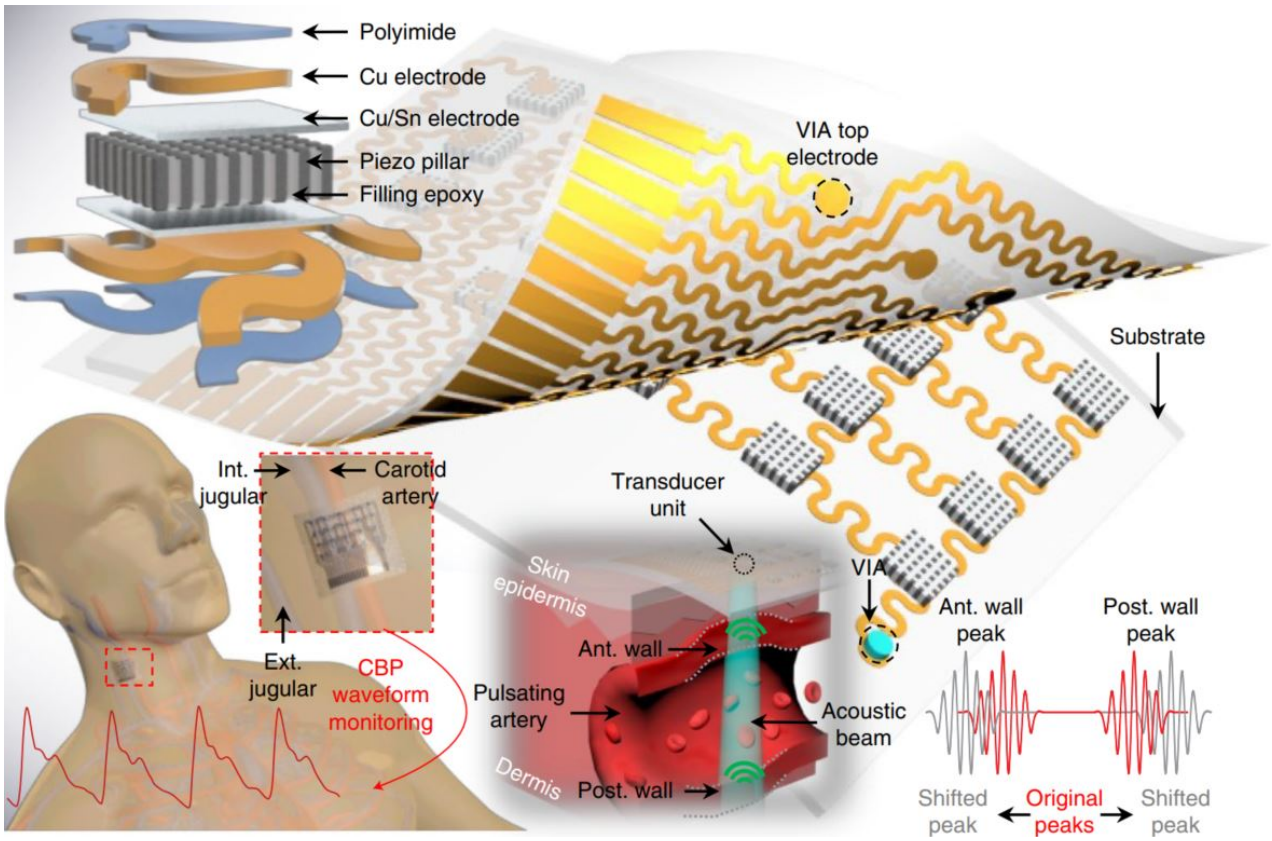

Figure 7. Schematics of the stretchable ultrasonic device, with key components labelled. The high-performance 1-3 composite with periodic piezoelectric rods embedded in an epoxy matrix suppresses shear vibration modes and enhances longitudinal ultrasonic penetration into the skin. The vertical interconnect access connects the top and bottom electrodes, allowing co-planar anisotropic conductive film bonding to the electrodes to enhance the robustness of the device. When mounted on the human neck, the device enables monitoring of CBP by capturing the pulsating vessel diameter of the carotid artery, internal jugular vein (int. jugular) and external jugular vein (ext. jugular) using the pulse-echo method, as illustrated in the bottom left graph. The device can locate the dynamic anterior (ant.) and posterior (post.) walls of the vessel using a high-directivity ultrasonic beam (bottom middle graph). The corresponding shifting echo radiofrequency signals reflected from the anterior and posterior walls are shown bottom right.

Bilayer stacking of polyimide (PI, 4μm)/Cu (20 μm) was used to fabricate stretchable electrodes to interconnect a 4×5 array of transducers in the device. The transducers can be individually addressed by 20 stimulating electrodes on the top and a common ground at the bottom. The array design aims to map the vessels' positions, thus enabling sensing and monitoring by a

transducer overlying the targeted vessel, without tedious manual positioning. The top simulating electrodes and the bottom ground are routed to the same plane by a vertical interconnect access for optimized mechanical robustness and ease of electrical bonding.

The working principle is illustrated in Figure 7 bottom. Technically, the device can continuously record the diameter of a pulsating blood vessel, which can be translated into localized blood pressure waveforms[38]. The blood pressure waveform can be calculated as

$$p(t)=p_d * e^{\alpha(\frac{A(t)}{A_d}-1)} \quad (1)$$

where pd is the diastolic pressure, which is acquired on the brachial artery using a blood pressure cuff, A_d is the diastolic arterial cross-section, and α is the vessel rigidity coefficient. Assuming that the artery is rotationally symmetrical, A(t) can be calculated as

$$A(t) = \frac{\pi d^2(t)}{4} \quad (2)$$

where d(t) is the diameter waveform of the target artery. When the device is softly laminated on the skin, each transducer can be individually activated and controlled with a power consumption of 23.6 mW. When the ultrasonic wave reaches interfaces, both transmission and reflection occur. The transmission wave with reduced intensity allows penetration into deeper layers of tissues. The reflection wave, which carries critical location information about the interfaces (for example, the anterior and posterior walls), can be sensed by the same transducer[39]. The vessel diameter measurement results were validated by clinical ultrasonography. At a high pulse repetitive frequency (2,000 Hz), time of flight (TOF) signals corresponding to the pulsating anterior and posterior walls can be accurately recorded by an oscilloscope with 2 GHz sampling frequency,

which will appear as separate and shifting peaks in the amplitude mode. The device can capture the pulsating blood vessel diameter dynamically with high spatial (axial resolution of 0.77 μm) and temporal (500 μs) resolution.

The entire device is encapsulated by a silicone elastomer with modulus on par with that of human skin. The elastomer is only 15 μm thick to provide a trade-off between mechanical robustness and sufficient acoustic emission performance. The hydrophobic nature of the silicone elastomer provides a barrier to moisture, which protects the device from possible sweat corrosion. Owing to its soft mechanics, the as-fabricated ultrasound patch allows conformation to both developable and non-developable surfaces. The device is also robust and can endure twisting and stretching, showing its high potential for skin integration applications.

1.5 Design of The Stretchable Ultrasonic Array for Tissue imaging.

Figure 8 shows the schematic working mechanism of a 16 by 16 array. The array is able to conform to the human skin for high-quality imaging. After the array is activated, ultrasound waves are sent into the tissue underneath the device. Scattering sources (e.g., tissue interfaces) can reflect the ultrasound waves, which carry location information of these scattering sources. The reflected waves are then received by the transducer elements in the ultrasonic array as radiofrequency data. The collected radiofrequency data by each element are then enhanced by receive beamforming. After that, 0.5%~1% strain is applied to the tissue by quasi-static uniaxial compression. The low strain ensures that the tissues exhibit linear stress-strain behavior, i.e., their Young's modulus does

not vary with load[40]. After compression, the maximum change in the array's pitch is only 0.02%. Therefore, the associated phase aberration is negligible for both transmit and receive beamforming, especially for deep-tissue inspections. As a result, we can use the same time-delay profile for both post- and pre-compression receive beamforming. A normalized cross-correlation algorithm was used to compare the radiofrequency data before and after compression, and calculate the displacements of the scattering sources with high sonographic sensitivity and accuracy[41,42]. A least-squares strain estimator was used to transform displacements to strain while minimizing possible fluctuations[43]. An inverse elasticity problem was solved to quantify the modulus distribution inside the tissue.

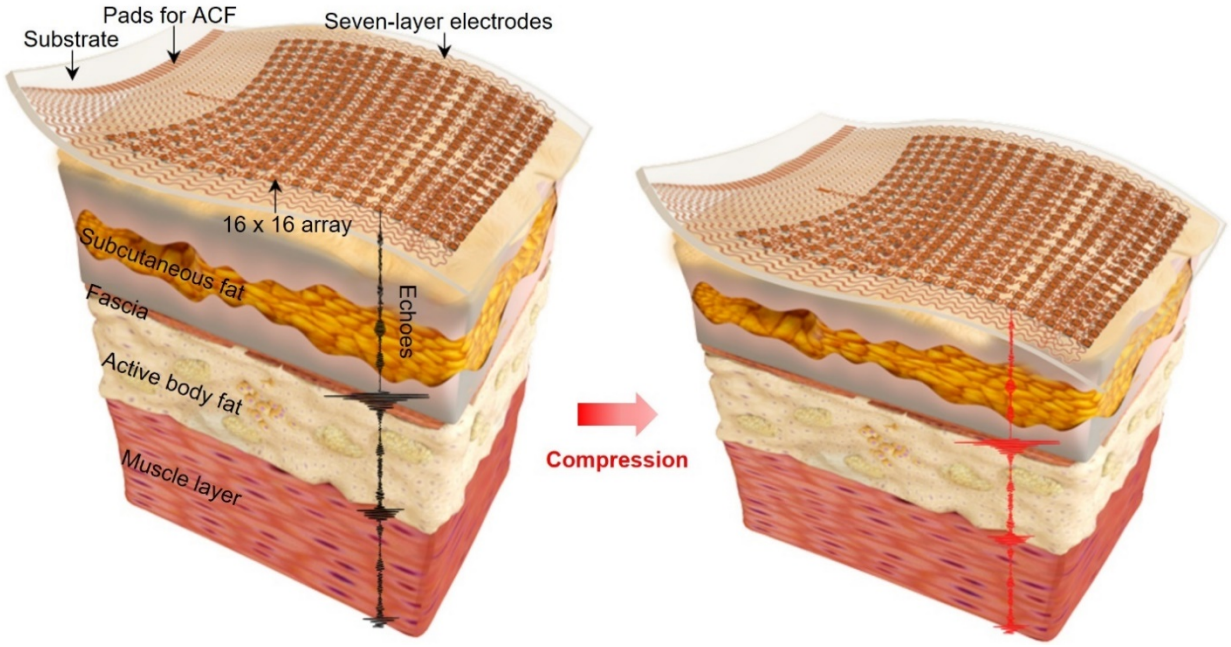

Figure 8. Schematics of the stretchable ultrasonic array laminated on a soft tissue. The device consists of a 16 by 16 array of transducer elements that are connected in-parallel by a seven-layer electrode and encapsulated with water-proof and biocompatible silicone elastomer. This layout allows activating each element individually with a particular time-delay profile and capturing the reflected echoes from scattering sources, (left) pre- and (right) post-compression. The beamformed pre- and post-compression signals are cross-correlated to derive the displacement, strain, and modulus fields. ACF: anisotropic conductive film.

We chose a center frequency of 3 MHz to balance the requirement of high spatial resolution[44] and frequency-dependent linear attenuation of the ultrasound wave in tissues[45]. The characterized mean resonant and anti-resonant frequencies show a small standard deviation, indicating the consistency across the entire array (Fig. 9). Given the corresponding ultrasound wavelength of ~500 μm in soft tissues, we chose a pitch of 800 μm that is suitable for generating wave convergence[46], producing high-quality images, and minimizing crosstalk[28]. A scalable method was used to align the backing material and the transducer elements, which enhanced the fabrication throughput and performance consistency, and avoided potential phase aberrations[27,28]. To individually address the 256 elements, six layers of activation electrodes and one layer of common ground in a serpentine shape were transfer-printed and routed to the same plane by vertical interconnect accesses. A low-temperature bonding technique was used to preserve the high electromechanical coupling coefficient of the 256 elements (average 0.64, Fig. 9 inset), with performance comparable to elements in commercial ultrasound probes (0.58-0.69)[47].

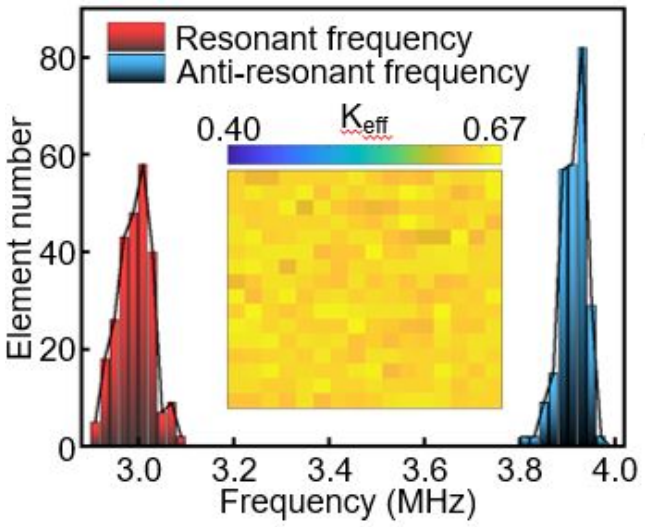

Figure 9. Resonant frequency, anti-resonant frequency, and calculated effective electromechanical coupling coefficient (K_{eff}) distribution of the elements (inset).

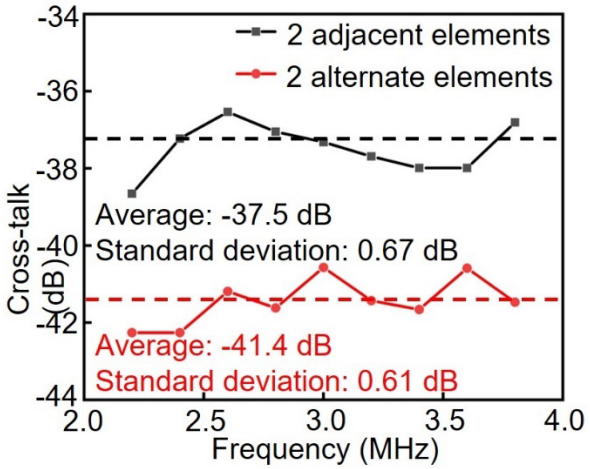

Figure 10. Evaluation of crosstalk between two adjacent elements and two alternate elements.

Because of the well-designed pitch, the suppression of shear vibrations by the 1-3 composite, and the damping effect of silicone elastomer between the elements, crosstalk between the elements is below the standard value of -30 dB (Fig. 10). A matching circuit effectively reduces the insertion loss to 16.98 dB at the resonant frequency, comparable to a commercial probe (17 dB)[48]. The low insertion loss leads to excellent sonographic sensitivity (Fig. 11), which is pivotal for modulus imaging[49]. The high-performance 1-3 composite material used, together with the innovative fabrication protocol and effective matching circuit, results in an average sonographic signal-to-noise ratio of 39 dB, comparable to a commercial probe (41 dB)[49]. The standard deviation of the sonographic signal-to-noise ratio measured underwater for two weeks is small (0.87), because of the excellent water-proof property of the encapsulating silicone elastomer. The device can be reversibly deformed in various modes (Fig. 12). The maximum biaxial stretchability of the

device without affecting its electromechanical properties is ~40%, indicating its reliability for skin integration[50].

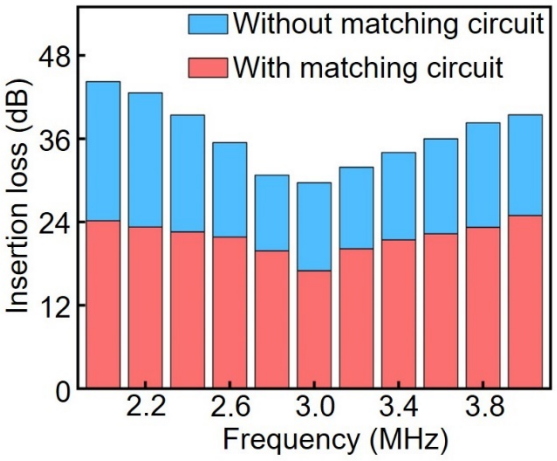

Figure 11. Insertion loss of the transducers with and without the matching circuit. The insertion loss has a minimum value at the resonant frequency because of the maximum electrical power generated by the echoes.

1.6 Conclusion.

In this chapter, we have discussed current research and challenges in the wearable and stretchable ultrasonic field from the material preparation to the device fabrication. Even though promising devices have been fabricated, critical problems such as the intrinsic stability issues in all sorts of properties, including the acoustic and mechanical properties, need to be characterized, which will quantify the performance of the device.

Chapter One, in full, is a partial reprint of the materials: ‘Stretchable ultrasonic transducer arrays for three-dimensional imaging on complex surfaces, Hu, H., Zhu, X., Wang, C., Zhang, L., Li, X., Lee, S., Huang, Z., Chen, R., Chen, Z., Wang, C., Gu, Y., Chen, Y., Lei, Y., Zhang, T.,

Kim, N., Guo, Y., Teng, Y., Zhou, W., Li, Y., Nomoto, A., Sternini, S., Zhou, Q., Pharr, M., Lanza di Scalea, F., Xu, S., Science advances, 4.3 (2018): eaar3979'; 'Monitoring of the central blood pressure waveform via a conformal ultrasonic device, Wang, C., Li, X., Hu, H., Zhang, L., Huang, Z., Lin, M., Zhang, Z., Yin, Z., Huang, B., Gong, H., Bhaskaran, S., Gu, Y., Makihata, M., Guo, Y., Lei, Y., Chen, Y., Wang, C., Li, Y., Zhang, T., Chen, Z., Pisano, A., Zhang, L., Zhou, Q., Xu, S., Nature biomedical engineering 2.9 (2018): 687-695'; 'Three-dimensional mapping of deep tissue modulus by stretchable ultrasonic arrays, Hu, H., Ma, Y., Gao, X., Song, D., Li, M., Huang, H., Qian, X., Shi, K., Ding, H., Lin, M., Chen, X., Zhao, W., Qi, B., Zhou, Sai; Chen, R., Gu, Y., Chen, Y., Lei, Y., Wang, C., Wang, C., Tong, Y., Cui, H., Zhu, Y., Tian, X., Chen, Z., Lu, C., Eghtedari, M., Zhou, Q., Oberai, A., Xu, S., Submitted'; 'Soft wearable devices for deep tissue sensing, Lin, M., Hu, H., Zhou, S., Xu, S., Accepted'. The dissertation author was the first or co-first author of these papers.

Chapter 2. The Characterization of The Stretchable Ultrasonic Array.

2.1 Acoustic Performance Characterization.

Ultrasound emission and sensing rely on the reversible conversion of mechanical and electrical energy. The electromechanical coupling capability is thus a key metric to evaluate the ultrasound transducer performance. As illustrated in Figure. 12, the electrical impedance and phase angle spectra of the 1-3 composite before and after fabrication are measured, from which we can obtain the electromechanical coupling coefficient k (k_t and k_{eff}) and the degree of poling, respectively[51]. The black curves show two sets of well-defined peaks, corresponding to the resonance frequency f_r and the antiresonance frequency f_a. Accordingly, the kt and k_{eff} of the 1-3 composite before and after the fabrication are calculated to be ~0.55 and ~0.60, respectively. The phase angle of the 1-3 composite at the central frequency slightly dropped from ~60° before fabrication to ~50° after fabrication because of the heat-induced slight depolarization of the 1-3 composite. The final phase angle of ~50°, which significantly exceeds many previous reports in flexible or rigid ultrasound probes, due to the intrinsic properties of the 1-3 composite material and optimized fabrication processes[14,52], demonstrates that most of the dipoles in the 1-3 composite align during poling, thereby indicating the outstanding electromechanical coupling properties of our device.

The Krimholtz-Leedom-Matthaei (KLM) model[53] in MATLAB allows for the prediction of the impulse response of the transducer, as a theoretical validation for our device design. The simulated results demonstrate the superb performance of the device in terms of spatial pulse length,

bandwidth, and SNR. Figure 13 shows the experimental results of pulse-echo response and its frequency spectrum. The pulse-echo response, with a narrow spatial pulse length (~1.94 ms), a wide bandwidth (~47.11%), and a high SNR (~20.24 dB), matches well with the simulation result and is on par with that of commercial flexible ultrasonic transducers[54]. The outstanding transducer performance results from (i) the excellent electromechanical coupling of the transducer and (ii) the optimized backing layer that reduces ringing effects.

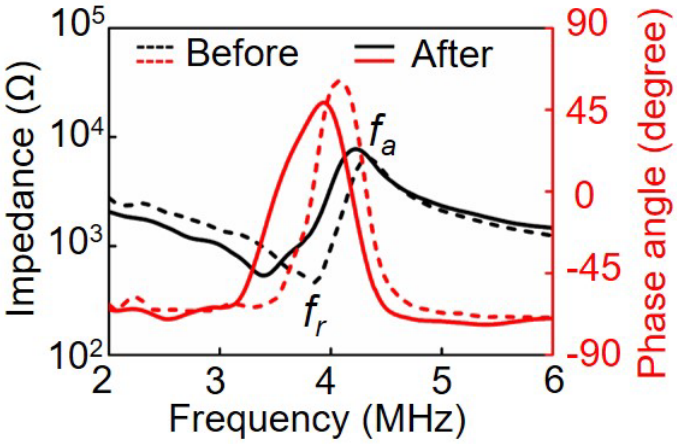

Figure 12. The impedance and phase angle spectra of the 1-3 composite before and after processing, showing good electromechanical coupling of the fabricated transducer (k_{eff}~0.60; θ~50°).

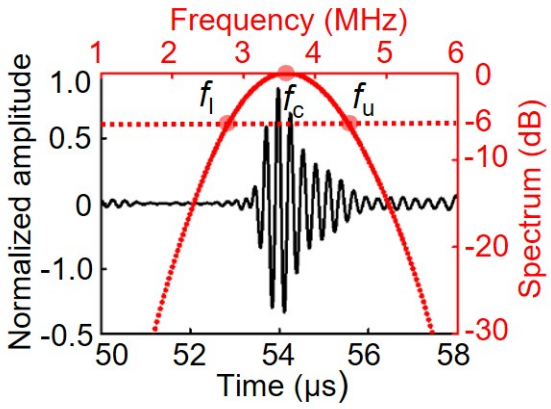

Figure 13. Pulse-echo response and frequency spectra, with a short spatial pulse length (~1.94 ms), a high SNR (~20.24 dB), and a wide bandwidth (~47.11%).

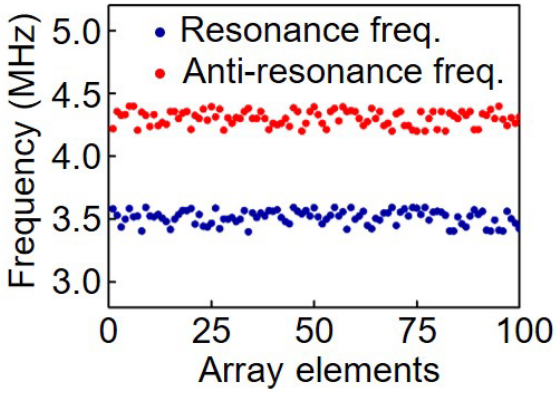

Figure 14. The resonance and antiresonance frequency variations of the 100 transducer elements. The mean values/SDs are 3.51 MHz/56.8 kHz (resonant) and 4.30 MHz/59.1 kHz (anti-resonant), respectively. The 100% yield demonstrates fabrication robustness.

The impedance measurements enable extraction of the resonant and anti-resonant frequencies of each element in the 10 × 10 array (Fig. 14). All 100 elements are functional. The mean values are 3.51 MHz (resonant) and 4.30 MHz (anti-resonant), with SDs of 56.8 and 59.1 kHz, respectively. The stable capacitance (~37.28 pF) and low dielectric loss (tan d < 0.02) of the array further suggest a remarkable uniformity across the array and a reliable fabrication method. Another important metric that assesses the performance of the array is the cross-talk, which

indicates the degree of interference between the elements. Figure 15 shows the cross-talk between elements with different spacings. All cross-talk levels are around -70 dB, with slight fluctuations, which is significantly lower than the standard -30 dB in the field[55]. The outstanding anti-interference properties arise from the 1-3 composites' effective suppression of spurious shear and from the silicone elastomer providing effective isolation among the elements. Overall, this combination of properties ensures low levels of noise in the ultrasonic imaging system[31].

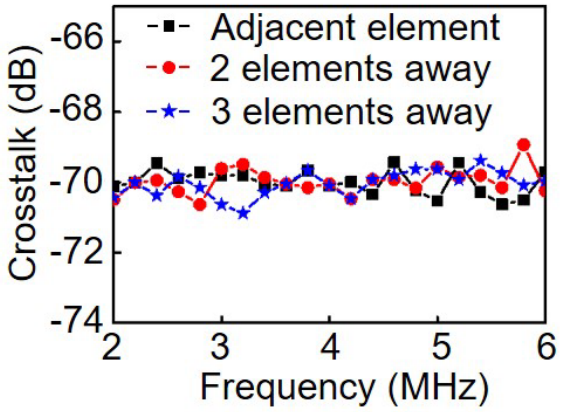

Figure 15. Average cross-talk levels between elements that are adjacent, two elements away, and three elements away, showing the outstanding anti-interference capacity of the device.

One of the important performance metrics of ultrasound imaging systems is the spatial resolution, in both axial and lateral directions. For the stretchable ultrasound probe, the axial resolution remains constant under different bending curvatures at a defined resonant frequency and bandwidth of the transducer. The lateral resolution is mainly dependent on device geometry, which affects the focal length and aperture size. The *f* number is used to define the ratio between the focal length and the aperture size[56]. To comprehensively explore the lateral resolution of the probe with

various f numbers, we performed a series of imaging experiments in which the ultrasonic probe is bent to different curvatures. As shown in Figure. 16, the spatial resolution was evaluated by focusing the array at focal lengths of 20, 32, 37, and 52 mm, respectively, to image a Cu wire (300 mm in diameter) located at a particular focal point in a phantom sample. The image was reconstructed using the DMAS (delay multiply and sum) algorithm[57], which more effectively suppressed the level of noise floor (~-40 dB, causing the energy ratio of noise to reflector to be only 0.01%) compared with a conventional algorithm such as DAS (delay and sum; Fig. 17)[58]. In light of this metric, the side lobes and grating lobes in images can be greatly reduced by using the DMAS, and the results from these four tests are combined in Figure 18. A configuration of -10 dB dynamic range in combination with an image resolution of 20 pixels/mm is applied to highlight the imaging capabilities.

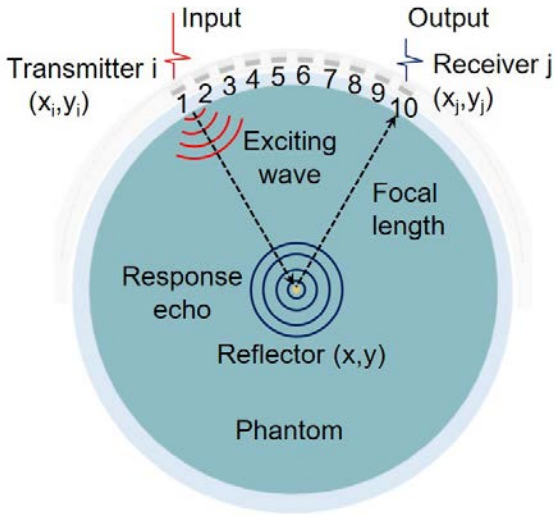

Figure 16. Schematics of spatial resolution measurement setup, with focal lengths of 20, 32, 37, and 52 mm, respectively.

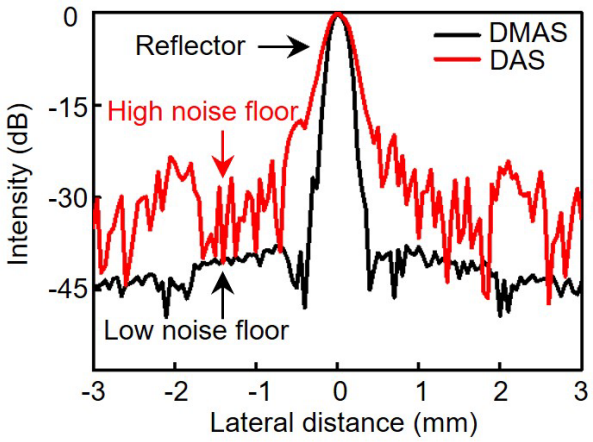

Figure 17. Comparison of noise floors reconstructed by DMAS and DAS algorithms, revealing the benefits of the DMAS algorithm with only 0.01% energy ratio of noise to the reflector.

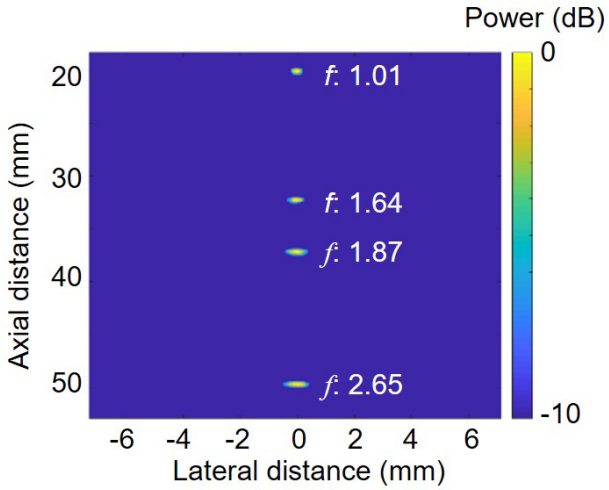

Figure 18. Images of wire phantom combining the four tests with different *f* numbers, showing the capability of focusing at different depths and obtaining high resolution images.

Plots of the axial and lateral line spread functions of the obtained images (Fig. 17) are shown in Figures 19 and 20. The measured FWHM (full width at half maximum) resolutions (-6 dB)[56,59] were calculated for the axial and lateral directions, as indicated by the dashed lines. As the f number decreases, the axial resolution remains relatively constant at around 610 mm, and the

lateral resolution improves approximately linearly from 789 to 344 mm. These results are in line with the theoretical results (an axial resolution of around 601 mm; lateral resolutions ranging from 787 to 284 mm) from the MATLAB k-Wave toolbox simulations (Fig. 21). The fine spatial resolution at the focal point, which is comparable to the 3.5 Hz commercial ultrasound probe resolution of 610 mm[60], is due to the combined effects of the high performance transducers, a strategic device structural design, and an advanced imaging algorithm.

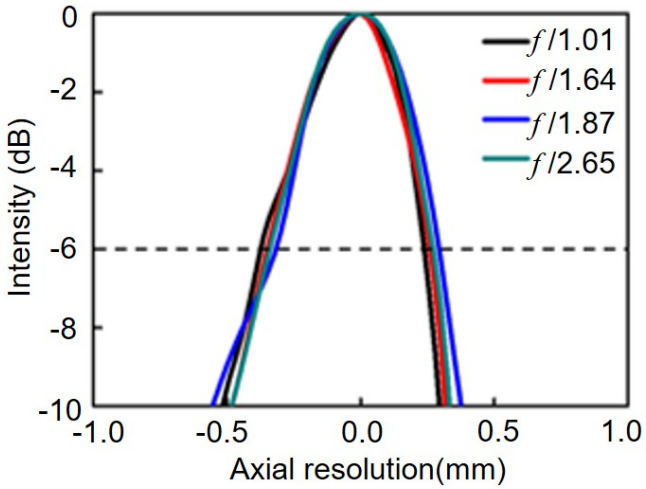

Figure 19. Axial line spread functions for the center wire at different focal lengths. Resolution is defined as the line spread function width at an intensity of -6 dB.

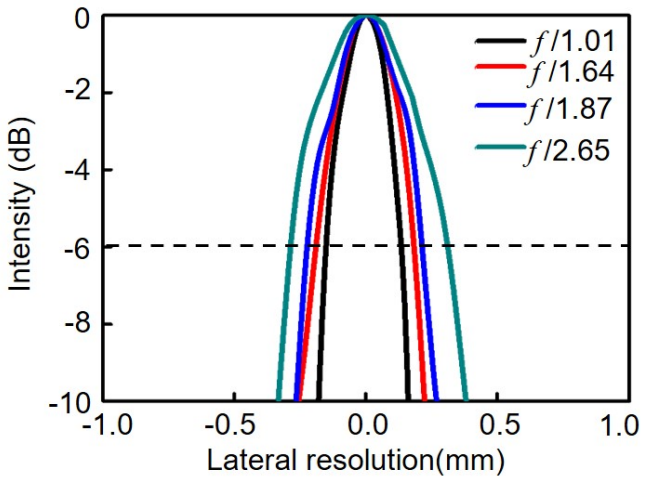

Figure 20. Lateral line spread functions for the center wire at different focal lengths.

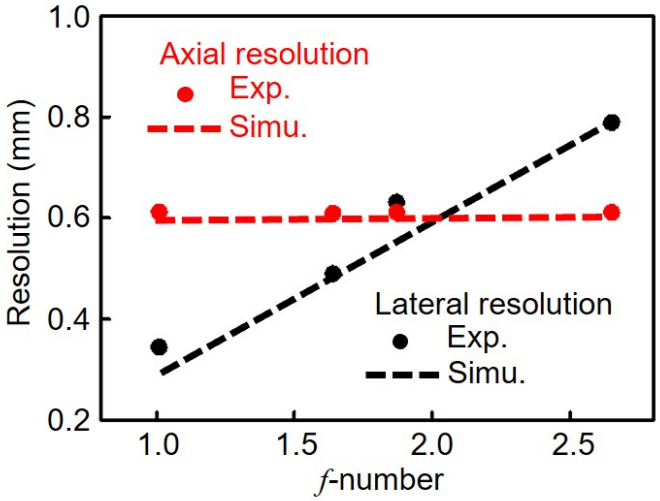

Figure 21. Experimental (Exp.) and simulation (Simu.) results of lateral and axial resolutions.

2.2 Mechanical Performance Characterization.

Mechanical properties of conductive interconnects are critical for flexible and stretchable devices[61-63]. Experimental results from biaxial stretching of the layered structures of serpentines between 0 and 50% and corresponding 3D finite element analysis (FEA) are shown in Figure 22

and Figure 23. A 2 × 2 array of elements is selected for visualization of the key mechanics involved. Under tensile loading, the horseshoe serpentines undergo an in-plane unraveling process and out-of-plane rotation and twisting, both of which mitigate the level of strain in the islands themselves[64,65]. Specifically, in these ultrasound arrays, 50% biaxial stretching produces a maximum of only ~1.2% tensile strain in the Cu interconnects, as shown in the FEA image of Figure 22. After the serpentines have fully unraveled (that is, finished rotating in-plane), the tensile strain in the Cu interconnects increases rapidly, thus defining the stretching limit of the serpentines[64,66], which is between ~50 and 60% in this case. Going beyond this limit will lead to fracture of the serpentines. In addition, for the reliability of these devices, they must be capable of sustaining mechanical integrity upon repetitive loading. In metals such as Cu, cycling into the plastic regime will cause permanent deformation of the interconnects, which may affect device performance or may eventually produce fatigue cracks[67]. According to both the simulations and the experiments, ~30 to 40% biaxial stretching produces irreversible deformation in the serpentines upon releasing (Fig. 24) and partial delamination between the serpentines and the silicone elastomer, as highlighted in Figure 23. However, below 30 to 40% biaxial stretching, mechanical integrity is maintained. Moreover, mechanical deformations have minimal influence on device performance, which is reflected by the stable impedances of each element (Figs. 25 and 26) and the resistance of the serpentines (Fig. 27) at various levels of tensile strains and bending curvatures. As for the device for the tissue imaging, the device can be reversibly deformed in various modes

(Fig. 28). The maximum biaxial stretchability of the device without affecting its electromechanical properties is ~40%, indicating its reliability for skin integration[50].

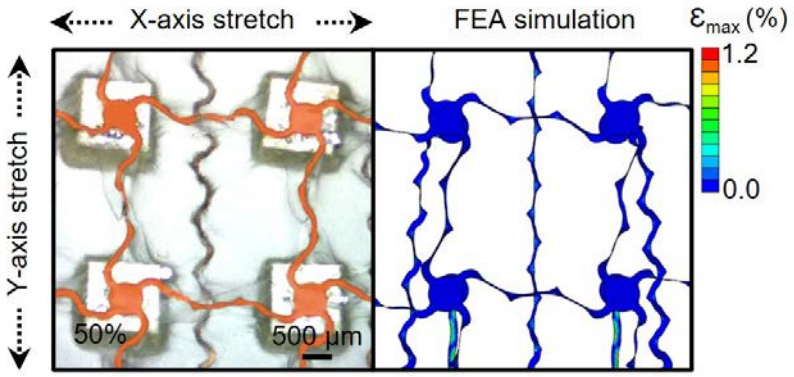

Figure 22. The optical image (left) and corresponding finite element analysis (FEA) simulation (right) of a 2 × 2 array under 50% biaxial tensile strain, showing its excellent stretchability. The local strain level (maximum principal strain) in the interconnects is indicated by the color scale.

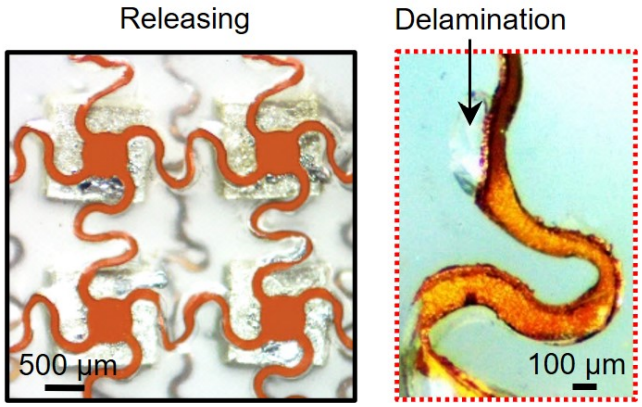

Figure 23. The optical image after releasing the biaxial strain of 50%. The zoomed-in image highlights plastic deformation and local delamination of the interconnects upon loading/unloading.

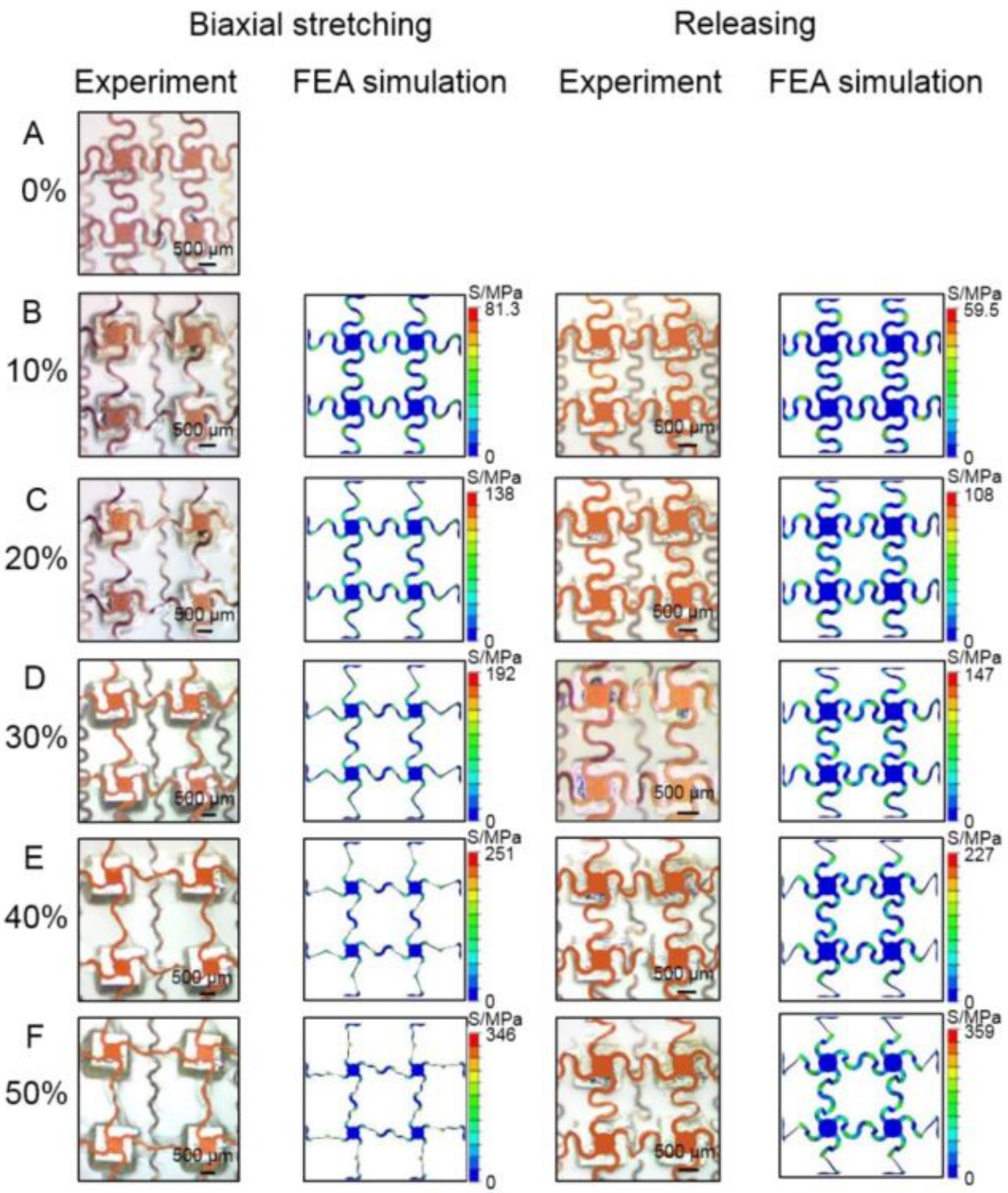

Figure 24. Experimental and simulation results of a small array under biaxial tensile strain.

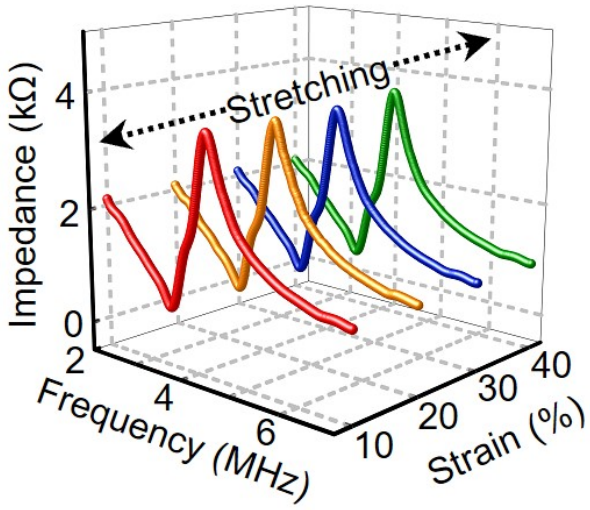

Figure 25. Electrical impedances of the transducer under different strain levels, showing the mechanical stability of the device.

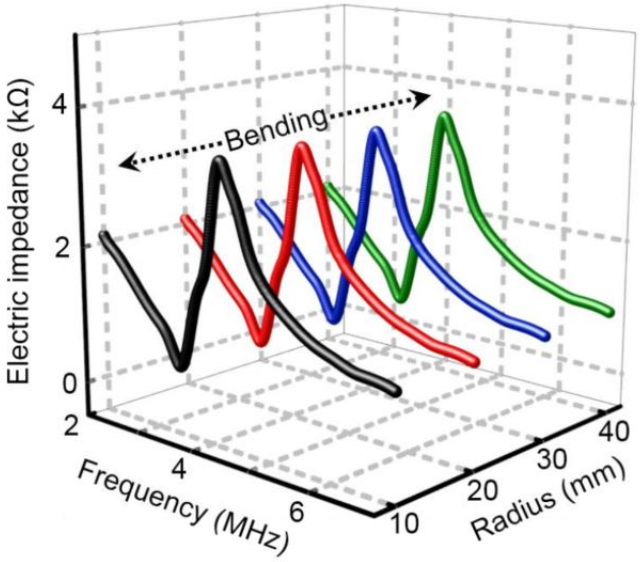

Figure 26. Electrical impedances under different bending curvatures.

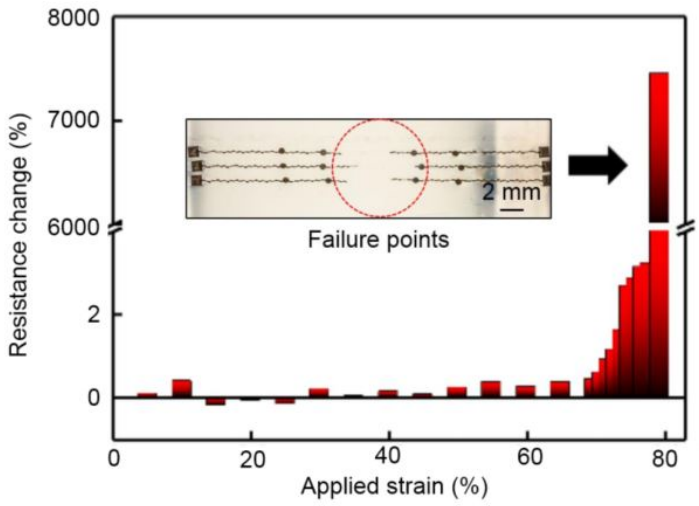

Figure 27. Relative resistance changes of Cu serpentine under stretching.

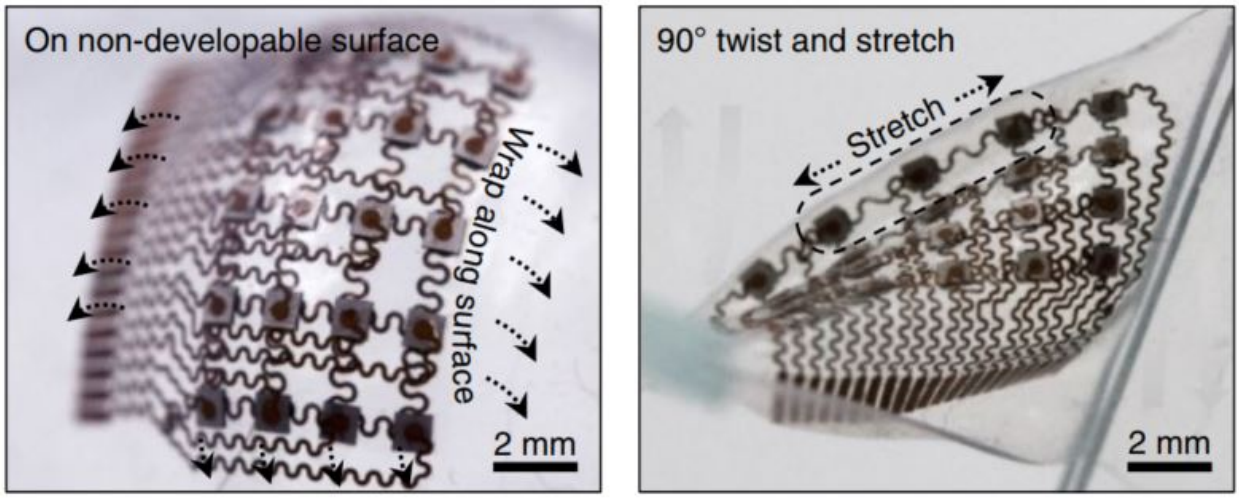

Figure 28. The device conforming to non-developable surfaces and under mixed modes of stretching and twisting.

2.3 Characterization of Elastography.

To determine the transmission mode for elastography, we simulated 2D strain distributions in a bilayer phantom under three different transmission modes: single plane wave, mono-focus, and coherent plane-wave compounding (Fig. 29)[68], and then analyzed the SNR_e and CNR_e, the two

most critical metrics for modulus mapping[69]. Among the three modes, the single plane wave mode produces the lowest SNR_e and CNR_e, because of the low transmission energy from non-focal scanning (Fig. 30). The mono-focal mode provides better SNR_e and CNR_e, but only in regions near the focal depth. The coherent plane-wave compounding mode consists of a series of single plane waves at different transmission angles, and these steered frames are coherently integrated to reconstruct a multi-angle compounding image, with multiplex signal intensities across the entire region. The resulting SNR_e and CNR_e levels are significantly enhanced in all regions[68]. The performance of the compounding strategy highly depends on the step size and the number of the steering angles used. In this work, we use 19 steering angles and a step size of 1°, which were found in experiments to give the best elastographic image quality (Figs. 31 to 34).

A high SNR_e is critical for high-quality elastographic imaging. The SNR_e is influenced by the magnitude of applied strain and the normalized cross-correlation coefficient, which reflects the similarity of the radiofrequency signals before and after compression. The smallest detectable strain with SNR_e of 6 dB is 0.0125%, which indicates the high elastographic sensitivity of the stretchable array (Fig. 35). At low strain levels, the displacement signals are small, so the relatively large intrinsic electrical noise in the radiofrequency signals leads to large deviations in the elastographic images and thus a low SNR_e. As the applied strain increases, the displacement signals increase proportionally, while the intrinsic electrical noise remains relatively constant, leading to an increase in the SNR_e. The SNR_e becomes the highest at ~1% strain. Beyond 1% strain, the radiofrequency signals distort in shape and amplitude[70], resulting in a sharp fall in the

normalized cross-correlation coefficient and therefore SNR_e (Fig. 35). The dynamic range (i.e., the strain range with high SNR_e) was determined by a -3 dB cutoff from the maximum SNR_e, which is 0.36%~2.34% in this work, corresponding to a normalized cross-correlation coefficient >0.8.

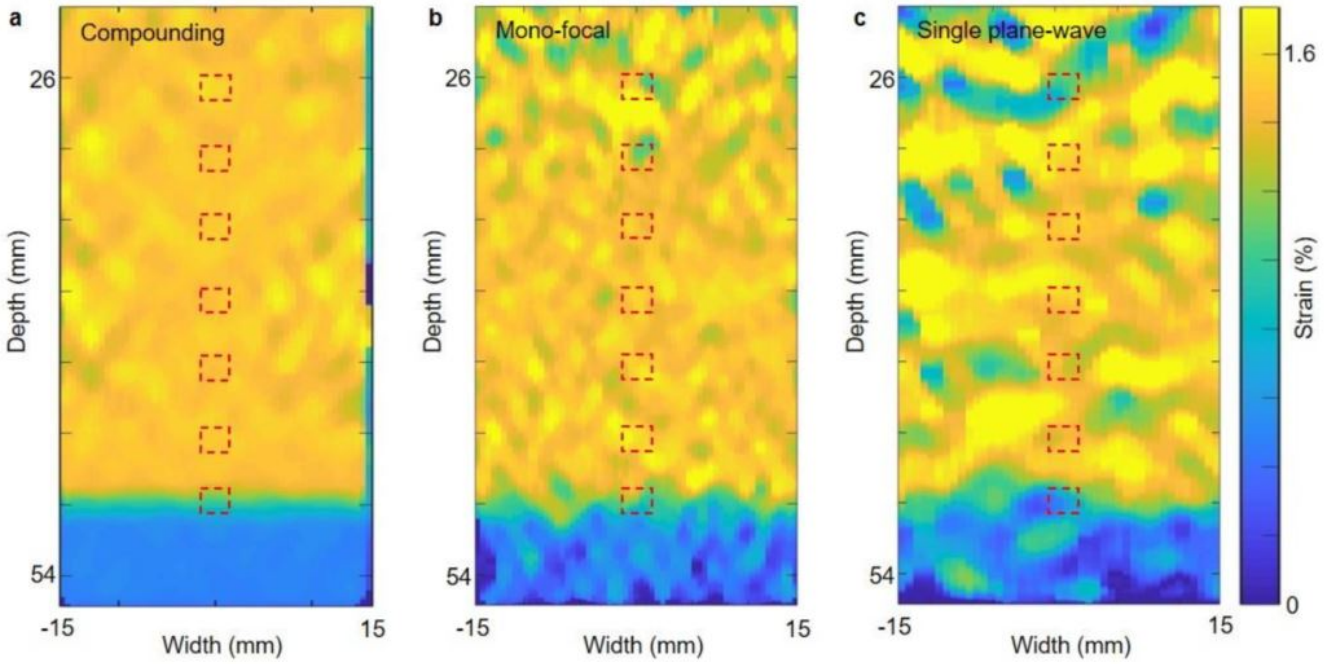

Figure 29. Comparison of three different transmission modes. Strain distribution simulations using (a) coherent plane wave compounding, (b) mono-focus, (c) single plane-wave transmission modes. Red dashed boxes are the locations of choice for comparison. The single plane wave mode has a high frame rate and a short image reconstruction time since it does not need to steer multiple angles. The mono-focal mode can achieve a high image quality at the focal depth. The coherent plane-wave compounding mode provides images with the best SNRe and CNRe than the other two modes so it is used as the transmission mode for elastography imaging in this work.

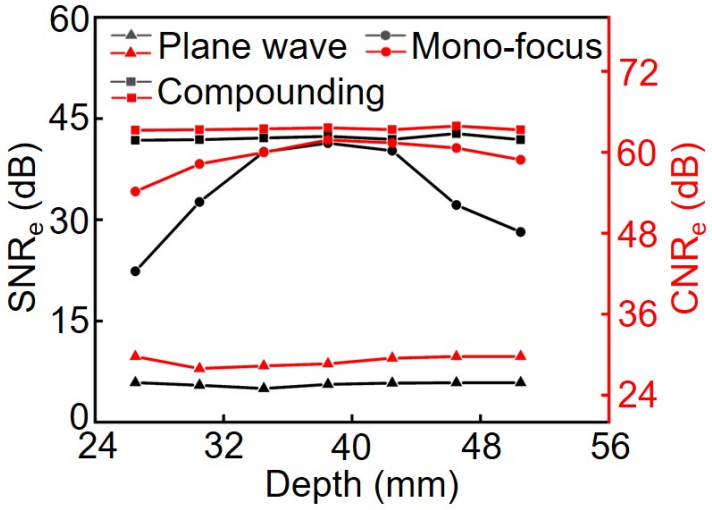

Figure 30. Simulations showing the SNR_e and CNR_e of the coherent plane wave compounding, mono-focus, and single plane wave transmission modes in a bilayer phantom.

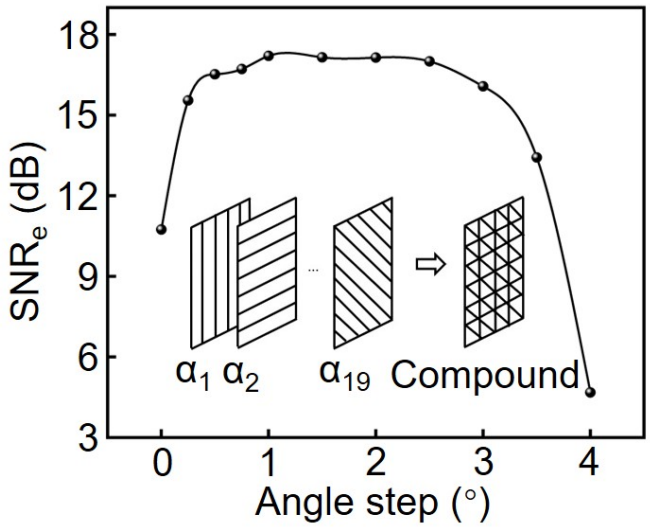

Figure 31. The SNRe as a function of the step size of the steering angle. Inset is a schematic diagram showing the process of compounding: a set of plane waves are transmitted with different steering angles and a final compounded image is built by coherently adding all beamformed images.

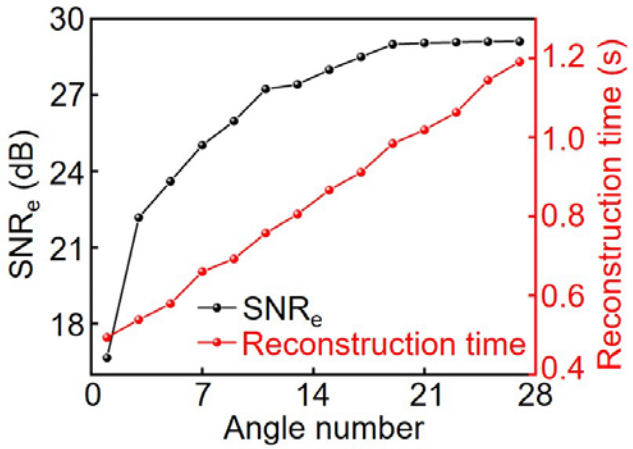

Figure 32. The SNR_e and reconstruction time with different numbers of steering angles.

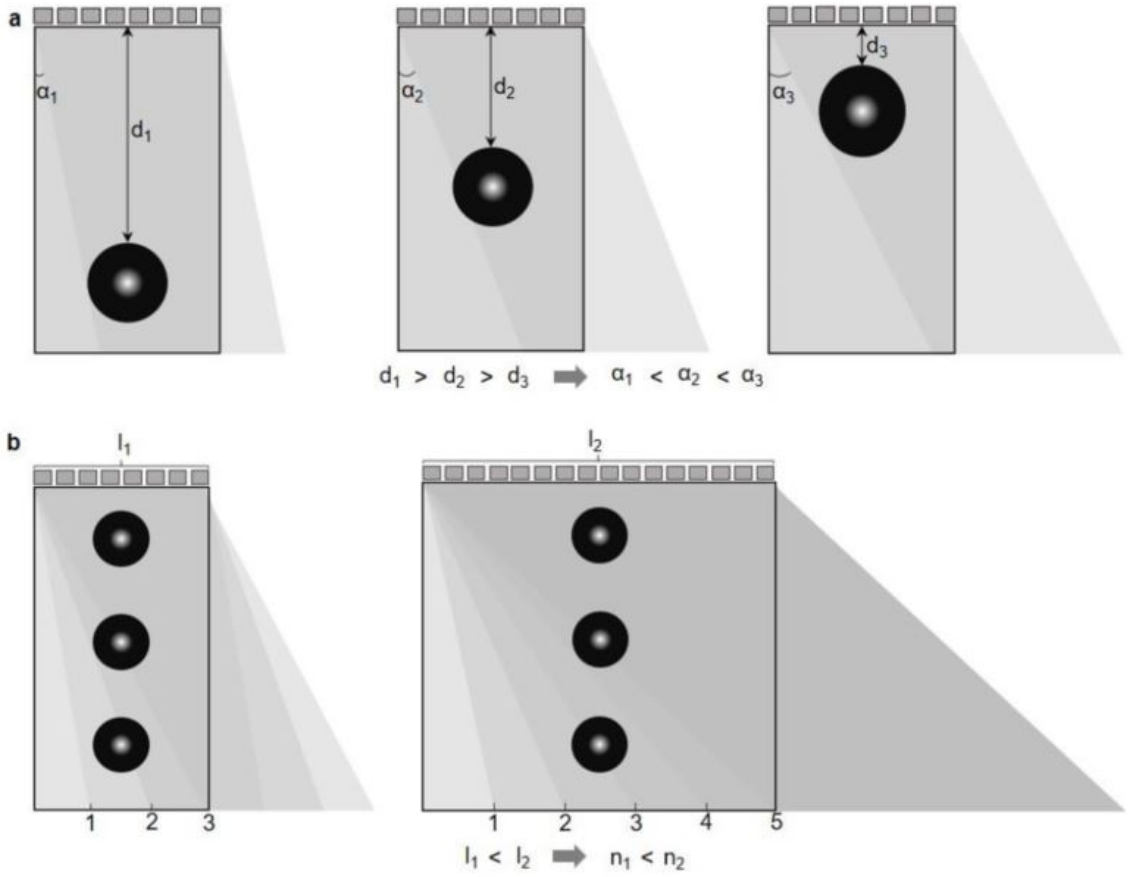

Figure 33. Factors affecting the step size and number of the compounding angle. (A) The step size mainly relies on the position of the target region. The deeper region needs a smaller step size, so the majority of scanned frames coherently overlap in this region. d: depth, α: step size. (B) The number of angles mainly relies on the aperture size of the transducer array.

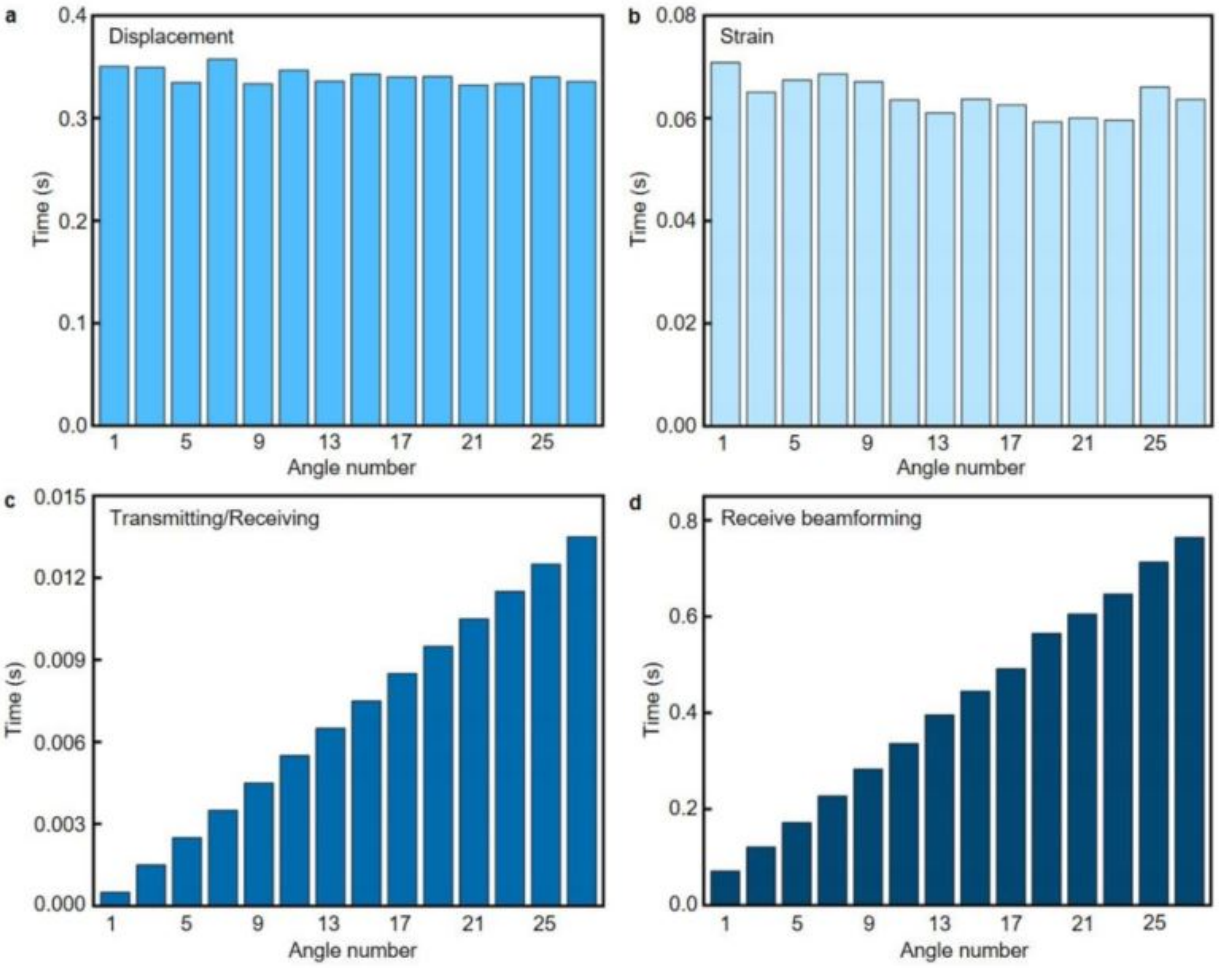

Figure 34. Processing time for reconstructing images at different angle numbers. Time for (A) displacement calculation, (B) strain calculation, (C) transmitting/receiving, and (D) receive beamforming with different angle numbers. Time for calculating the displacement and strain keeps constant at different angle numbers but for the transmitting/receiving processes and receive beamforming is increasing linearly with the angle number. Specifically, time for receive beamforming dominates. Balancing the overall time budget and the gain in SNR_e at different numbers of steering angles, we use 19 angles for the compounding imaging in this work.

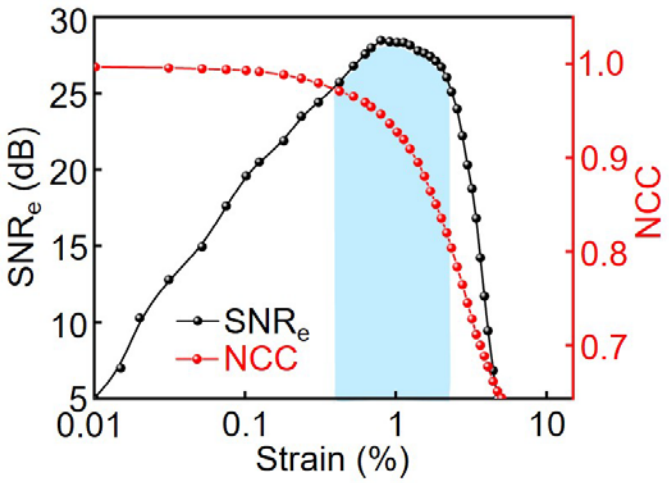

Figure 35. The SNR_e and normalized correlation coefficient (NCC) as 158 a function of applied strain. The shaded area with >0.8 NCC by a -3 dB strain filter shows the dynamic range.

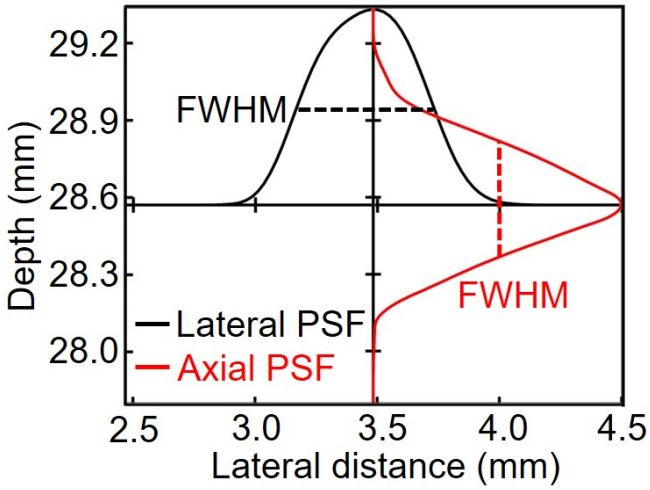

Figure 36. Lateral and axial resolutions of the stretchable ultrasonic array based on the full width at half maximum (FWHM) of point spread functions (PSF).

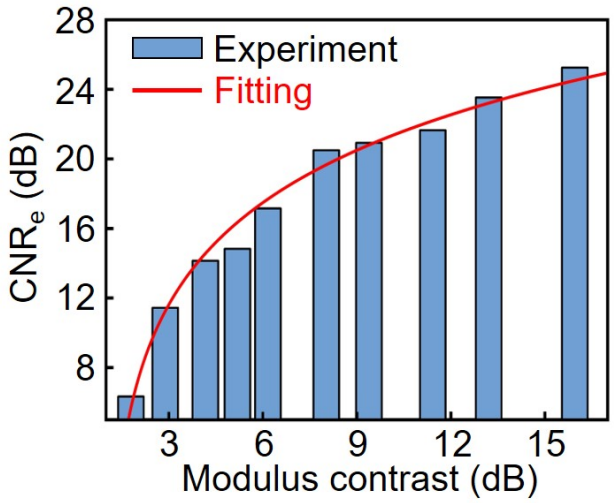

Figure 37. Quantification of the contrast resolution based on the relationship between the CNR_e and modulus contrast of phantoms.

Both spatial resolution and contrast resolution are critical for elastographic imaging[71]. To characterize the spatial resolution, we imaged and extracted the modulus distribution of the lateral and axial transition edges in an inclusion phantom. The first derivatives of the modulus distribution yield the point spread functions, whose full widths at half maximum are used to estimate the elastographic spatial resolutions[72]. The spatial resolutions are then determined to be 0.56 mm in the lateral and 0.50 mm in the axial directions (Fig. 36). Because of the synthetic focusing effect of the coherent plane-wave compounding mode, the spatial resolution remains high and consistent at different locations across the entire imaged region[68].

Similar to the spatial resolution, the contrast resolution is defined as the modulus contrast with a corresponding CNR_e of 6 dB. To quantify the contrast resolution, we performed tests on bilayer phantoms, each composed of two homogenous gelatin phantoms with different elastic moduli. The modulus of each layer is within 10~100 kPa, covering the modulus range of all typical

healthy and diseased tissues[73], which creates an interfacial modulus contrast ranging from 1.79 dB to 15.94 dB. The CNR_e, determined by the ratio of the strain contrast to the standard deviation of strain distribution, decreases as the modulus contrast becomes lower (Fig. 37). Logarithmic curve-fitting, with a coefficient of determination >0.98, demonstrates the reliability of the experimental results[71]. The contrast resolution of the device is determined to be ~1.79 dB (i.e., a modulus ratio of 1.22).

2.4 Conclusion.

In this chapter, we demonstrate all kinds of characterizations, including the acsoutic performance, mechanical performance, elastographic performance, and B-mode imaging performance. Those characterizations quantify the properties of stretchable and wearable devices that are applied to different applications, which lays the foundation for the application of stretchable and wearable ultrasonic probes in various scenarios.

Chapter Two, in full, is a partial reprint of the materials: ‘Stretchable ultrasonic transducer arrays for three-dimensional imaging on complex surfaces, Hu, H., Zhu, X., Wang, C., Zhang, L., Li, X., Lee, S., Huang, Z., Chen, R., Chen, Z., Wang, C., Gu, Y., Chen, Y., Lei, Y., Zhang, T., Kim, N., Guo, Y., Teng, Y., Zhou, W., Li, Y., Nomoto, A., Sternini, S., Zhou, Q., Pharr, M., Lanza di Scalea, F., Xu, S., Science advances, 4.3 (2018): eaar3979’; ‘Monitoring of the central blood pressure waveform via a conformal ultrasonic device, Wang, C., Li, X., Hu, H., Zhang, L., Huang, Z., Lin, M., Zhang, Z., Yin, Z., Huang, B., Gong, H., Bhaskaran, S., Gu, Y., Makihata, M., Guo,

Y., Lei, Y., Chen, Y., Wang, C., Li, Y., Zhang, T., Chen, Z., Pisano, A., Zhang, L., Zhou, Q., Xu, S., Nature biomedical engineering 2.9 (2018): 687-695'; 'Three-dimensional mapping of deep tissue modulus by stretchable ultrasonic arrays, Hu, H., Ma, Y., Gao, X., Song, D., Li, M., Huang, H., Qian, X., Shi, K., Ding, H., Lin, M., Chen, X., Zhao, W., Qi, B., Zhou, Sai; Chen, R., Gu, Y., Chen, Y., Lei, Y., Wang, C., Wang, C., Tong, Y., Cui, H., Zhu, Y., Tian, X., Chen, Z., Lu, C., Eghtedari, M., Zhou, Q., Oberai, A., Xu, S., Submitted'. The dissertation author was the first or co-first author of these papers.

Chapter 3. Applications in Non Destructive Evaluation.

3.1 Two-Dimensional Imaging on Complex Surfaces.

We used the stretchable ultrasonic device to image customized Al work pieces with embedded defects under planar, concave, and convex surfaces. In all cases, a straight defect (2 mm in diameter, orthogonal to the side surface) was created with different distances from the top surface (Fig. 38, A to C, first column). The device was laminated seamlessly on the test surfaces. The synthetic aperture focus (SAF) method was applied to reconstruct the corresponding images[59]. This method allows a sparse transmitter-receiver scheme that bypasses the need for simultaneous excitations, minimizing the number of simultaneously active elements while preserving the image quality. As indicated by the wave field simulation results, the main lobes of the transducer are parallel, divergent, and focused for the planar, concave, and convex surfaces, respectively (Fig. 38, A to C, second column). Considering that the central defect acts as a secondary wave source and the transducer is primarily sensitive to out-of-plane motion (direction normal to transducer's sensing surface), the target surface curvature can greatly influence the captured signal strength. Specifically, for the convex surface, most of the reflected longitudinal wave motion from the defect aligns with the direction perpendicular to the sensing surface; for the concave surface, the reflected wave motion aligns with the in-plane motion (direction parallel to the sensing surface); for the planar surface, which is an intermediate case, the sensitivity of the transducer mainly depends on the component of the reflected wave vector normal to the sensing surface. To acquire the defect

signals, for each case, we obtained 90 sets of data. Longitudinal wave reflection signals from the defects and the bottom boundaries, with more than 18 dB SNR, can be collected with predicted times of arrival (Fig. 38, A to C, third column). The obtained full-field images of the defects are shown in the fourth column of Fig. 38 (A to C), which have no artifacts and match the simulation results extremely well (Fig. 39). These results suggest that the stretchable ultrasound probe is capable of accurately imaging defects in media of complex surface geometries.

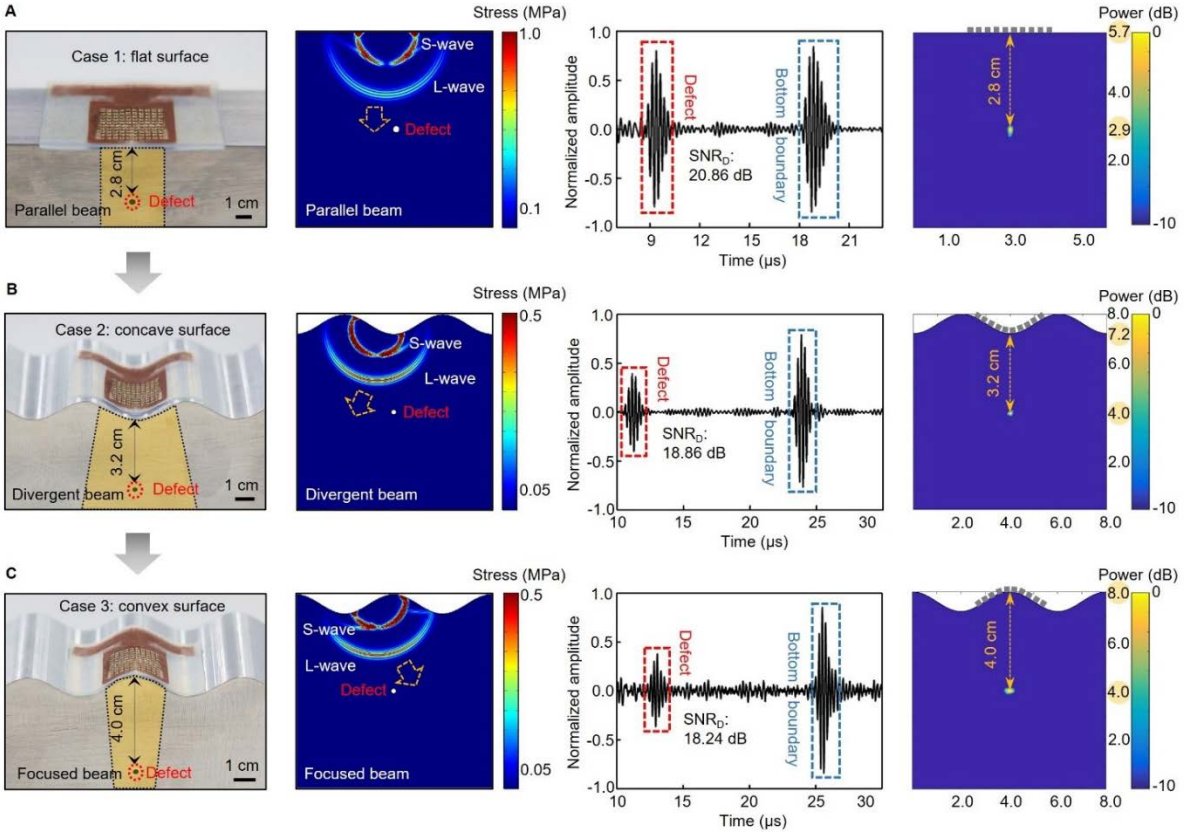

Figure 38. Two-dimensional images of a linear defect under complex surfaces. Optical images of experimental setups with the stretchable ultrasonic device tested on (A) planar, (B) concave, and (C) convex surfaces showing the good conformability of the device on these surfaces (first column); simulation results showing the different wave fields and sensing modes (second column); pulse-echo signals from the defects and boundaries with high SNR (third column); and acquired 2D images using DMAS algorithms with accurate and artifact-free positions (fourth column). S wave, shear wave; L wave, longitudinal wave; SNRD, SNR of pulse-echo response from the defect.

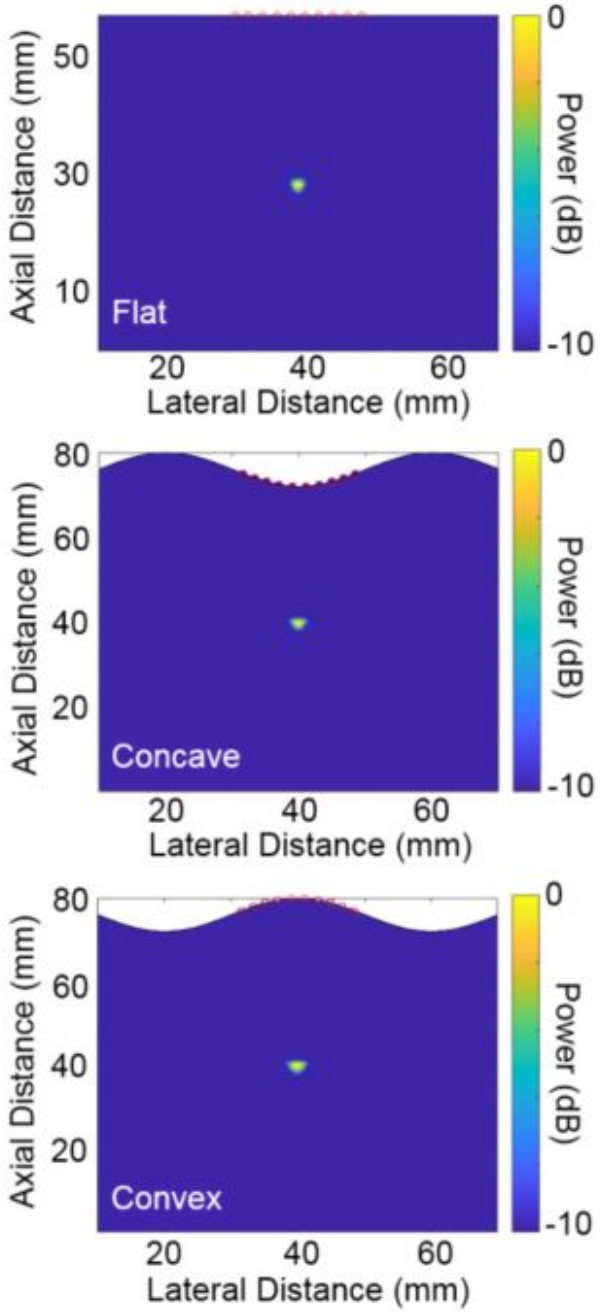

Figure 39. Reconstructed images based on simulation under flat, concave, and convex surfaces.

3.2 Three-Dimensional Imaging on Complex Surfaces.

For practical engineering inspections, detection of multiple defects is of particular interest, for example, welding inspection of a pipeline[74] and rail track detection under shelling[75]. The stretchable ultrasonic device was used for 3D internal structure visualization by imaging two defects with different depths and orientations under a sinusoidal curved surface. A schematic of the experimental setup is shown in Fig. 40, with one defect orthogonal to the x-z plane at a depth of 4.0 cm below the top surface, and the other defect 18° tilted away from the y axis at a depth of 6.0 cm below the top surface. Each 1 × 10 linear array in the x-z plane generates a 2D cross-sectional image of the two defects using the DMAS algorithm (Fig. 41), similar to Fig. 38. The upper defect reflects part of the wave and reduces the wave energy reaching the lower defect. Thus, it produces a shadowing effect[76], which is exacerbated by the tilted configuration of the lower defect as the array scans from the y = 0 to the y = 1.8 plane. The 3D image can be reconstructed by integrating the 10 slices with a 2-mm pitch along the y axis, as shown in Fig. 42. The shadowing effect is removed by normalizing against the peak intensity of each defect. The corresponding front, top, and side views are shown in Fig. 43, which accurately match the design in Fig. 40, thereby demonstrating the capability of volumetric imaging using the stretchable ultrasonic probe. Similar protocols of testing and imaging reconstruction can be applied to general and more sophisticated surfaces.

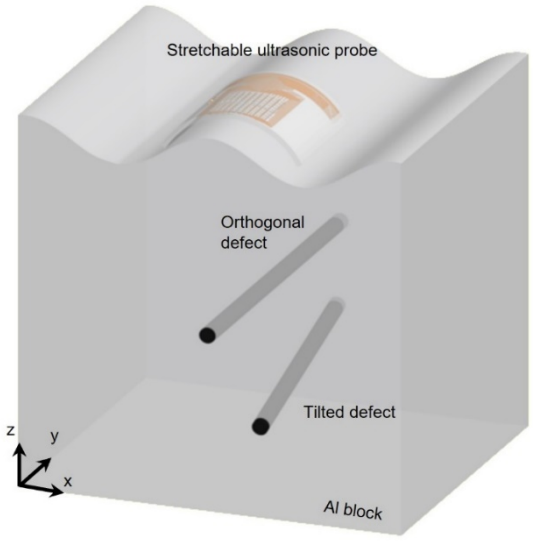

Figure 40. Schematics of the experimental setup, illustrating the spatial location and relative orientation of the two defects in the test subject.

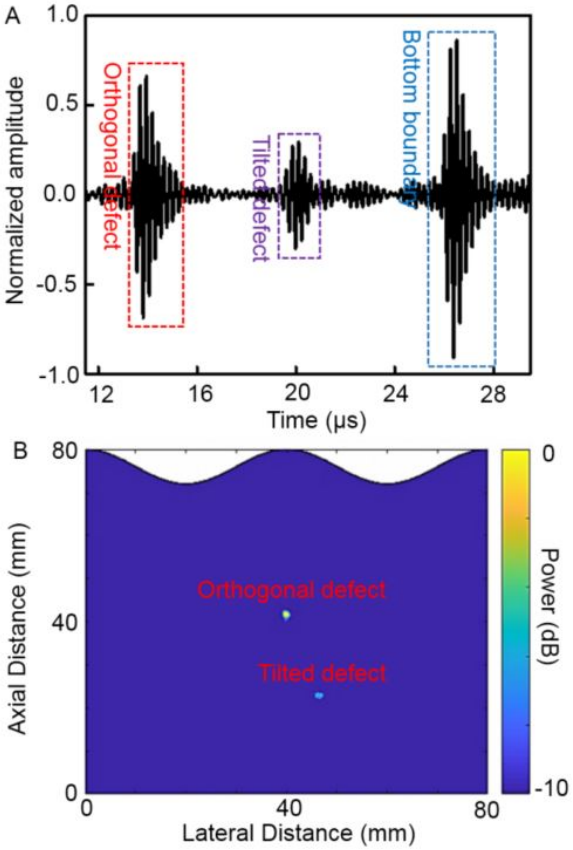

Figure 41. The pulse-echo signal and 2D image of the two defects. (A) The clear pulse-echo signals of the two defects and the bottom boundary acquired by a linear array. (B) The reconstructed 2D image of the two defects.

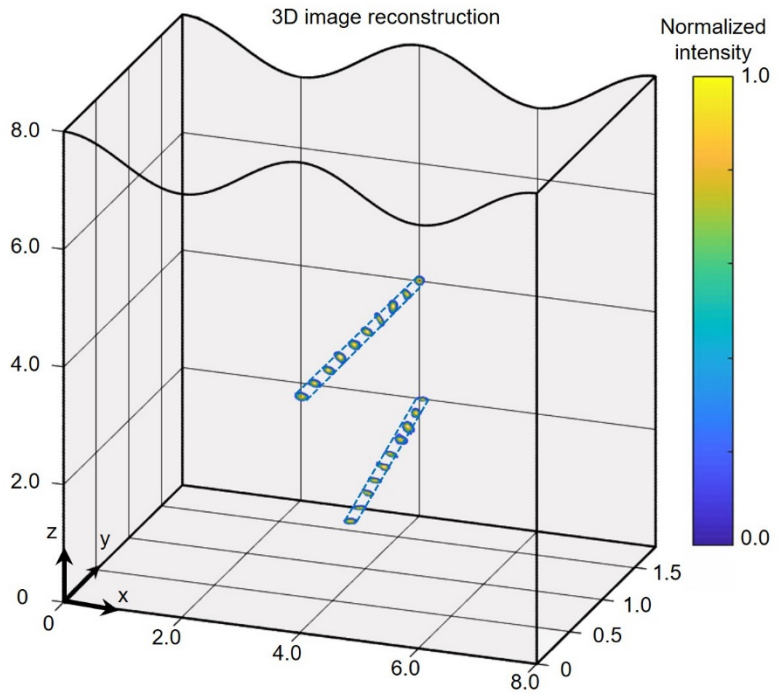

Figure 42. The reconstructed 3D image, showing complete geometries of the two defects.

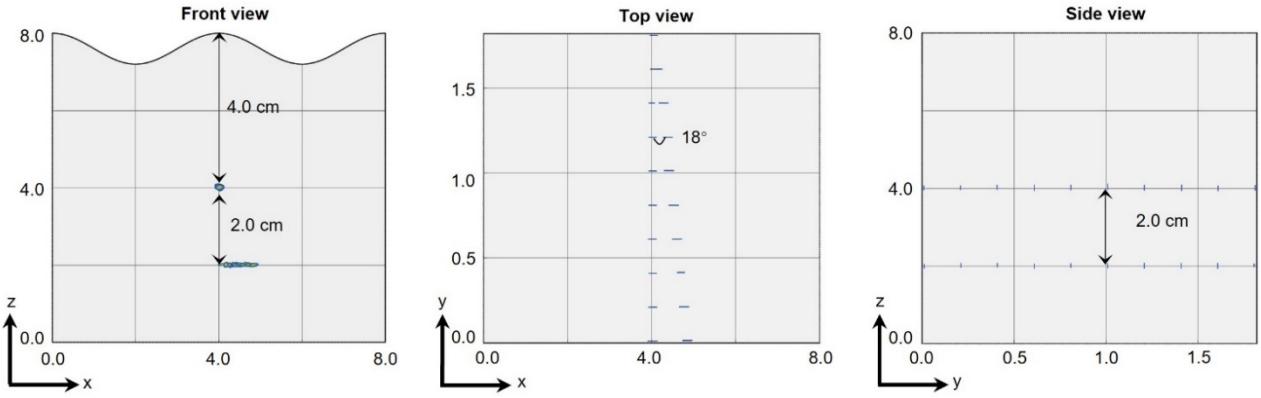

Figure 43. The 3D image from different view angles, showing the relative positions and orientations of the two defects to the top surface, which match the design well.

3.3 Conclusion.

In this chapter, we have introduced the application of the stretchable ultrasonic transducer array on the industrial components. The hybridized material integration, electrode design strategies,

and imaging algorithm development introduced here provide a foundational basis for stretchable ultrasound imaging arrays that allow nondestructive 3D volumetric inspections under general complex surfaces. The high-performance anisotropic 1-3 piezoelectric composites suppress shear vibrations, reduce cross-talk among the transducer, enhance longitudinal vibrations, and thus improve the overall sensitivity and SNR. Five-layered serpentine electrodes enable a high level of integration and large stretchability of more than 50%. The stretchable ultrasound probe, consisting of a 10 × 10 array of individually addressable transducer elements, can focus at different depths, with comparable spatial resolutions with existing rigid probes. The unique device design, combined with the advanced DMAS imaging algorithms, enables accurate, artifact-free, full field, and nondestructive examinations underneath general complex surfaces. Future studies will focus on improving the device performance by reducing the pitch between elements and exploring the integration of more active elements, incorporating matching layers, automated sensor positioning systems, and wireless signal actuation and transmission chips, for distributed, mobile, and real-time subsurface health monitoring of infrastructures and the human body.

Chapter Three, in full, is a partial reprint of the materials: ‘Stretchable ultrasonic transducer arrays for three-dimensional imaging on complex surfaces, Hu, H., Zhu, X., Wang, C., Zhang, L., Li, X., Lee, S., Huang, Z., Chen, R., Chen, Z., Wang, C., Gu, Y., Chen, Y., Lei, Y., Zhang, T., Kim, N., Guo, Y., Teng, Y., Zhou, W., Li, Y., Nomoto, A., Sternini, S., Zhou, Q., Pharr, M., Lanza di Scalea, F., Xu, S., Science advances, 4.3 (2018): eaar3979’. The dissertation author was the first author of this paper.

Chapter 4. Applications on Monitoring of Human Vital Signs.

4.1 Motivation of The Central Blood Pressure Waveform.

Owing to the amplification effect-namely progressive vascular resistance, stiffness and impedance mismatch between central and peripheral vessels—the arterial pressure waveform varies from central to peripheral[77]. Although the diastolic and mean arterial pressures are relatively constant, systolic pressure can be up to 40 mmHg higher in the peripheral than the central artery[78]. This amplification effect on various parts of the body contains abundant information related to age, gender, height, heart rate and systematic diseases affecting the vasculature[79]. These data, if carefully collected, can be critical for improving the efficacy of diagnosis and prognosis of cardiovascular diseases[80]. However, in current clinical settings, such valuable data and signals can only be obtained by a professional clinician in a quite infrequent manner.

Our device allows observation of this intriguing phenomenon. The amplification effect will increase as we move from the large and highly elastic central arteries (for example, the carotid) to the small and stiff peripheral arteries (for example, the radial and dorsalis pedis) (Fig. 44, first row). This phenomenon is due to backward propagation of pulse waves generated at arterioles. At central sites, the reflected pulses need to travel a long distance, so they add to the central blood pressure waveform in a misaligned manner. At peripheral sites, however, they travel a much shorter distance, so instantly contribute to the peripheral blood pressure waveform in a way that is time-aligned. Therefore, the more peripheral the artery is, the higher the

amplification/augmentation will be (Fig. 44, second row). To validate this amplification effect, we used a commercial tonometer to test the same subject. Remarkably corresponding results are shown in the third row of Figure 44. An exciting feature contributed by this direct diameter measurement approach is that it allows observation of this amplification phenomenon and derivation of accurate pulse pressure values from multiple body parts simultaneously from diastolic pressure at only the brachial site, with no site mismatch. The upstroke gradient increases as a result of the pressure amplification.

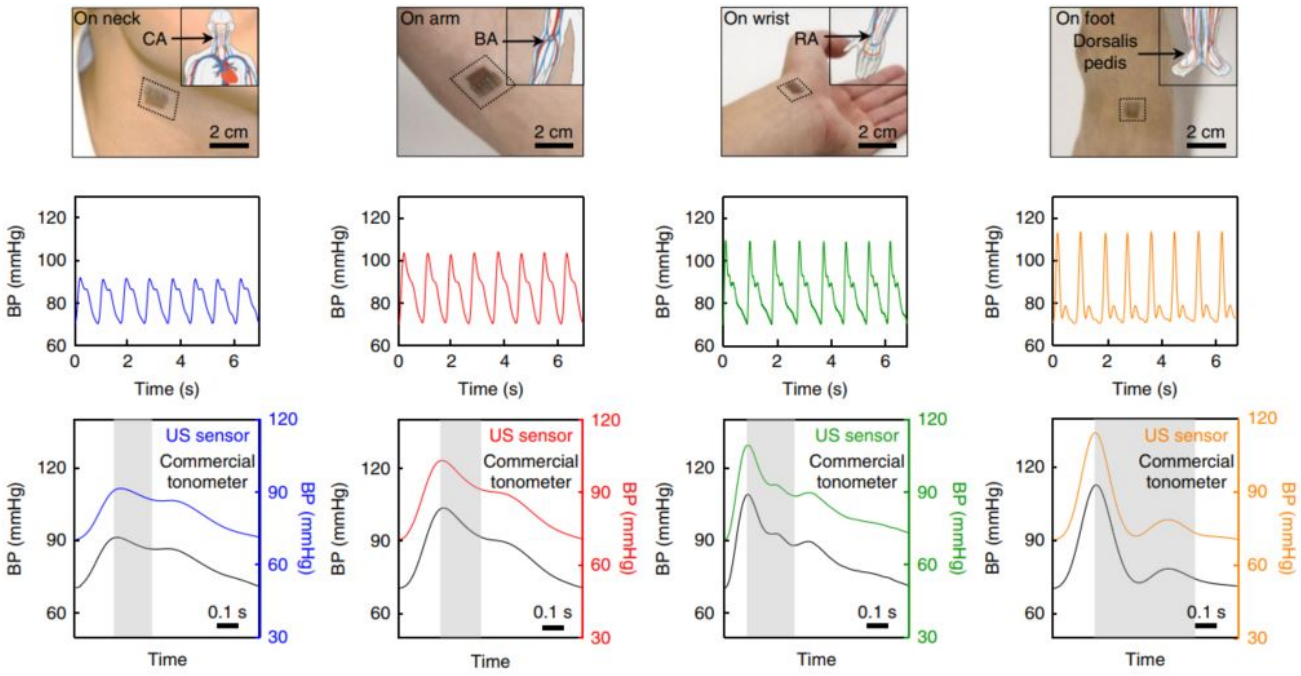

Figure 44. Blood pressure measurements from the central to peripheral arteries and validation using a commercial tonometer. Measurement positions (top row), collected arterial pressure waveforms (middle row) and the blood pressure waveforms of one period compared with the results from the tonometer (bottom row). Columns (left to right): carotid artery (CA), brachial artery (BA), radial artery (RA) and pedal artery (dorsalis pedis), respectively, showing an increase in amplification effect by progressive vascular resistance, longer interval time between the systolic peak and the dicrotic notch (grey areas), higher systolic pressure and higher upstroke gradient (the slope of the blood pressure waveform at the beginning of the upstroke).

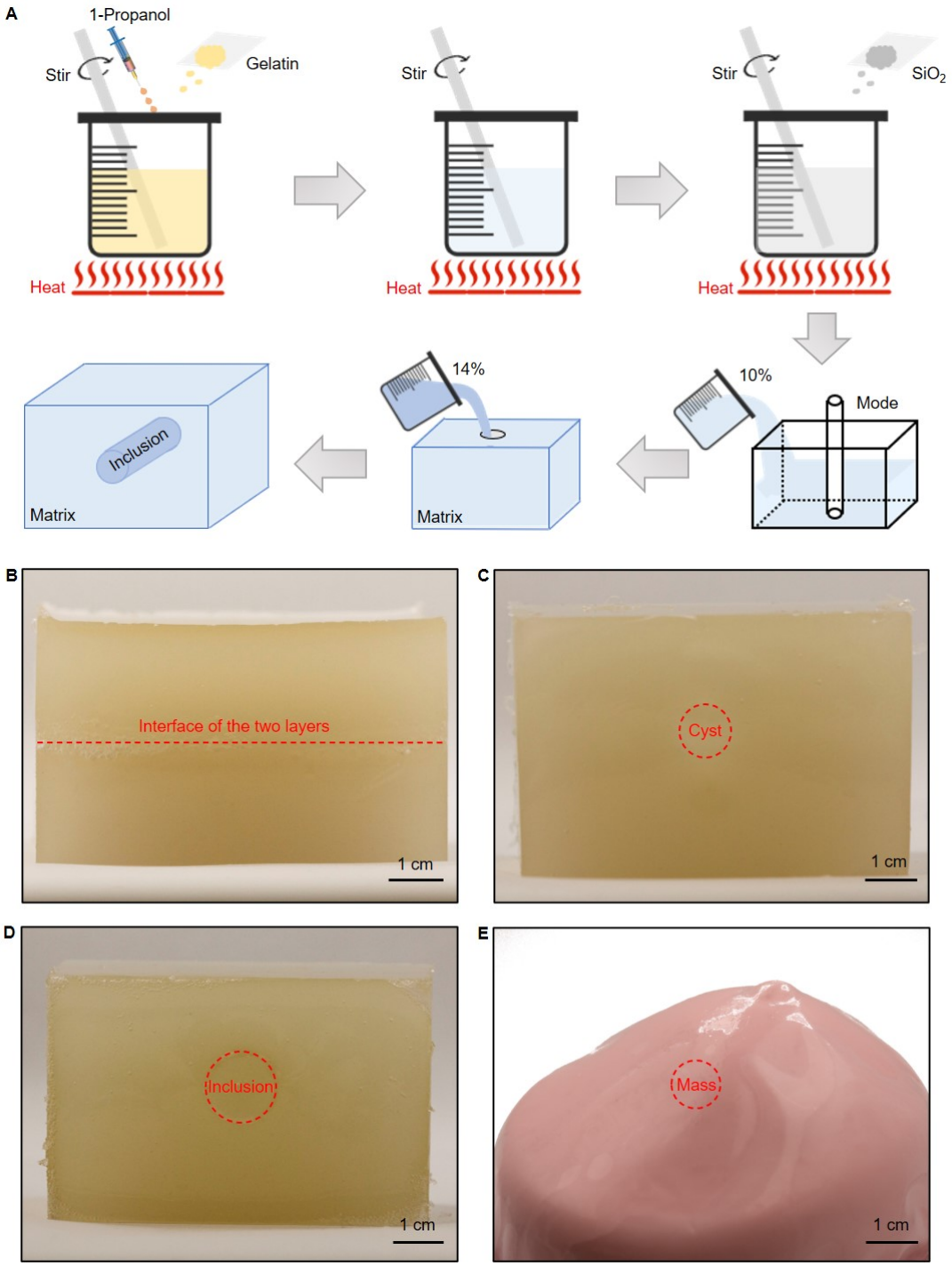

Figure 45. Fabrication processes and optical images of tissue-mimic phantoms. (A) The tissue-mimic phantoms are made of gelatin and silicon dioxide particles. Optical images of (B) a bilayer phantom, (C) a phantom with cyst (fluid inside), (D) a phantom with inclusion (solid inside), (E) a commercial 1436 breast phantom with a mass inside (CIRS Model 059), corresponding to 1D, 2D, 2D, and 3D biological tissue elasticity models, respectively.

Another notable feature of the blood pressure waveforms is the progressive time interval between the systolic peak and the dicrotic notch, which is illustrated by the grey areas in Figure 44. When the pressure wave travels down from the central arteries, its magnitude increases due to impedance mismatches encountered on the way, creating a reflected wave that travels back to the heart during late systole and early diastole. This reflection wave takes a longer time to travel from a location that is more distant from the heart, and thus contributes to an increase in the time interval between the systolic peak and the dicrotic notch (grey areas in the waveforms in Fig. 44, third row)[81]. The capability of capturing those systemic variations demonstrates the device's potential for accurate clinically relevant diagnosis.

4.2 Three-Dimensional Mapping of Deep Tissue Modulus.

Following the clinical practice for tumor screening and diagnosis, we used four types of phantoms to simulate different pathological tissue environments (Fig. 45)[71,82]: a one-dimensional (1D) phantom consisting of two layers with different Young's moduli, which mimics muscles with an area of disease or injury[83,84]; a 2D phantom consisting of a cylindrical cavity filled with fluid, which simulates the cysts that frequently appear in central organs[85]; a 2D phantom with a solid cylindrical inclusion; and a commercial 3D breast phantom with a spherical mass. The last two phantoms mimic tumors and nodes with various morphologies in the breast[86]. Young's moduli of all components have been characterized by either standard apparatus or a clinical ultrasound machine. Many masses (except for the cyst phantom) have materials and constituents, and thus

acoustic impedances, similar to the surrounding tissues. Thus, they exhibit a homogeneous echogenicity and a minimal sonographic contrast that can hardly be distinguished by B-mode imaging (Fig. 46A-D, first column)[87,88].

The tests on phantom models focus on the axial displacement fields (Fig. 46A-D, second column). This is because compared with the lateral and elevational displacements, the axial displacements can reflect the movement of each scattering source more accurately, since it is parallel to the direction of ultrasonic wave transmission[89]. The strain is higher when the modulus of the component is lower (the third column in Fig. 46A-D). A common practice for computing strain is to take the spatial derivative of the displacement field[90], which amplifies small fluctuations in the displacement field (Fig. 47). To remedy this problem, we applied a least-squares strain estimator with a piecewise linear curve fitting method, which allows us to calculate the 2D strain distributions while smoothing unphysical fluctuations (Fig. 47)[91]. The resulting strain distributions clearly reveal the inclusion. An exception is the cyst phantom, whose strain distribution map has a blue-green-red region (Fig. 46B and Fig. 48), a signature of cysts that has been used clinically to distinguish between cystic and solid lesions[85,92]. To evaluate the resolution of the stretchable ultrasonic array in the elevation direction, we reconstructed 3D strain images of the phantoms by integrating 16 cross-sectional images obtained by the stretchable array. The 3D imaging results match those of a commercial ultrasound probe with a similar center frequency (2.8 MHz) (Figs.

49-50). The measurements are highly reproducible, reflecting the reliability of the stretchable array (Fig. 51).

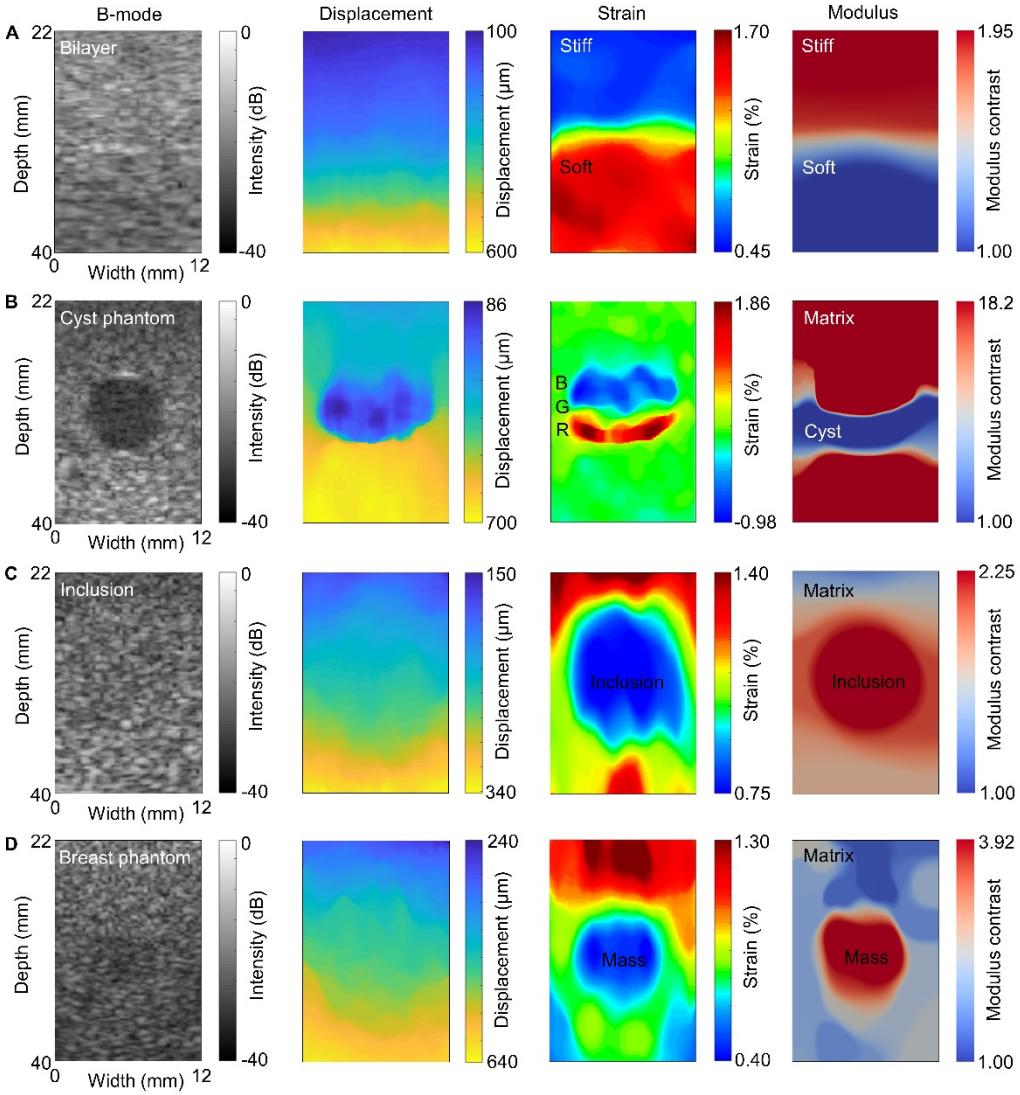

Figure 46. Characterizations on phantom models. Four types of phantoms are used to simulate different pathological tissue environments: (A) a bilayer phantom where the top layer is 2.03 times stiffer than the bottom layer, (B) a cyst phantom consisting of a cylindrical cavity filled with fluid, phantoms with (C) a cylindrical inclusion that is 1.61 times stiffer than the matrix and (D) a spherical mass that is 2.54 times stiffer than the matrix. B-mode images of all phantoms acquired by a commercial ultrasound probe are shown in the first column. Displacement fields estimating the motion of each scattering source in the phantoms during compression are shown in the second column. The ultrasonic array's position is defined as the origin. Corresponding strain distributions are shown in the third column. Solving the inverse elasticity problem with the displacement distributions yields quantitative modulus contrasts, shown in the fourth column.

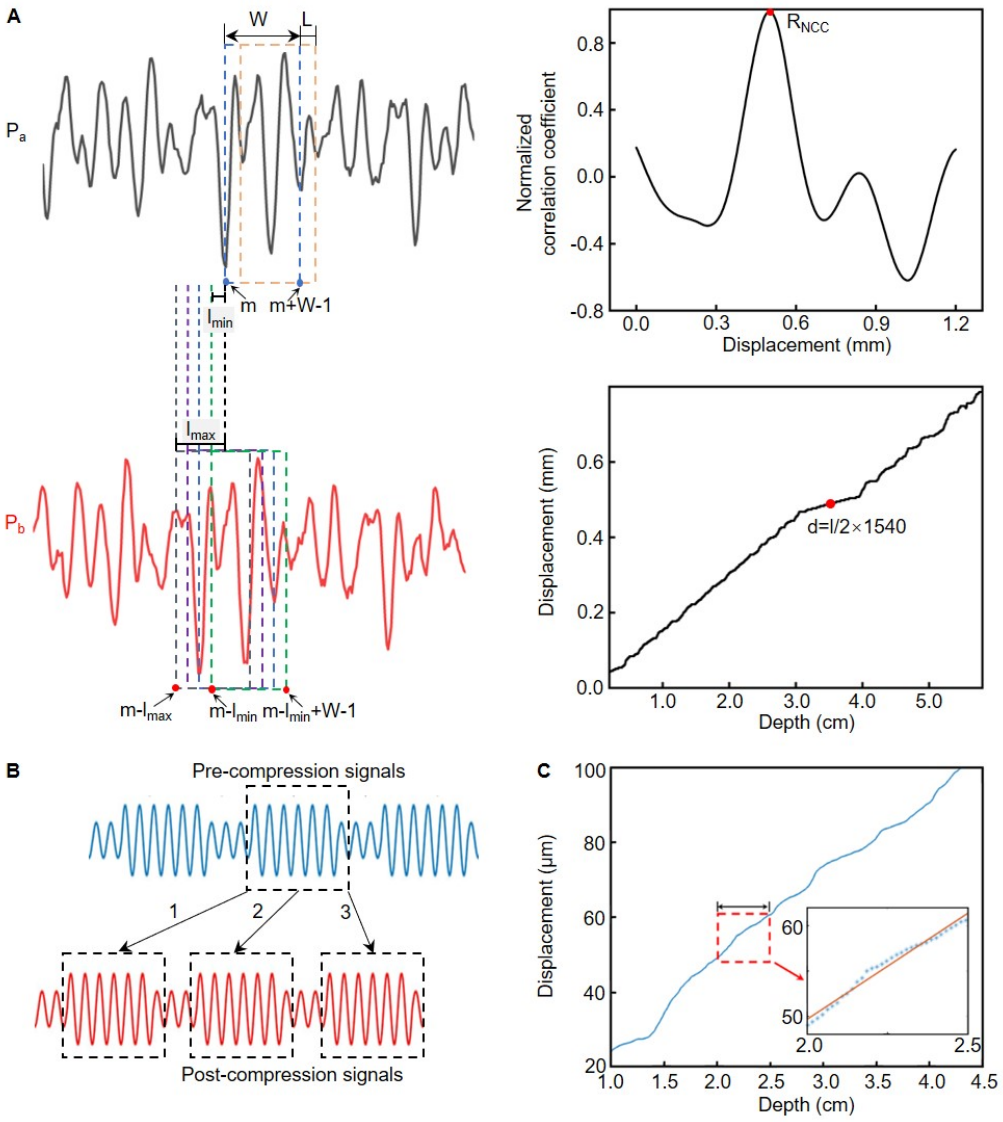

Figure 47. Illustration of the normalized cross-correlation and least-squares strain estimator algorithms. (A) The process of displacement calculation. Sliding windows are applied to correlate the beamformed RF signals before and after compression. The displacement at a certain depth is defined as the one with the highest normalized correlation coefficient among all compared windows (top right panel). The displacement curve is derived by combing all displacement values along the depths (lower right panel). (B) A schematic figure showing the source of fluctuations in the displacement curve. Signals in windows 1, 2, and 3 are adjacent to each other. After compression, the pre-compression signals may correlate signals from window 1, or 2, or 3 since they are very similar and the corresponding correlation coefficients are almost the same. It causes some confusion to the normalized cross-correlation algorithm and thus leads to tiny fluctuations in the displacement curve. (C) The displacement along the axial direction and a window used to estimate the local strain. The inset image illustrates the raw (blue dots) and the fitted displacements by a least-squares strain estimator (red line), which can smooth out the fluctuations in the displacement. The calculated strain is the slope of the fitted displacement curve.

Strain depends on applied loads and thus strain mapping can be subjective and operator-dependent. Additionally, strain maps cannot faithfully reveal quantitative modulus information if the load is non-uniform[93]. To avoid these issues, we quantified the spatial distribution of the shear modulus by solving an inverse elasticity problem[94]. Specifically, we formulated the inverse elasticity problem as a constrained optimization problem. The objective is to seek a shear modulus distribution that produces a predicted displacement field that satisfies the equilibrium equation of the 2D linear elasticity model[95] and matches the measured displacement field. We solve the optimization problem by a gradient-based minimization approach and compute the gradient efficiently using the adjoint method (Fig. 52)[94]. The Young's modulus distribution is three times the shear modulus distribution[96,97]. For a measured displacement field, the derived modulus distribution can be accurately determined, regardless of whether the load is uniform.

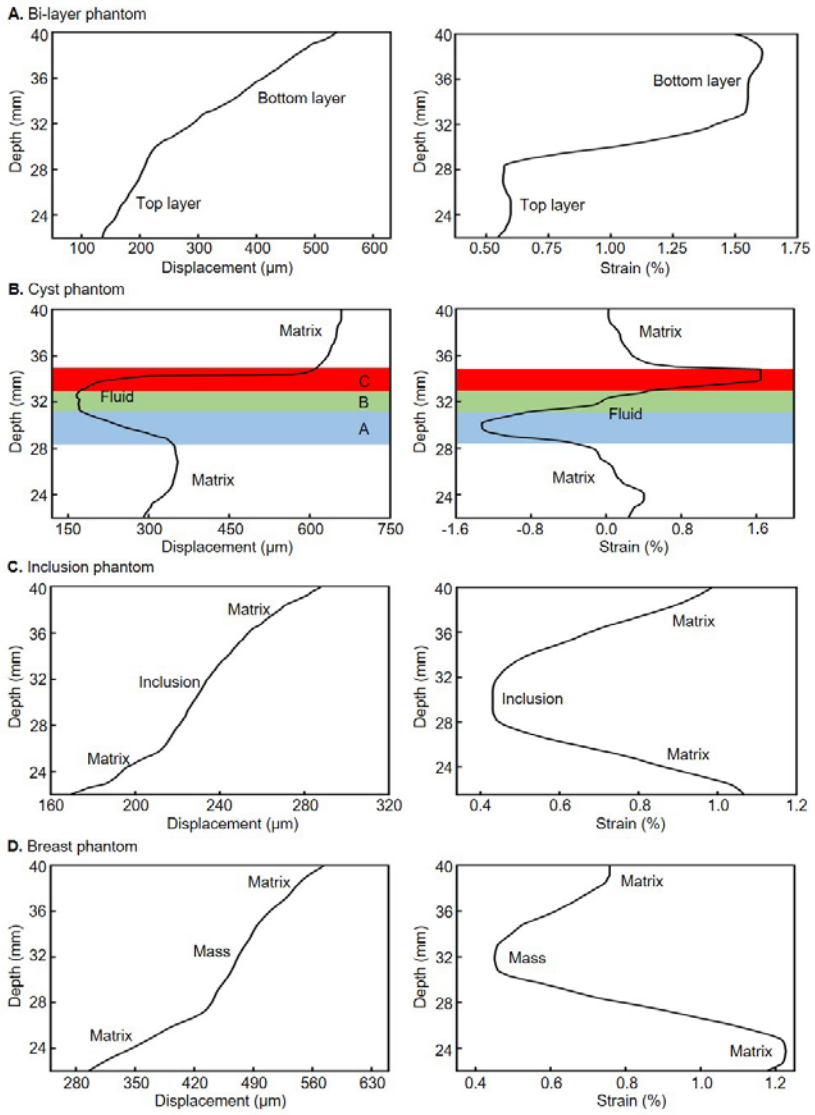

Figure 48. Displacement and strain curves at the central lines of different phantoms. The displacement (left column) and strain curves (right column) of (A) a bi-layer phantom, (B) a cyst phantom, (C) an inclusion phantom, and (D) a breast phantom. The slope of the displacement curve of each component generally does not vary with the thickness, indicating the uniform Young's modulus of each component. The least-squares strain estimator with a piecewise linear curve fitting transforms the displacement to the strain. These curves at the central lines clearly show the difference in displacement and strain of each component in the phantoms. Particularly, the blue-green-red regions in the cyst phantom is a unique artifact in cysts. The cyst region is devoid of echoes and mere random noises are detected, causing the displacements to be very small. The section where the large displacement transits to the small displacement produces a large negative strain due to the slope change in the displacement curve ("A" region, blue artifacts). The small displacement generates close to zero strain ("B" region, green artifacts). And the transition section where the displacement raises from small to large yields large positive strain ("C" region, red artifacts).

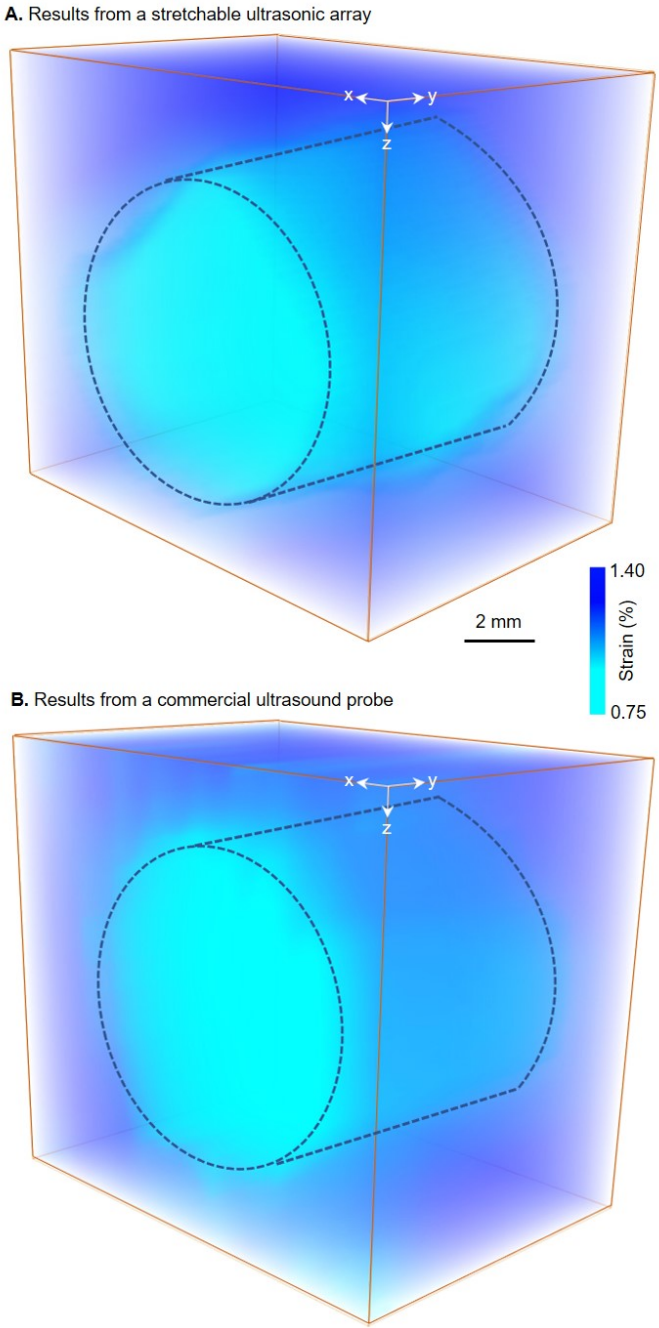

Figure 49. 3D strain images of an inclusion phantom by the stretchable and commercial ultrasonic probes. The 3D strain images tested by (A) the stretchable ultrasonic array and (B) a commercial ultrasound probe show high correspondence to each other in size, geometry, and strain distribution of the inclusion phantom. Both figures share the same color bar and scale bar.

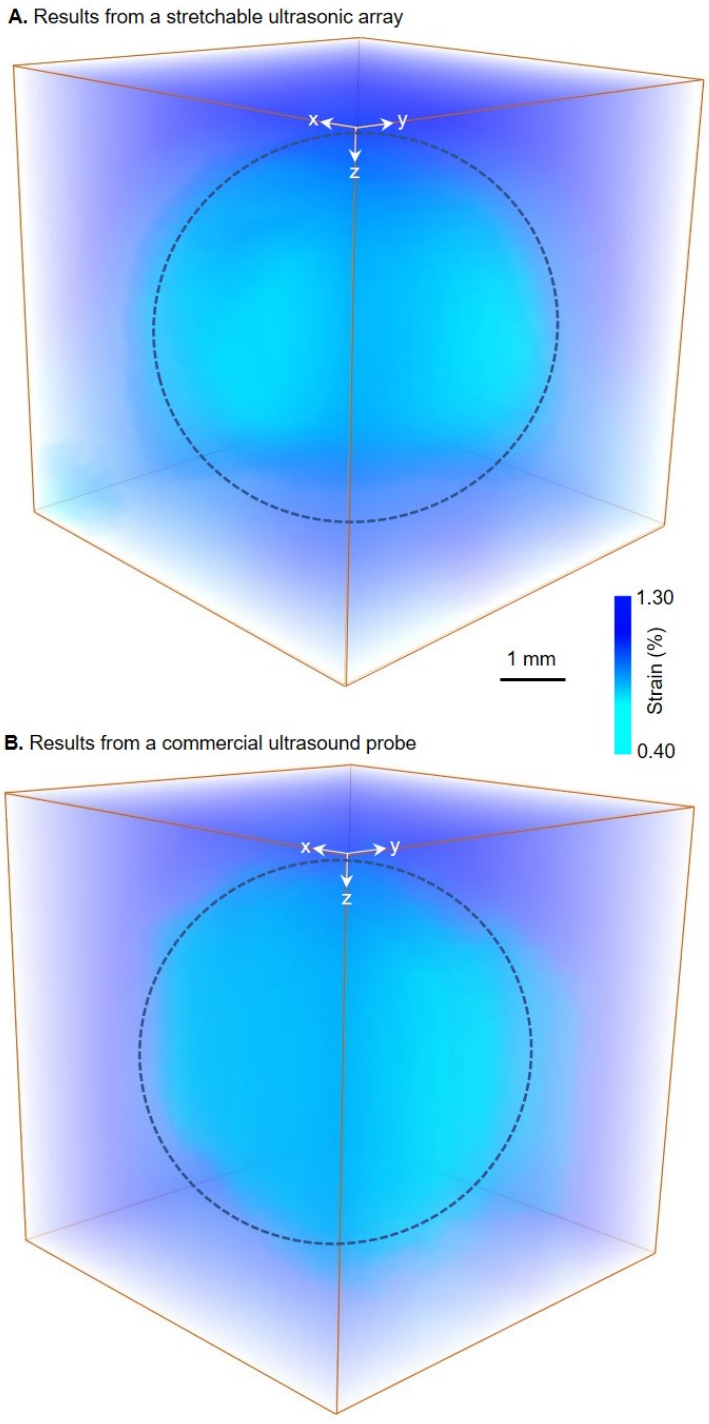

Figure 50. 3D strain images of the commercial breast phantom by the stretchable and commercial ultrasonic probes. The results by (A) the stretchable ultrasonic array and (B) the commercial ultrasound probe show high correspondence to each other in size, geometry, and strain distribution of the breast phantom. Both figures share the same color bar and scale bar.

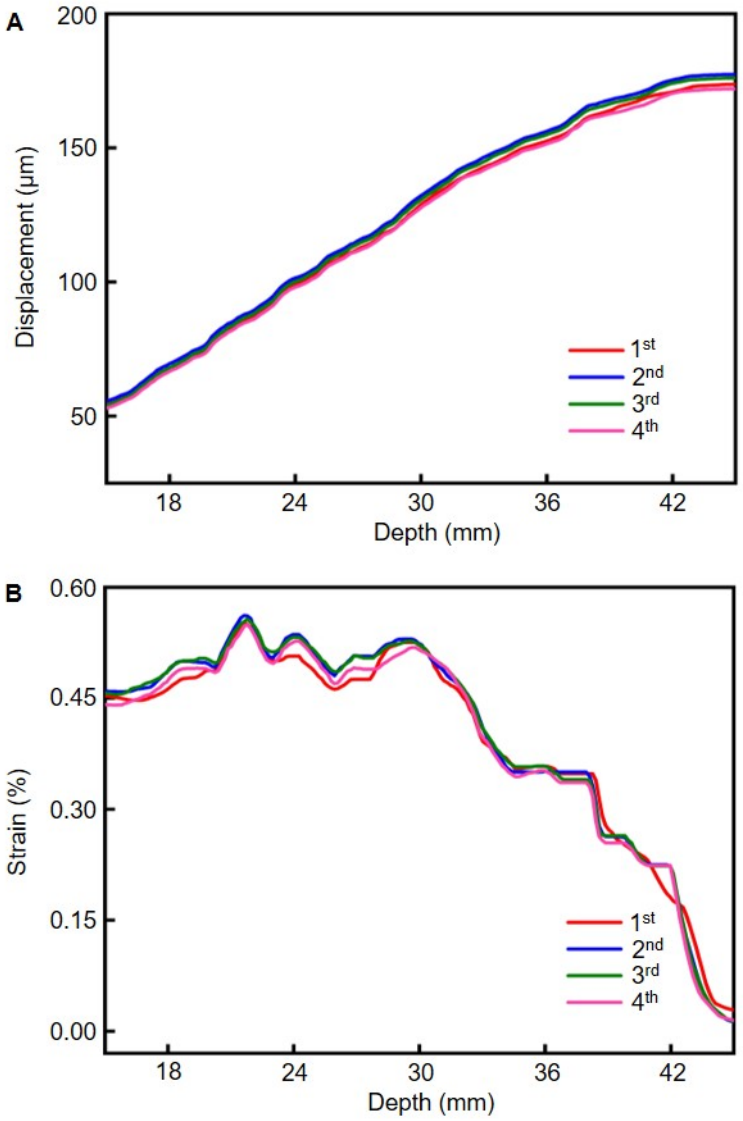

Figure 51. Repetitive tests. Measurements of (A) the displacement and (B) the strain of a phantom for four times. There is a three-minute interval between each measurement to allow the phantom to relax from the compressive to the original states. These measurements are highly reproducible.

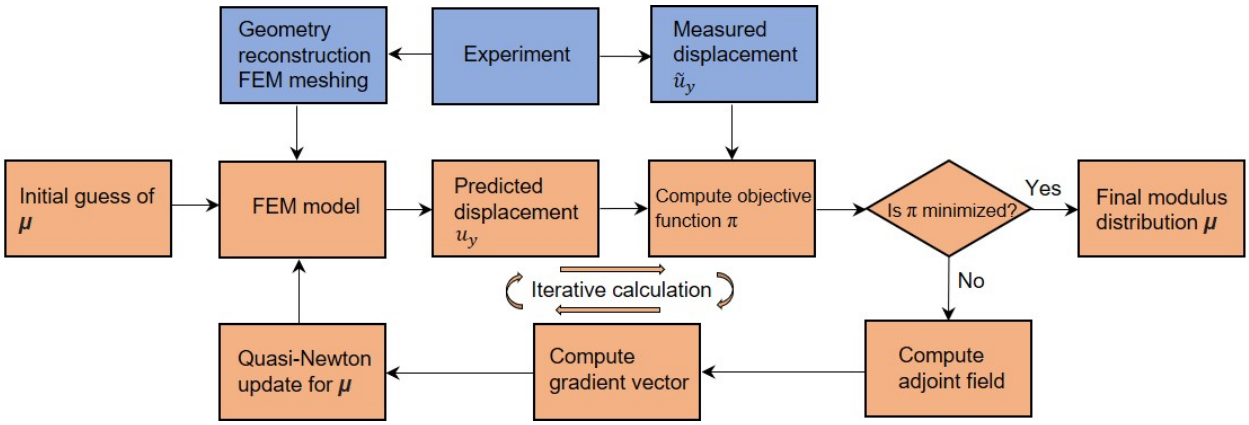

Figure 52. Flow chart of the process for calculating the inverse elasticity problem. Orange boxes demonstrate the workflow of calculating the inverse elasticity problem. Blue boxes demonstrate the interaction of the inverse elasticity problem with the experimental system. μ: modulus distribution; $\boldsymbol{u_y}$: the predicted displacement field; $\boldsymbol{\tilde{u}_y}$: the measured displacement field; π: the objective function.

The modulus distribution maps visualize the morphology of the internal structures, which accurately match the design (the fourth column of Fig. 46A-D). Shadowing artifacts, usually caused by inclusions, do not appear in the elastograms here, because of the high transmission energy of the coherent compounding method and the excellent sonographic sensitivity of the stretchable ultrasonic array. The mean modulus contrasts between the stiff and soft components of the bilayer, inclusion, and breast phantoms are 1.94, 1.50, and 2.21, with a difference of 4.59%, 6.81%, and 12.78%, respectively, from those obtained by a standard apparatus. Note that for the cyst phantom, the acquired values only indicate that the stiffness of the cyst is much lower than that of the surrounding matrix, and do not represent the exact modulus ratios[98]. There is a slight underestimation of modulus contrast in all cases because the total variation regularization used to solve the inverse elasticity problem tends to sacrifice the contrast in order to generate less noisy images (Fig. 53)[99]. The overall >87% accuracy of the results here is well above the average

accuracy of 80% in the literature[100], because of the outstanding transducer performance and the advanced coherent compounding approach.

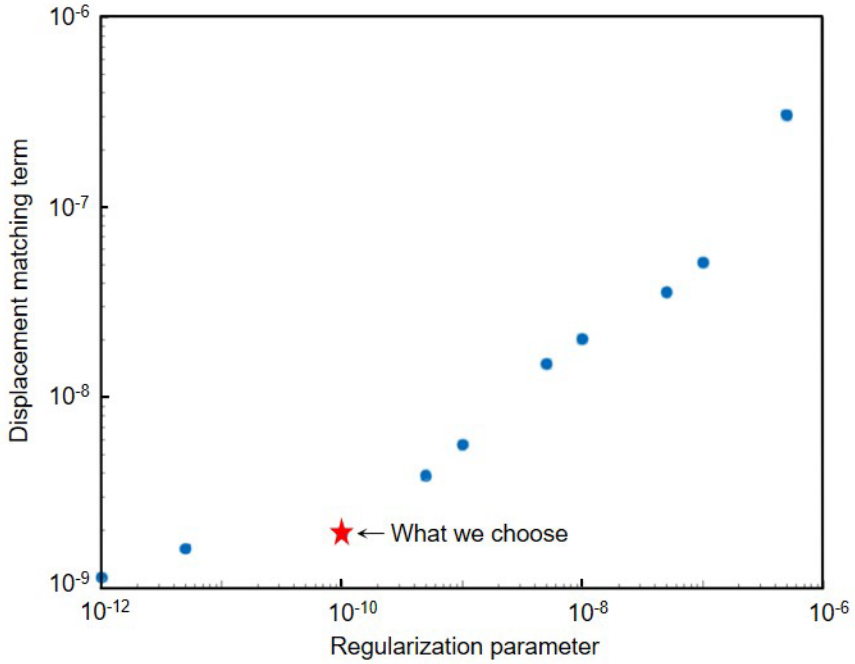

Figure 53. The L-curve of calculating the inverse elasticity problem. An appropriate regularization parameter is required to reconstruct the displacement and modulus ratio fields. When selecting a large regularization parameter, the field will be very smooth but with small modulus contrast; and vice versa. In this work, we use 1×10-10 to optimally harmonize the levels of smoothness and contrast to get the best matching of the measured and predicted results.

We validated the 3D imaging performance of the stretchable array against MRE on porcine abdominal tissues 4 cm thick with a multilayer structure[101]. Each 1×16 linear array on the ultrasonic patch can map a 2D cross-sectional displacement field and the corresponding modulus distribution. A 3D elastographic image is portrayed by integrating 16 slices of modulus maps with a 0.8 mm pitch (Fig. 54), with an average discrepancy between measured and predicted displacement fields of 3% (Fig.55). The 3D image illustrates the heterogeneous nature of the soft

tissue. The same porcine abdominal tissue is then measured by MRE (Fig. 56). The volumetric mapping result from the stretchable array is highly comparable to that from MRE in both morphology and modulus distribution. The average measured modulus contrasts of transversus abdominis muscle, obliquus internus abdominis muscle, fascia, and intermuscular fat are approximately 1.92:1.67:1.30:1 by the stretchable array, and 2.26:1.83:1.46:1 by MRE; both are comparable to those in the literature[102,103].

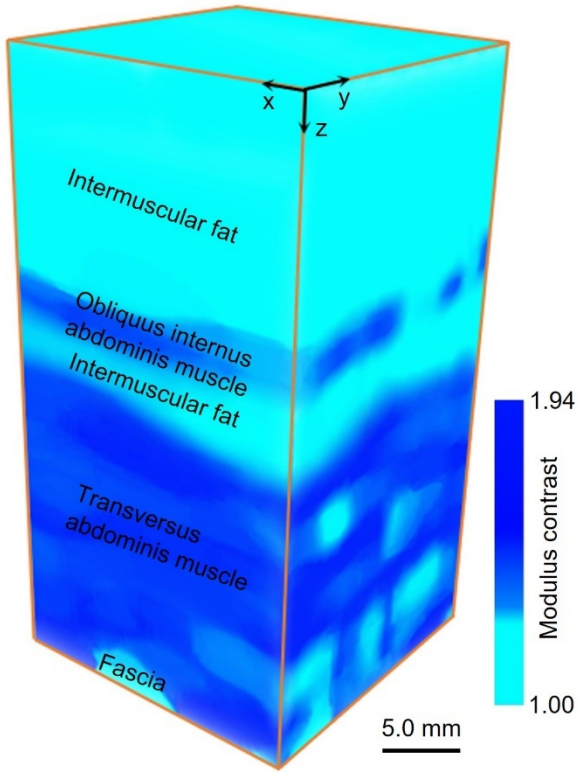

Figure 54. A 3D quantitative elastographic image of a porcine abdominal tissue by the stretchable ultrasonic array. In the tissue, two muscle layers intersect with the intermuscular fat, and the fascia are embedded in the transversus abdominis muscle. The 3D elastogram embodies homogeneous, lower modulus fat layers made of glycerol and fatty acids molecules, and relatively heterogeneous, muscle groups with higher modulus made from criss-crossing and confluence fibers.

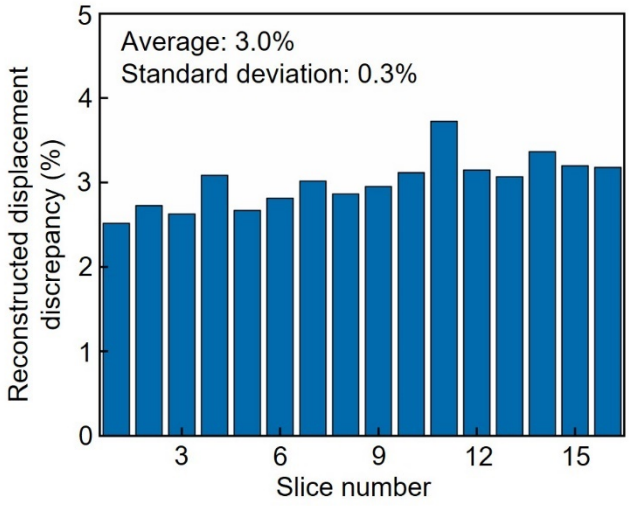

Figure 55. The averaged 3% discrepancy of the 16 pairs of measured and predicted displacement fields, with a high degree of correspondence between the reconstructed mechanical model by solving the inverse elasticity problem and the experimental conditions, suggesting a robust foundation for yielding the accurate modulus distributions.

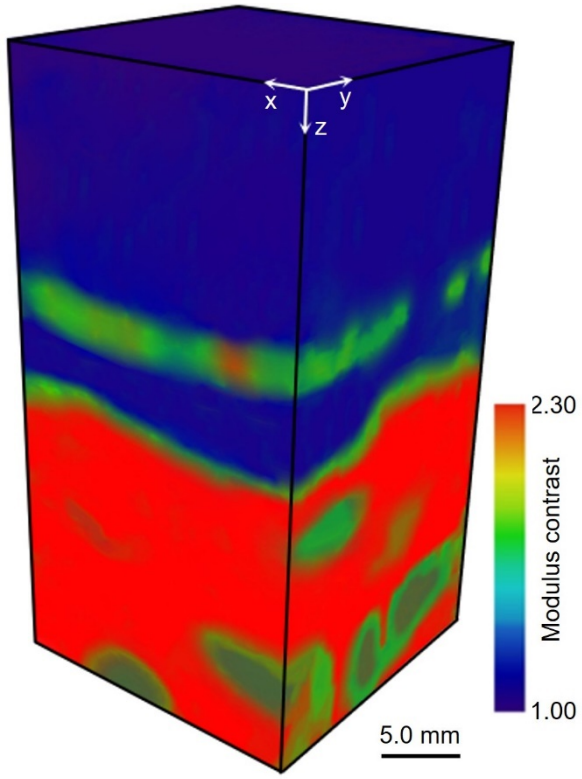

Figure 56. A 3D MRE image of the porcine abdominal tissue.

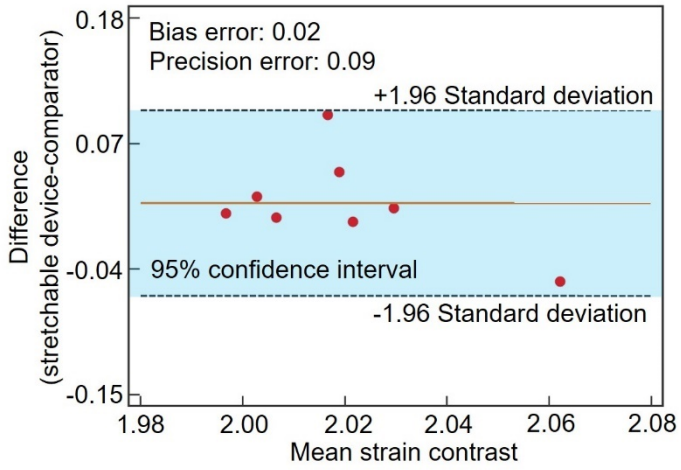

Figure 57. Bland-Altman analysis of the strain contrast of a commercial breast phantom for eight weeks. Each data point represents the difference in the measured strain contrasts between the stretchable ultrasonic array and the commercial probe.

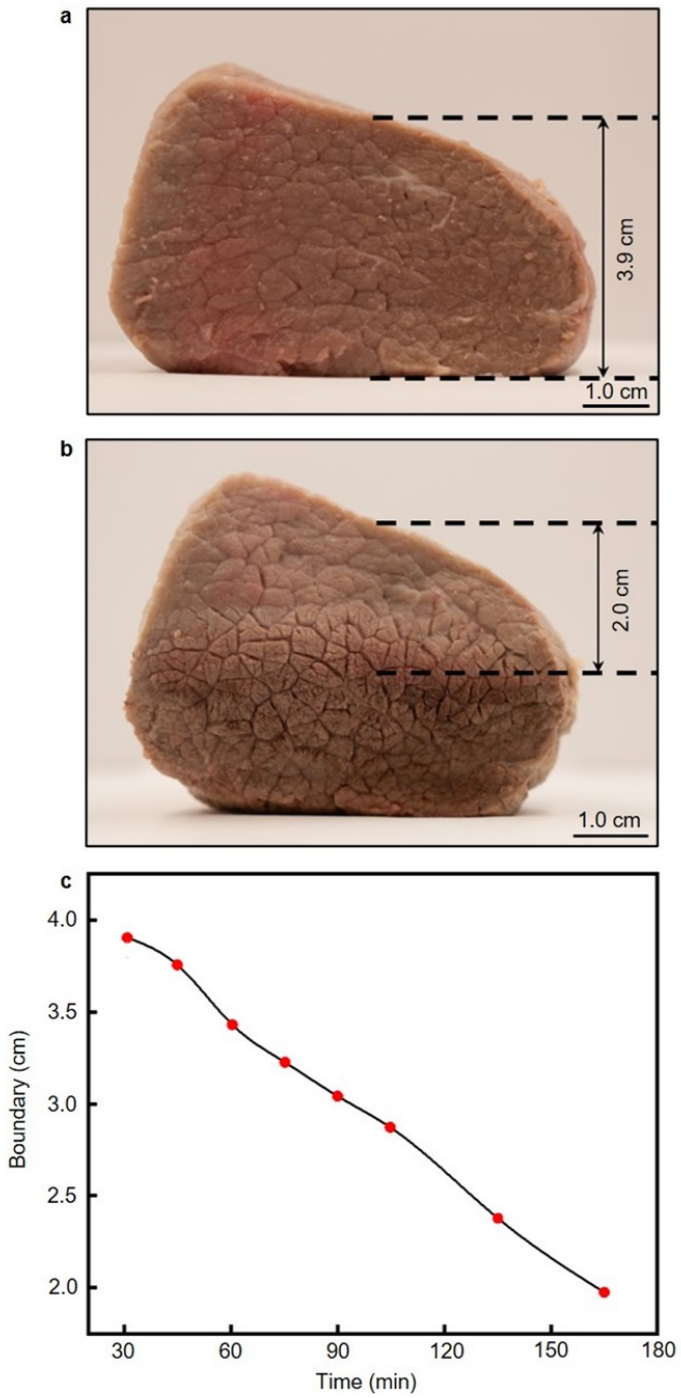

Figure 58. Serial monitoring of the modulus evolution of a bovine gluteobiceps muscle. Optical images of the bovine gluteobiceps muscle (A) before and (B) after heating for 165 mins. The total thickness of the testing part is 3.9 cm. After heating, part of the specimen is stiffened, as evidenced by the boundary between stiff and soft tissues. (C) The boundary locations are plotted with the heating time. The probe position is defined as the origin.

A method for serial surveillance applications needs to be stable for long-term reproducibility, with a high sensitivity for picking up dynamic changes in the target tissue. A longitudinal study is carried out by testing a commercial phantom with the stretchable ultrasonic array and a commercial probe over eight weeks. We compared the strain contrast between the mass and matrix measured by the two methods and conducted Bland-Altman analysis. All data points have a 95% confidence interval with a small bias error of 0.02, demonstrating that the precision and accuracy of the stretchable device is comparable to the commercial probe (Fig. 57). A small precision error of 0.09 indicates the stability of the stretchable array for serial measurements over the long term. To test the elastographic sensitivity of the stretchable array, we measured a piece of bovine gluteobiceps muscle under controlled unilateral heating as its modulus gradually increases (Fig. 58). The measurement lasted for 165 minutes. The results clearly show that before heating, the tissue has a low modulus across the entire depth (Fig. 59). When heated from the bottom, the region of the tissue close to the heat source started to stiffen, because the actin in the myofibrils becomes firm and short, expelling liquid and making the structure dense[104]. As the heating continues, the high-modulus region gradually grows, while the boundary between the high- and low-modulus regions remains clearly defined. These recordings demonstrate the capability of the stretchable array for serial monitoring of deep tissue mechanics.

In vivo measurements can further illustrate the clinical value of the stretchable ultrasonic array. Multiple sites on the human body where muscle injuries usually happen were selected in this study. Figure 60A-D presents the results of the strain mapping within 4 cm depth from the

lateral side of the shoulder joint (Fig. 60A), the anterior forearm (Fig. 60B), the anterior thigh (Fig. 60C), and the posterior calf (Fig. 60D) with the anatomies labelled, juxtaposed with the corresponding B-mode images acquired by a commercial probe. The stretchable array can effectively resolve the mechanical properties of various tissue components.

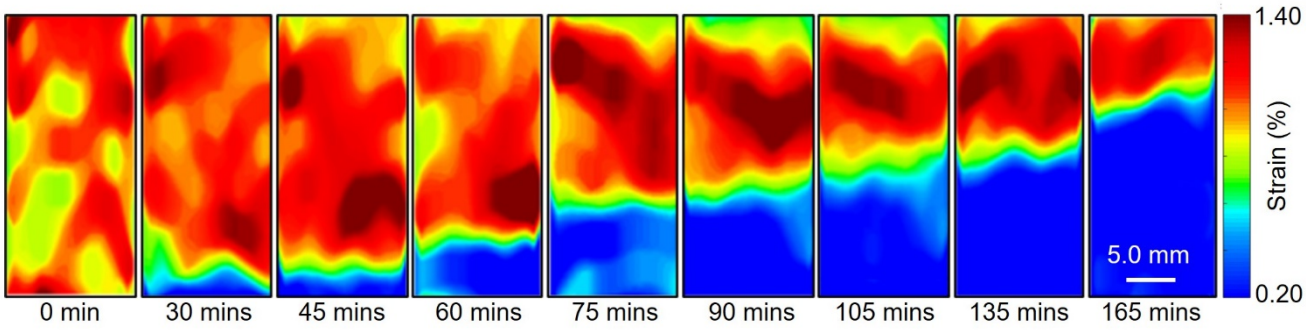

Figure 59. Time-dependent stiffness variation of a piece of bovine gluteobiceps muscle under heating.

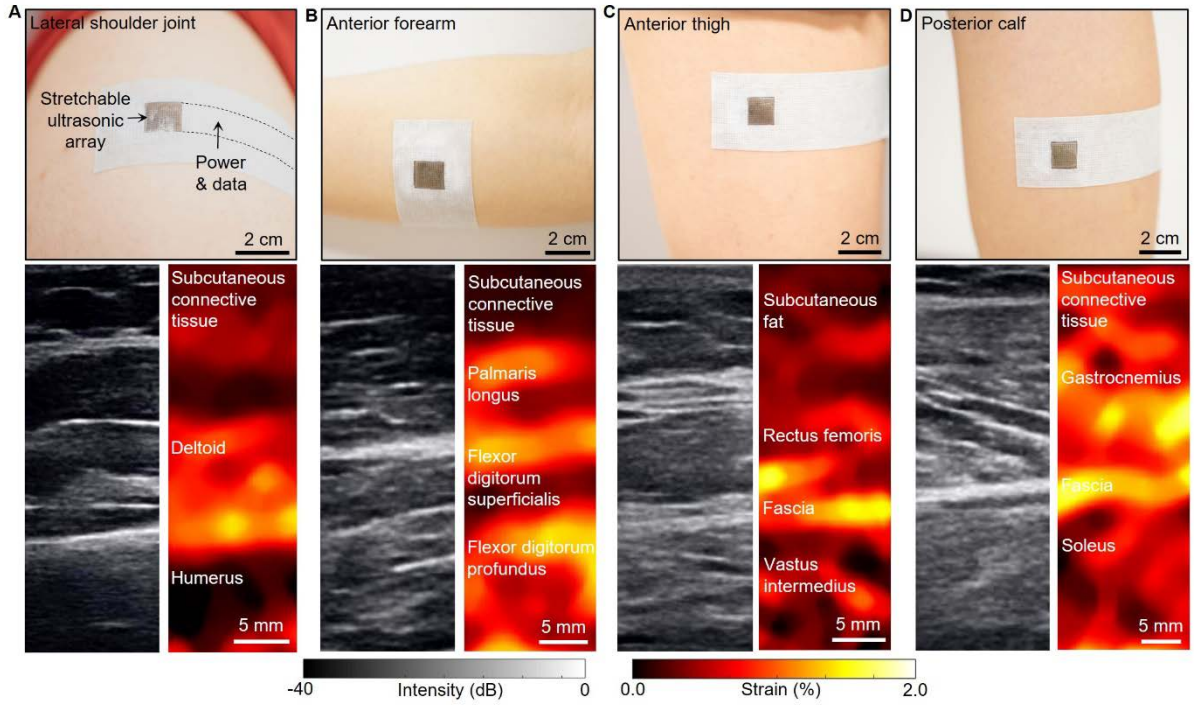

Figure 60. Multi-site mapping in human. Optical images, B-mode images, and corresponding strain mapping results of (A) a lateral shoulder joint, (B) an anterior forearm, (C) an anterior thigh, and (D) a posterior calf. Key anatomical structures are labelled in the strain images.

Over-exercise introduces injuries to the musculoskeletal systems, associated with damages in the sarcolemma and others[105]. These disruptions lead to inflammation, stiffness increase, and function impairment of the tissues[105]. Very often, the sensation of soreness doesn't occur until a few days later[106]. The delayed onset of body responses precludes timely treatments and the injury often gets neglected and worsens. Additionally, serial evaluation of the tissue can guide the rehabilitation strategy[107,108]. MRE is frequently used to evaluate the tissue's stiffness to diagnose tissue injuries[107,108]. However, it is only available for short-term testing due to its large footprint, limited availability, and high cost.

The stretchable ultrasonic array addresses these needs. A healthy volunteer was selected to perform the eccentric elbow joint exercise to develop delayed onset muscle soreness[109]. Before exercise, well-defined anatomic components of the upper arm can be visualized three-dimensionally (Fig. 61). After exercise, the muscles are either allowed to recover naturally, or treated with massotherapy or hyperthermia. In all experiments, the normalized modulus contrast of the biceps brachii was surveilled every day for five days to track the dynamic recovery process. Meanwhile, the intensity of the soreness was evaluated based on the pain visual analog scale[110] (Fig. 62).

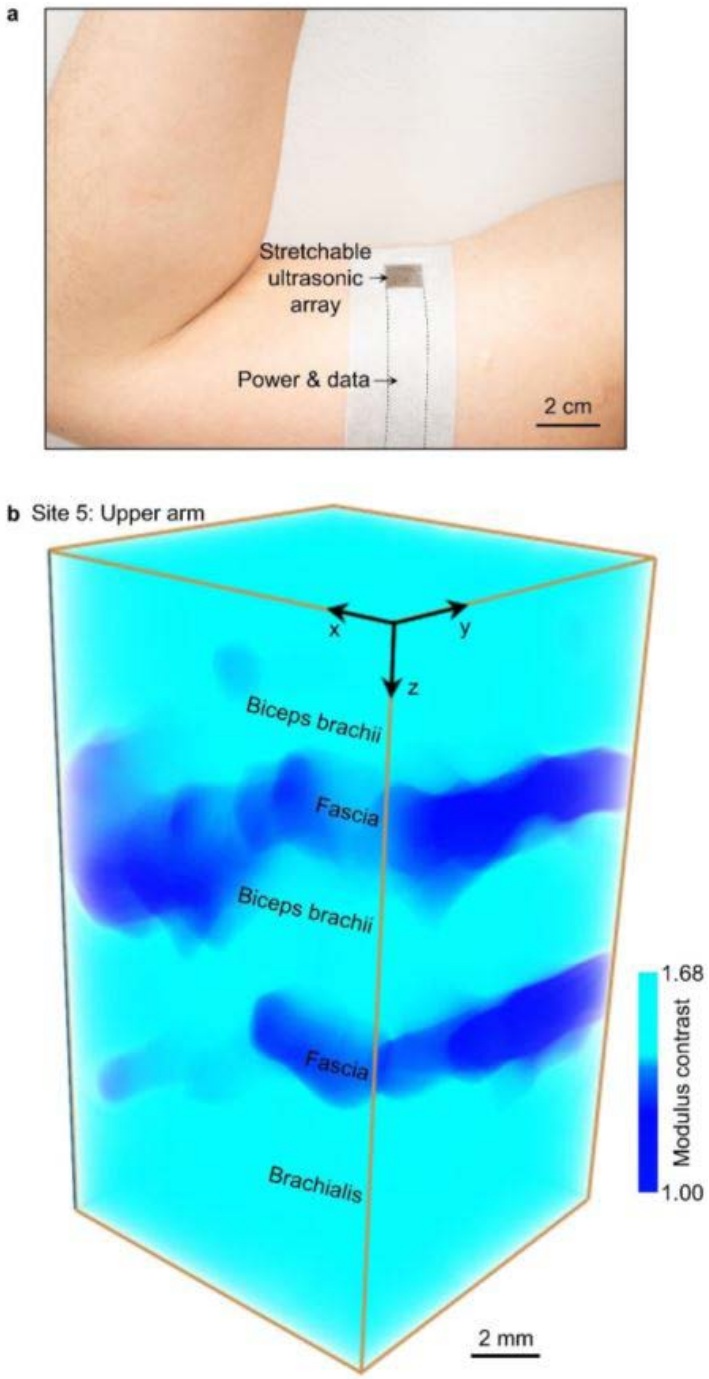

Figure 61. A 3D elastographic reconstruction of the upper arm. (A) An optical image showing the device and the testing position. (B) 3D modulus distribution of the upper arm mapped by the stretchable ultrasonic array.

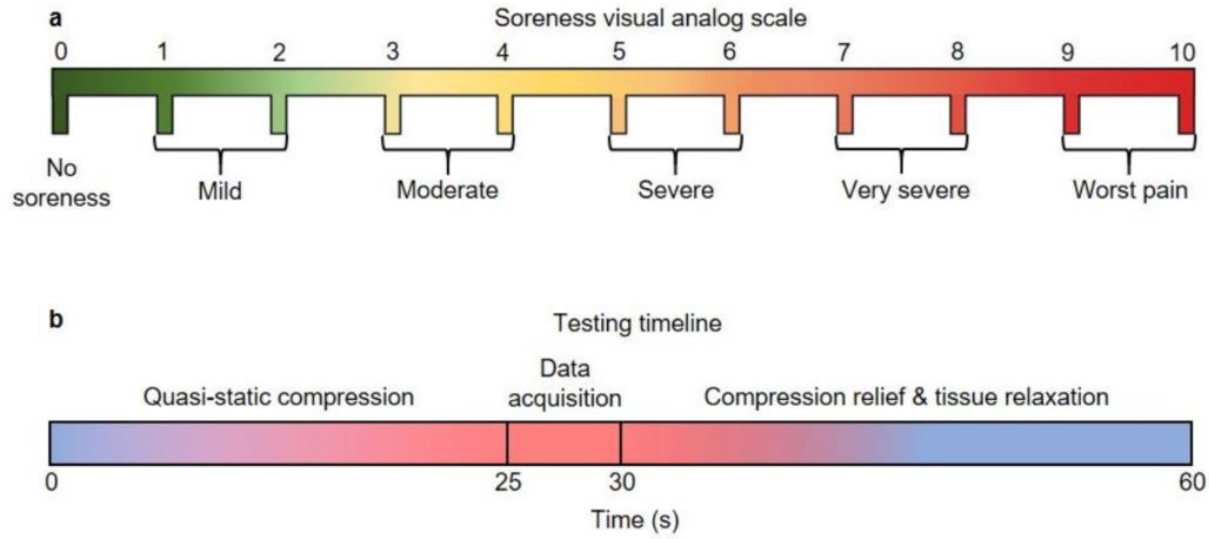

Figure 62. Soreness visual analog scale and testing protocol. (A) Soreness visual analog scale interpreting the corresponding scores for different levels of soreness. (B) The testing protocol with all steps labelled. The test begins with quasi-static compression, which takes about 25 seconds. Then, multiple frames of data are acquired with a frame rate of 1 Hz. In the following ~30 s, the compression is relieved to make tissue recover to the original state.

Figure 63 presents the monitoring results, where normalized modulus contrast (top) and soreness intensity score (bottom) of each measurement are collected. The modulus of biceps brachii increased within 20 minutes after the exercise due to the muscle contracture induced by sarcolemmal disruption[107,108]. However, the sensation of soreness did not arise until one day after exercise[111]. As more time goes by, sarcolemmal disruption continued, and the muscle modulus kept increasing. Meanwhile, the circulation system delivered supplies to repair the sarcolemma, and eventually tissue modulus dropped[112]. During natural recovery, the muscle modulus continued to increase for two days before dropping. When physiotherapies are applied, the increase only sustained for one day, with lower maximum moduli. The intensity of soreness has a latency but evolves in a trend similar to the modulus. On the fifth day, the normalized modulus contrast and

soreness intensity with physiotherapies are lower than those with natural recovery. Additionally, blood cannot circulate well through the injured myofibrils, leading to involuntary tremors of the muscle during testing[113], which induces variations in the measurement results. The coefficient of variation of the modulus, defined as the ratio of the standard deviation to the mean, is smaller for physiotherapies than that of the natural recovery (Fig. 64). These collective results confirm that the physiotherapies promote efficient circulation, expediting the delivery of supplies to the lesion for muscle recovery[112]. Hyperthermia has slightly higher efficacy than massotherapy in this study. Wearing the device one hour a day for five days did not induce any skin irritation (Fig. 65).

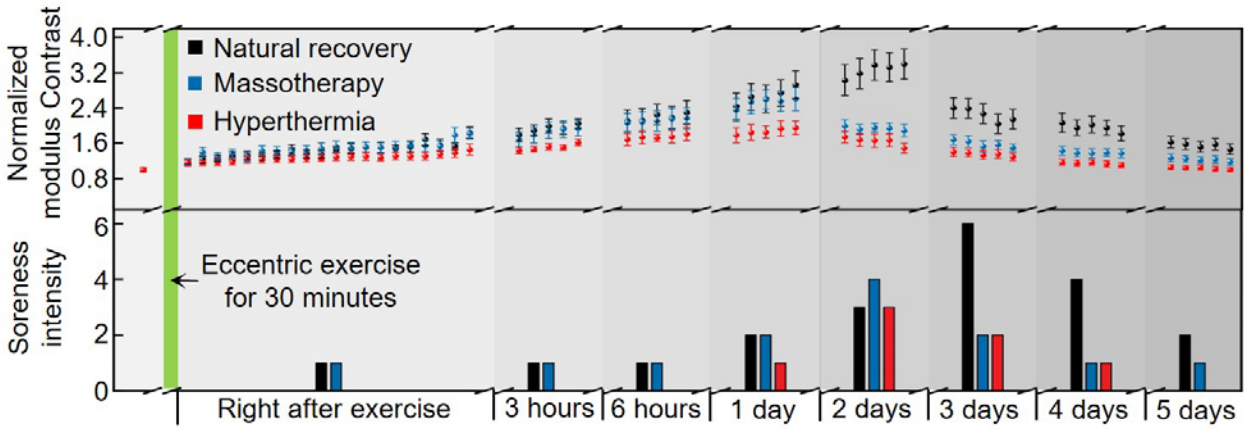

Figure 63. Serial monitoring results of normalized modulus contrast and soreness intensity of the biceps brachii muscle before and after the eccentric exercise. At the top panel, each point and error bar indicate the mean and standard deviation of modulus contrast of the biceps brachii muscle of every test. The time interval between adjacent tests is one minute. At the bottom panel, soreness scores were evaluated following the pain visual analog scale.

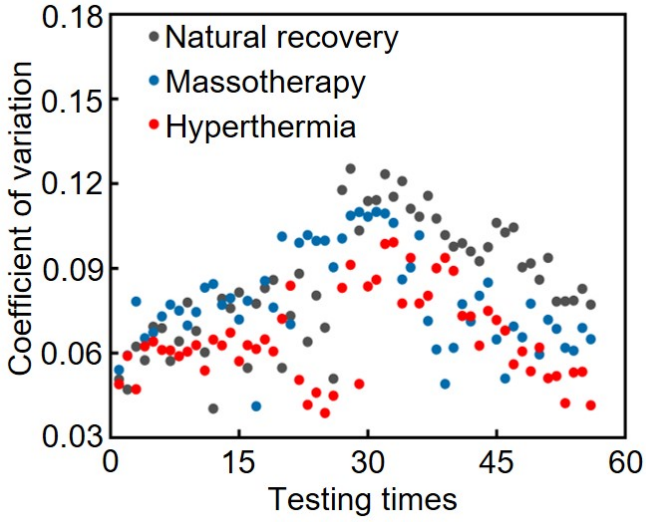

Figure 64. Coefficient of variation among all tests.

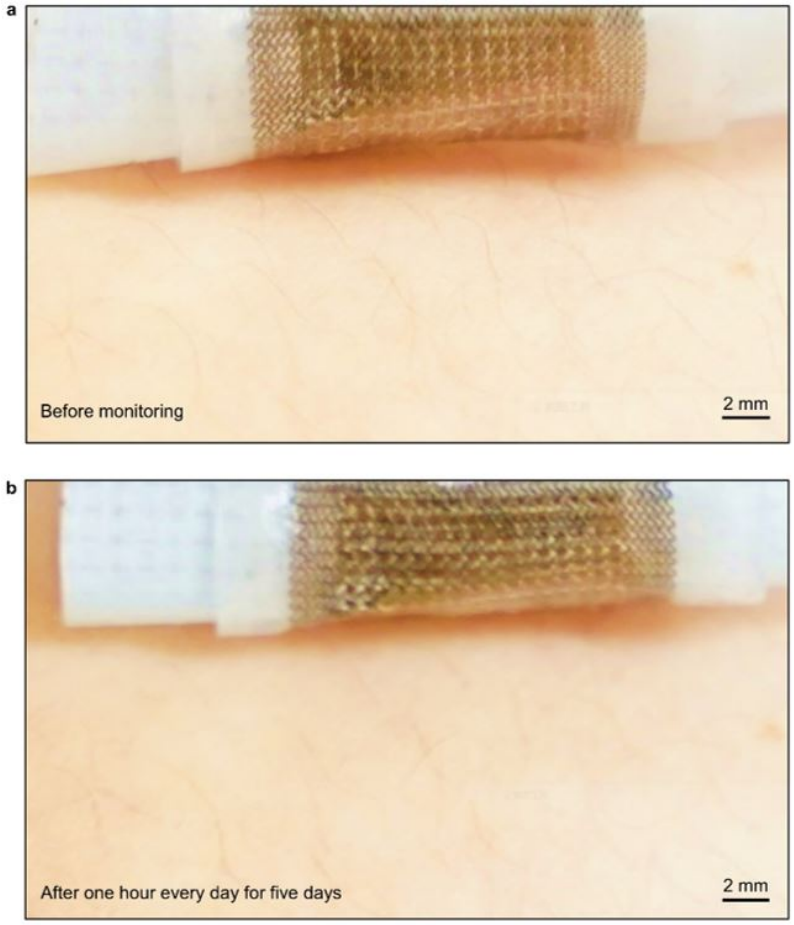

Figure 65. Optical images of skin before and after monitoring. The device was mounted on the upper arm one hour every day for five days. No obvious skin irritation occurs, showing that the device is appropriate for long-time monitoring.

4.3 B-mode imaging of the deep tissue and organs.

Besides monitoring the modulus of deep tissue and organs, the stretchable and wearable ultrasonic transducer array can be used for B-mode imaging applications, which can visualize the anatomic structure of the tissue and organs. In order to fully demonstrate the imaging capability of the device, we select tissues at different depth as the targets. Abdominal aorta and liver, which are located at ~5 cm and ~9 cm underneath the skin respectively, are imaged by the stretchable ultrasonic device.

As seen in Figure 66, the abdominal aorta from the longitudinal view has been shown. After rotating 90 degrees of the device, the aorta from the cross view is shown (Fig. 67). From the images below, we can clearly see the structure of multiple tissues, such as abdominal aorta, interior vena cava, and spine. To further verify the image quality, we use a commercial ultrasonic probe (Verasonics, P4-2v) to do the imaging at the same body location. The verified images have been put side by side to the images from the stretchable ultrasonic probe. The verified images match those images from the stretchable ultrasonic probes. Liver is another target organ that is used to verify the imaging capability of the stretchable ultrasonic device. As seen in Figure 68, the details in liver, such as the boundary, hepatic vein, and aorta, are clearly displayed. The verified image from the commercial ultrasonic probe has also been taken, which are highly comparable with the image from the stretchable ultrasonic probe. Achieving B-mode imaging through the wearable ultrasonic patch provides the feasibility for the continuous monitoring of human vital signs, diagnosis of acute diseases, and imaging-guided surgeries.

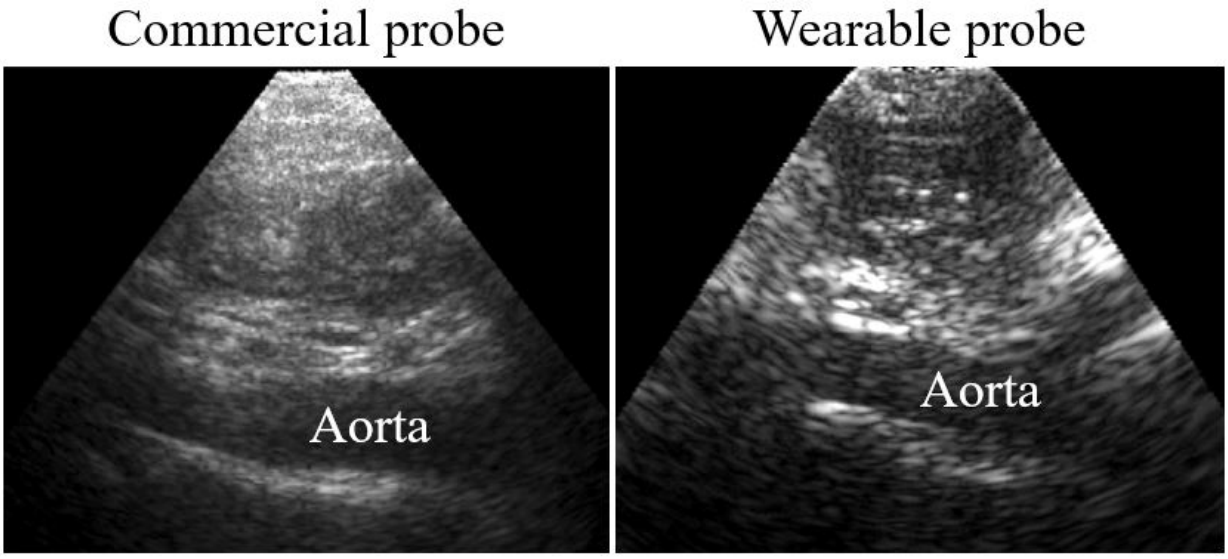

Figure 66. B-mode images of abdominal aorta from longitudinal view from both commercial and wearable ultrasonic probes.

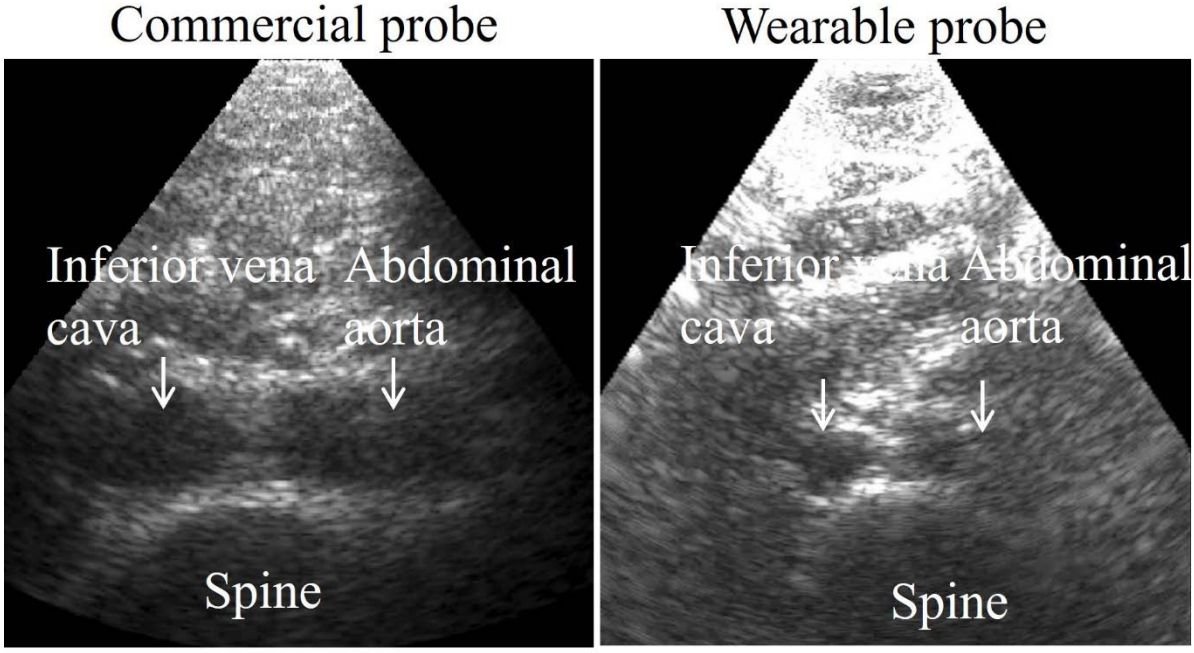

Figure 67. B-mode images of abdominal aorta from cross view from both commercial and wearable ultrasonic probes.

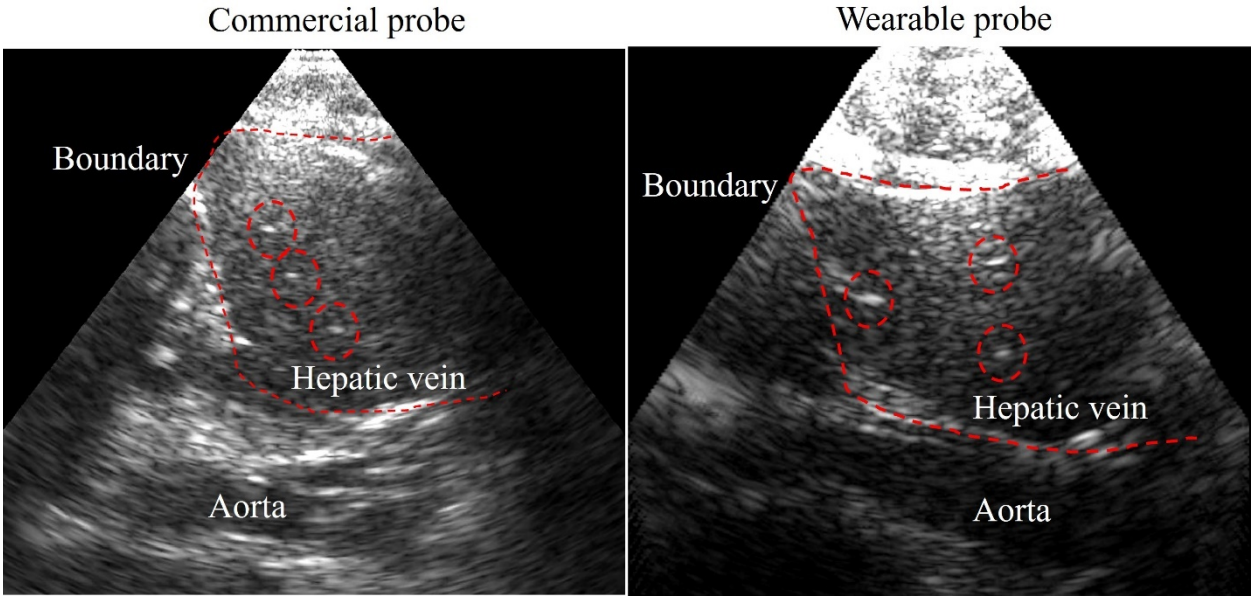

Figure 68. **B-mode images of liver from both commercial and wearable ultrasonic probes.**

4.4 Conclusion

In this chapter, we have demonstrated the applications of the wearable and stretchable ultrasonic array for monitoring of human vital signs. The stretchable ultrasonic array is able to perform serial, non-invasive 3D mapping of the blood pressure waveform, mechanical properties, and anatomical structure of deep tissues, which has yet to be realized by any existing diagnosis devices. Collectively, these achievements clearly demonstrate that the stretchable ultrasonic array is potentially complementary to existing clinical monitoring modalities and can be used as a unique platform technology for sensing and treatment monitoring.

Chapter four, in full, is a partial reprint of the materials: ‘Monitoring of the central blood pressure waveform via a conformal ultrasonic device, Wang, C., Li, X., Hu, H., Zhang, L., Huang, Z., Lin, M., Zhang, Z., Yin, Z., Huang, B., Gong, H., Bhaskaran, S., Gu, Y., Makihata, M., Guo,

Y., Lei, Y., Chen, Y., Wang, C., Li, Y., Zhang, T., Chen, Z., Pisano, A., Zhang, L., Zhou, Q., Xu, S., Nature biomedical engineering 2.9 (2018): 687-695'; 'Three-dimensional mapping of deep tissue modulus by stretchable ultrasonic arrays, Hu, H., Ma, Y., Gao, X., Song, D., Li, M., Huang, H., Qian, X., Shi, K., Ding, H., Lin, M., Chen, X., Zhao, W., Qi, B., Zhou, Sai; Chen, R., Gu, Y., Chen, Y., Lei, Y., Wang, C., Wang, C., Tong, Y., Cui, H., Zhu, Y., Tian, X., Chen, Z., Lu, C., Eghtedari, M., Zhou, Q., Oberai, A., Xu, S., Submitted'. The dissertation author was the co-first author of these papers.

Chapter 5. Summary

Throughout the time in Professor Xu's group as a graduate student, I have worked towards making significant contributions in the wearable and stretchable ultrasonic array and its related characterizations and applications. Our contributions are substantial, as summarizing below.

In Chapter One, the introduction of the stretchable ultrasonic device and the current problems presented in this field has been introduced and discussed. Currently, ultrasound probes with flat bases have been created to successfully accommodate different components of planar surfaces. However, these rigid probes cannot achieve a solid interfacial contact and therefore good coupling with irregular nonplanar surfaces, which are ubiquitous in real objects. Recent efforts have focused on developing flexible ultrasonic probes, but those drawbacks represent a bottleneck for the development of advanced probes that combine excellent ultrasonic performance with desirable mechanical properties that allow for application to general complex surfaces. Therefore, we report the first stretchable ultrasonic transducer arrays for different applications.

In Chapter Two, the acoustic and mechanical properties of the device will be introduced. Specifically, the electrical impedance spectrum, resonant and anti-resonant frequencies, phase angle, bandwidth, crosstalk, insertion loss, sensitivity are characterized. The biaxial stretchability of the transducer array has been quantitatively demonstrated. The elastographic performances of the transducer array, including the signal to noise ratio, contrast to noise ratio, compounding angle step, angle number, spatial resolutions, and dynamic range, are characterized.

In Chapter Three, we report the application of the stretchable ultrasonic array for nondestructive evaluation. The stretchable ultrasound probe, consisting of a 10 × 10 array of individually addressable transducer elements, can focus at different depths, with comparable spatial resolutions with existing rigid probes. Its performance has been demonstrated by reconstructing defects in 2D and 3D space with high spatial resolution through flat, concave, and convex surfaces.

In Chapter Four, we report the demonstration of the stretchable ultrasonic device on human body testing. The blood pressure waveform, deep-tissue moduli and anatomical structures are monitored by the stretchable and wearable ultrasonic array, which should facilitate its use in a variety of clinical environments.

In conclusion, we systematically study the current challenges in the ultrasonic field, from which we generated the idea of developing the wearable and stretchable ultrasonic array. Then, we did the rigorous characterizations from multiple aspects. Finally, we implemented our device into the real medical cases to monitor the blood pressure waveform, tissue stiffness, and anatomical structure. Therefore, we conclude that our research significantly advances the ultrasonic inspection and the sensing depth of wearable electronics.

References

1 Lowe, M. J., Alleyne, D. N. & Cawley, P. Defect detection in pipes using guided waves. *Ultrasonics* **36**, 147-154(1998).

2 Drinkwater, B. W. & Wilcox, P. D. Ultrasonic arrays for non-destructive evaluation: A review. *NDT & e International* **39**, 525-541(2006).

3 Casula, O., Poidevin, C., Cattiaux, G. & Dumas, P. in *AIP Conf. Proc.* 829-836 (American Institute of Physics).

4 Schmerr, L. W. in *Fundamentals of Ultrasonic Nondestructive Evaluation* 1-13 (Springer, 2016).

5 Pilkey, W. D., Pilkey, D. F. & Bi, Z. *Peterson's stress concentration factors*. (John Wiley & Sons, 2020).

6 Xiao, H., Sun, Y., Chen, D. & Xu, J. Prediction of flat-bottom hole signals received by a spherically focused transducer for an ultrasonic pulse echo immersion testing. *Measurement Science and Technology* **27**, 115001(2016).

7 Long, R. & Cawley, P. in *AIP Conf. Proc.* 754-761 (American Institute of Physics).

8 Jasiūnienė, E., Raišutis, R., Šliteris, R., Voleišis, A. & Jakas, M. Ultrasonic NDT of wind turbine blades using contact pulse-echo immersion testing with moving water container. *Ultragarsas* **63**, 28-32(2008).

9 Lane, C. J. The inspection of curved components using flexible ultrasonic arrays and shape sensing fibres. *Case Stud. Nondestr.Test. Eval.* **1**, 13-18(2014).

10 Chatillon, S., Cattiaux, G., Serre, M. & Roy, O. Ultrasonic non-destructive testing of pieces of complex geometry with a flexible phased array transducer. *Ultrasonics* **38**, 131-134(2000).

11 Powell, D. & Hayward, G. Flexible ultrasonic transducer arrays for nondestructive evaluation applications. II. Performance assessment of different array configurations. *IEEE Trans. Ultrason. Ferroelectr. Freq. Control* **43**, 393-402(1996).

12 Qi, Y., Jafferis, N, Lyons, K, Lee, C, Ahmad, H, & McAlpine, Piezoelectric ribbons printed onto rubber for flexible energy conversion. *Nano letters* **10**, 524-528(2010).

13 Harvey, G., Gachagan, A., Mackersie, J. W., Mccunnie, T., & Banks, R. Flexible ultrasonic transducers incorporating piezoelectric fibres. *IEEE Trans. Ultrason. Ferroelectr. Freq. Control* **56**, 1999-2009(2009).

14 Wang, Z., Xue, Q., Chen, Y., Shu, Y., Tian, H., Yang, Y., Xie, D., Luo, J., & Ren, T., A flexible ultrasound transducer array with micro-machined bulk PZT. *Sensors* **15**, 2538-2547(2015).

15 Zhuang, X., Lin, D.-S., Oralkan, O. & Khuri-Yakub, B. T. in *2007 IEEE 20th International Conference on Micro Electro Mechanical Systems (MEMS).* 73-76 (IEEE).

16 Mineo, C., Macleod, C., Morozov, M., Pierce, G., Summan, R., Rodden, T., Kahani, D., Powell, J., McCubbin, P., McCubbin, C., Munro, G., Paton, S., & Watson, D., in *AIP Conf. Proc.* 020026 (AIP Publishing LLC).

17 Pang, D.-C. & Chang, C.-M. Development of a novel transparent flexible capacitive micromachined ultrasonic transducer. *Sensors* **17**, 1443(2017).

18 Li, Z., Chen, A. I., Wong, L. L., Na, S. & Yeow, J. T. in *2015 IEEE International Ultrasonics Symposium (IUS).* 1-4 (IEEE).

19 Qiu, Y., Gigliotti, J., Wallace., M., Griggio., F., Demore., C., Cochran., S., & Trolier-McKinstry, S., Piezoelectric micromachined ultrasound transducer (PMUT) arrays for integrated sensing, actuation and imaging. *Sensors* **15**, 8020-8041(2015).

20 Lee, J, Il-Joo C, Kyungmin K, Yoon, E., Park, H., and Kim, T., Flexible piezoelectric micromachined ultrasonic transducer (pMUT) for application in brain stimulation. *Microsystem Technologies* **23**, no. 7 (2017): 2321-2328.

21 Duval, F. F., Dorey, R. A., Wright, R. W., Huang, Z. & Whatmore, R. W. Fabrication and modeling of high-frequency PZT composite thick film membrance resonators. *IEEE Trans. Ultrason. Ferroelectr. Freq. Control* **51**, 1255-1261(2004).

22 Bowen, C., Bradley, L., Almond, D. & Wilcox, P. Flexible piezoelectric transducer for ultrasonic inspection of non-planar components. *Ultrasonics* **48**, 367-375(2008).

23 Pashaei, V., Parisa D., George E., Mahdi B., Steve J., and Soumyajit M., Flexible body-conformal ultrasound patches for image-guided neuromodulation. *IEEE transactions on biomedical circuits and systems* **14**, no. 2 (2019): 305-318.

24 Kato, Y., Sekitani, T., Noguchi, Y., Yokota, T., Takamiya, M., Sakurai, T., and Someya, T., Large-area flexible ultrasonic imaging system with an organic transistor active matrix. *IEEE Transactions on Electron Devices* **57**, no. 5 (2010): 995-1002.

25 Wang, C., Qi, B., Lin, M., Zhang, Z., Makihata, M., Liu, B., Zhou, S., Huang, Y., Hu, H., Gu, Y., Chen, Y., Lei, Y., Lee, T., Chien, S., Jang, K., Kistler, E., & Xu, S., Continuous monitoring of deep-tissue haemodynamics with stretchable ultrasonic phased arrays. *Nature Biomedical Engineering* **5**, no. 7 (2021): 749-758.

26 Gao, X.,, Chen, X., Hu, H., Wang, X., Mu, J., Lou, Z., Zhang, R., Shi, K., Yue, W., Chen, X., Lin, M., Qi, B., Zhou, S., Lu, C., Gu, Y., Ding, H., Zhu, Y., Huang, H., Ma, Y., Li, M., Mishra, A., & Xu, S., A photoacoustic patch for three-dimensional imaging of hemoglobin and core temperature. (2021).

27 Wang, C., Li, X., Hu, H., Zhang, L., Huang, Z., Lin, M., Zhang, Z., Yin, Z., Huang, B., Gong, H., Bhaskaran, S., Gu, Y., Makihata, M., Guo Y., Lei, Y., Chen, Y., Wang, C., Li, Y., Zhang, T., Chen, Z., Pisano, A., Zhang, L., Zhou, Q., and Xu, S., Monitoring of the central blood pressure waveform via a conformal ultrasonic device. *Nature biomedical engineering* **2**, no. 9 (2018): 687-695.

28 Hu, H., Zhu, X., Wang, C., Zhang, L., Li, X., Lee, S., Huang, Z., Chen, R., Chen, Z., Wang, C. and Gu, Y., Chen, Y., Lei, Y., Zhang, T., Kim, N., Guo, Y., Teng, Y., Zhou, W., Li, Yang., Nomoto, A., Sternini, S., Zhou, Q., Pharr, M., Lanza di Scalea, F., & Xu, S., 2018. Stretchable ultrasonic transducer arrays for three-dimensional imaging on complex surfaces. *Science advances*, ***4***(3), p.eaar3979.

29 Ceh, D., Peters, T. M. & Chen, E. C. in *Medical Imaging 2015: Physics of Medical Imaging.* 94123G (International Society for Optics and Photonics).

30 Gu, X., Yang, Y., Chen, J. & Wang, Y. Temperature-dependent properties of a 1-3 connectivity piezoelectric ceramic-polymer composite. *Energy Harvesting and Systems* **2**, 107-112(2015).

31 Shung, K. K. *Diagnostic ultrasound: Imaging and blood flow measurements*. 1-232 (CRC press, Boca Raton, 2005).

32 Hatfield, J.V., Scales, N.R., Armitage, A.D., Hicks, P.J., Chen, Q.X. and Payne, P.A., An integrated multi-element array transducer for ultrasound imaging. *Sens. Actuators, A* **41**, 167-173(1994).

33 Payne, P.A., Hatfield, J.V., Armitage, A.D., Chen, Q.X., Hicks, P.J. and Scales, N., in *1994 Proceedings of IEEE Ultrasonics Symposium.* 1523-1526 (IEEE).

34 Liu, C., Djuth, F., Li, X., Chen, R., Zhou, Q. & Shung, K.K., Micromachined high frequency PMN-PT/epoxy 1-3 composite ultrasonic annular array. *Ultrasonics* **52**, 497-502(2012).

35 Guo, L. & DeWeerth, S. P. High-density stretchable electronics: toward an integrated multilayer composite. *Adv. Mater. (Weinheim, Ger.)* **22**, 4030-4033(2010).

36 Xu, S., Zhang, Y., Jia, L., Mathewson, K.E., Jang, K.I., Kim, J., Fu, H., Huang, X., Chava, P., Wang, R., Bhole, S., Wang, L., Na, Y., Guan, Y., Flavin, M., Han, Z., Huang, Y., Rogers, J., Soft microfluidic assemblies of sensors, circuits, and radios for the skin. *Science* **344**, 70-74(2014).

37 Kabiri Ameri, S., Ho, R., Jang, H., Tao, L., Wang, Y., Wang, L., Schnyer, D.M., Akinwande, D. & Lu, N., Graphene electronic tattoo sensors. *ACS Nano* **11**, 7634-7641(2017).

38 Arndt, J. O., Klauske, J. & Mersch, F. The diameter of the intact carotid artery in man and its change with pulse pressure. *Pflüger's Archiv für die gesamte Physiologie des Menschen und der Tiere* **301**, 230-240(1968).

39 Zhou, Q., Lam, K. H., Zheng, H., Qiu, W. & Shung, K. K. Piezoelectric single crystal ultrasonic transducers for biomedical applications. *Prog. Mater Sci.* **66**, 87-111(2014).

40 Goenezen, S., Dord, J.F., Sink, Z., Barbone, P.E., Jiang, J., Hall, T.J. & Oberai, A.A., Linear and nonlinear elastic modulus imaging: an application to breast cancer diagnosis. *IEEE transactions on medical imaging* **31**, 1628-1637(2012).

41 Pellot-Barakat, C., Frouin, F., Insana, M. F. & Herment, A. Ultrasound elastography based on multiscale estimations of regularized displacement fields. *IEEE transactions on medical imaging* **23**, 153-163(2004).

42 Jiang, J. & Hall, T. J. A coupled subsample displacement estimation method for ultrasound-based strain elastography. *Phys. Med. Biol.* **60**, 8347(2015).

43 Kallel, F. & Ophir, J. A least-squares strain estimator for elastography. *Ultrason. Imaging* **19**, 195-208(1997).

44 Cloostermans, M. & Thijssen, J. A beam corrected estimation of the frequency dependent attenuation of biological tissues from backscattered ultrasound. *Ultrason. Imaging* **5**, 136-147(1983).

45 Bader, K. B., Crowe, M. J., Raymond, J. L. & Holland, C. K. Effect of frequency-dependent attenuation on predicted histotripsy waveforms in tissue-mimicking phantoms. *Ultrasound Med. Biol.* **42**, 1701-1705(2016).

46 Shung, K. K. *Diagnostic ultrasound: Imaging and blood flow measurements*. (CRC press, 2015).

47 Mi, X., Qin, L., Liao, Q. & Wang, L. Electromechanical coupling coefficient and acoustic impedance of 1-1-3 piezoelectric composites. *Ceramics International* **43**, 7374-7377(2017).

48 Haller, M. & Khuri-Yakub, B. Micromachined 1–3 composites for ultrasonic air transducers. *Review of scientific instruments* **65**, 2095-2098(1994).

49 Chen, R., Jiang, L., Zhang, T., Matsuoka, T., Yamazaki, M., Qian, X., Lu, G., Safari, A., Zhu, J., Shung, K.K., Ma, T., & Zhou, Q., Eco-Friendly Highly Sensitive Transducers Based on a New KNN–NTK–FM Lead-Free Piezoelectric Ceramic for High-Frequency Biomedical Ultrasonic Imaging Applications. *IEEE Transactions on Biomedical Engineering* **66**, 1580-1587(2018).

50 Arumugam, V., Naresh, M. D. & Sanjeevi, R. Effect of Strain-Rate on the Fracture-Behavior of Skin. *J. Biosci.* **19**, 307-313(1994).

51 Zhou, Q., Xu, X., Gottlieb, E.J., Sun, L., Cannata, J.M., Ameri, H., Humayun, M.S., Han, P. & Shung, K.K., PMN-PT single crystal, high-frequency ultrasonic needle transducers for pulsed-wave Doppler application. *IEEE Trans. Ultrason. Ferroelectr. Freq. Control* **54**, 668-675(2007).

52 Wang, Y., Zhang, Q., Zhao, L. & Kim, E.S., in *2011 IEEE 24th International Conference on Micro Electro Mechanical Systems.* 1035-1038 (IEEE).

53 Cochran, S., Demore, C. & Courtney, C. in *Ultrasonic Transducers* 187-219 (Elsevier, 2012).

54 Kobayashi, M., Jen, C.-K. & Levesque, D. Flexible ultrasonic transducers. *IEEE Trans. Ultrason. Ferroelectr. Freq. Control* **53**, 1478-1486(2006).

55 Cannata, J. M., Williams, J. A., Zhou, Q., Ritter, T. A. & Shung, K. K. Development of a 35-MHz piezo-composite ultrasound array for medical imaging. *IEEE Trans. Ultrason. Ferroelectr. Freq. Control* **53**, 224-236(2006).

56 Chen, Z., Zheng, L., Cao, W., Chen, X., Chen, R., Li, R., Shung, K. & Zhou, Q., High-frequency ultrasonic imaging with lead-free (Na, K)(Nb, Ta) O3 single crystal. *Ultrason. Imaging* **39**, 348-356(2017).

57 Matrone, G., Ramalli, A., Savoia, A. S., Tortoli, P. & Magenes, G. High frame-rate, high resolution ultrasound imaging with multi-line transmission and filtered-delay multiply and sum beamforming. *IEEE transactions on medical imaging* **36**, 478-486(2016).

58 Yiu, B. Y., Tsang, I. K. & Alfred, C. GPU-based beamformer: Fast realization of plane wave compounding and synthetic aperture imaging. *IEEE Trans. Ultrason. Ferroelectr. Freq. Control* **58**, 1698-1705(2011).

59 Frazier, C. H. & O'Brien, W. D. Synthetic aperture techniques with a virtual source element. *IEEE Trans. Ultrason. Ferroelectr. Freq. Control* **45**, 196-207(1998).

60 Medina-Valdes, L., Camacho, J., González-Salido, N. & Cruza, J. Resolution of image compounding with a ring array transducer. *Physics Procedia* **63**, 141-146(2015).

61 Secor, E. B., Prabhumirashi, P. L., Puntambekar, K., Geier, M. L. & Hersam, M. C. Inkjet printing of high conductivity, flexible graphene patterns. *The journal of physical chemistry letters* **4**, 1347-1351(2013).

62 Rotenberg, M. Y. & Tian, B. Bioelectronic devices: Long-lived recordings. *Nat. Biomed. Eng.* **1**, 1-2(2017).

63 Kaltenbrunner, M., Sekitani, T., Reeder, J., Yokota, T., Kuribara, K., Tokuhara, T., Drack, M., Schwödiauer, R., Graz, I., Bauer-Gogonea, S., Bauer, S., & Someya T., An ultra-lightweight design for imperceptible plastic electronics. *Nature* **499**, 458-463(2013).

64 Xu, S., Zhang, Y., Cho, J., Lee, J., Huang, X., Jia, L., Fan, J.A., Su, Y., Su, J., Zhang, H., Cheng, H., Lu, B., Yu, C., Chuang, C., Kim, T., Song, T., Shigeta, K., Kang, S., Dagdeviren, C., Petrov, I., Braun, P., Huang, Y., Paik, U., Rogers, J., Stretchable batteries with self-similar serpentine interconnects and integrated wireless recharging systems. *Nature communications* **4**, 1-8(2013).

65 Huang, X., Liu, Y., Kong, G.W., Seo, J.H., Ma, Y., Jang, K.I., Fan, J.A., Mao, S., Chen, Q., Li, D., Liu, H., Wang, C., Patnaik, D., Tian, L., Salvatore, G., Feng, X., Ma, Z., Huang, Y., Rogers, J., Epidermal radio frequency electronics for wireless power transfer. *Microsyst. Nanoeng.* **2**, 1-9(2016).

66 Hussain, A.M., Ghaffar, F.A., Park, S.I., Rogers, J.A., Shamim, A. & Hussain, M.M., Metal/polymer based stretchable antenna for constant frequency far-field communication in wearable electronics. *Advanced Functional Materials* **25**, 6565-6575(2015).

67 Pan, T., Pharr, M., Ma, Y., Ning, R., Yan, Z., Xu, R., Feng, X., Huang, Y. & Rogers, J.A., Experimental and theoretical studies of serpentine interconnects on ultrathin elastomers for stretchable electronics. *Advanced Functional Materials* **27**, 1702589(2017).

68 Montaldo, G., Tanter, M., Bercoff, J., Benech, N. & Fink, M. Coherent plane-wave compounding for very high frame rate ultrasonography and transient elastography. *IEEE Trans. Ultrason. Ferroelectr. Freq. Control* **56**, 489-506(2009).

69 Wang, Y., Bayer, M., Jiang, J. & Hall, T. J. Large-strain 3-D in vivo breast ultrasound strain elastography using a multi-compression strategy and a whole-breast scanning system. *Ultrasound Med. Biol.* **45**, 3145-3159(2019).

70 Céspedes, I. & Ophir, J. Reduction of image noise in elastography. *Ultrason. Imaging* **15**, 89-102(1993).

71 Varghese, T. & Ophir, J. An analysis of elastographic contrast-to-noise ratio. *Ultrasound Med. Biol.* **24**, 915-924(1998).

72 Qian, X., Ma, T., Yu, M., Chen, X., Shung, K.K. & Zhou, Q., Multi-functional ultrasonic micro-elastography imaging system. *Sci. Rep.* **7**, 1-11(2017).

73 Kennedy, K.M., Chin, L., McLaughlin, R.A., Latham, B., Saunders, C.M., Sampson, D.D. & Kennedy, B.F., Quantitative micro-elastography: imaging of tissue elasticity using compression optical coherence elastography. *Sci. Rep.* **5**, 15538(2015).

74 Hunter, A. J., Drinkwater, B. W., Wilcox, P. & Russell, J. in *8th International Conference on NDE in Relation to Structural Integrity for Nuclear and Pressurised Components, Berlin, Germany.* (Citeseer).

75 Mariani, S., Nguyen, T., Zhu, X. & Lanza di Scalea, F. Field test performance of noncontact ultrasonic rail inspection system. *Journal of Transportation Engineering, Part A: Systems* **143**, 04017007(2017).

76 Cruza, J., Camacho, J. & Fritsch, C. Plane-wave phase-coherence imaging for NDE. *NDT & E International* **87**, 31-37(2017).

77 Trudeau, L. Central blood pressure as an index of antihypertensive control: determinants and potential value. *Can. J. Cardiol.* **30**, S23-S28(2014).

78 Mukkamala, R. & Xu, D. Continuous and less invasive central hemodynamic monitoring by blood pressure waveform analysis. *American Journal of Physiology-Heart and Circulatory Physiology* **299**, H584-H599(2010).

79 Camacho, F., Avolio, A. & Lovell, N. Estimation of pressure pulse amplification between aorta and brachial artery using stepwise multiple regression models. *Physiological measurement* **25**, 879(2004).

80 Williams, B., Lacy, P.S., Thom, S.M., Cruickshank, K., Stanton, A., Collier, D., Hughes, A.D., Thurston, H. & O'Rourke, M., Differential impact of blood pressure–lowering drugs on central aortic pressure and clinical outcomes: principal results of the Conduit Artery Function Evaluation (CAFE) study. *Circulation* **113**, 1213-1225(2006).

81 Shirwany, N. A. & Zou, M.-h. Arterial stiffness: a brief review. *Acta Pharmacologica Sinica* **31**, 1267-1276(2010).

82 Ding, H., Akhbari, S., Eovino, B.E., Wu, Y., Xie, J. and Lin, L., in *2018 IEEE Micro Electro Mechanical Systems (MEMS).* 396-399 (IEEE).

83 Illomei, G., Spinicci, G., Locci, E. & Marrosu, M. Muscle elastography: a new imaging technique for multiple sclerosis spasticity measurement. *Neurol. Sci.* **38**, 433-439(2017).

84 Brandenburg, J.E., Eby, S.F., Song, P., Kingsley-Berg, S., Bamlet, W., Sieck, G.C., & An, K.N., Quantifying passive muscle stiffness in children with and without cerebral palsy using ultrasound shear wave elastography. *Dev. Med. Child Neurol.* **58**, 1288-1294(2016).

85 Dietrich, C.F., Barr, R.G., Farrokh, A., Dighe, M., Hocke, M., Jenssen, C., Dong, Y., Saftoiu, A. & Havre, R.F. Strain elastography-how to do it? *Ultrasound international open* **3**, E137(2017).

86 Taylor, K., O'Keeffe, S., Britton, P.D., Wallis, M.G., Treece, G.M., Housden, J., Parashar, D., Bond, S. & Sinnatamby, R., Ultrasound elastography as an adjuvant to conventional

ultrasound in the preoperative assessment of axillary lymph nodes in suspected breast cancer: a pilot study. *Clinical radiology* **66**, 1064-1071(2011).

87 DeWall, R. J. Ultrasound elastography: principles, techniques, and clinical applications. *Crit. Rev. Biomed. Eng.* **41**, 1-19(2013).

88 Krouskop, T. A., Wheeler, T. M., Kallel, F., Garra, B. S. & Hall, T. Elastic moduli of breast and prostate tissues under compression. *Ultrason. Imaging* **20**, 260-274(1998).

89 Lopata, R.G., Nillesen, M.M., Hansen, H.H., Gerrits, I.H., Thijssen, J.M. and De Korte, C.L., Performance evaluation of methods for two-dimensional displacement and strain estimation using ultrasound radio frequency data. *Ultrasound Med. Biol.* **35**, 796-812(2009).

90 Hÿtch, M., Snoeck, E. & Kilaas, R. Quantitative measurement of displacement and strain fields from HREM micrographs. *Ultramicroscopy* **74**, 131-146(1998).

91 Papadacci, C., Bunting, E. A. & Konofagou, E. E. 3D quasi-static ultrasound elastography with plane wave in vivo. *IEEE transactions on medical imaging* **36**, 357-365(2016).

92 Hayakawa, M., Hatano, T., Tsuji, A., Nakajima, F. & Ogawa, Y. Patients with renal cysts associated with renal cell carcinoma and the clinical implications of cyst puncture: a study of 223 cases. *Urology* **47**, 643-646(1996).

93 Sigrist, R. M., Liau, J., El Kaffas, A., Chammas, M. C. & Willmann, J. K. Ultrasound elastography: review of techniques and clinical applications. *Theranostics* **7**, 1303(2017).

94 Oberai, A. A., Gokhale, N. H. & Feijóo, G. R. Solution of inverse problems in elasticity imaging using the adjoint method. *Inverse Prob.* **19**, 297(2003).

95 Ferreira, E. R., Oberai, A. A. & Barbone, P. E. Uniqueness of the elastography inverse problem for incompressible nonlinear planar hyperelasticity. *Inverse Prob.* **28**, 065008(2012).

96 Song, D., Hugenberg, N. & Oberai, A. A. Three-dimensional traction microscopy with a fiber-based constitutive model. *Computer Methods in Applied Mechanics and Engineering* **357**, 112579(2019).

97 Yu, X., Wang, H., Ning, X., Sun, R., Albadawi, H., Salomao, M., Silva, A.C., Yu, Y., Tian, L., Koh, A., Lee, C.M., Chempakasseril, A., Tian, P., Pharr, M., Yuan, J., Huang, Y., Oklu, R., Rogers, J., Needle-shaped ultrathin piezoelectric microsystem for guided tissue targeting via mechanical sensing. *Nat. Biomed. Eng* **2**, 165-172(2018).

98 Risholm, P., Ross, J., Washko, G. R. & Wells, W. M. in *Biennial International Conference on Information Processing in Medical Imaging*. 699-710 (Springer).

99 Gokhale, N. H., Barbone, P. E. & Oberai, A. A. Solution of the nonlinear elasticity imaging inverse problem: the compressible case. *Inverse Prob.* **24**, 045010(2008).

100 Francois Dord, J., Goenezen, S., Oberai, A.A., Barbone, P.E., Jiang, J., Hall, T.J. & Pavan, T., Validation of quantitative linear and nonlinear compression elastography. *Ultrasound Elastography for Biomedical Applications and Medicine*, 129-142(2018).

101 Brouwer, I., Ustin, J., Bentiey, L., Dhruv, A. & Tendick, F. in *Medicine meets virtual reality*. 69 (IOS Press Amsterdam).

102 Van Houten, E. E., Doyley, M. M., Kennedy, F. E., Weaver, J. B. & Paulsen, K. D. Initial in vivo experience with steady-state subzone-based MR elastography of the human breast. *Journal of Magnetic Resonance Imaging: An Official Journal of the International Society for Magnetic Resonance in Medicine* **17**, 72-85(2003).

103 Xie, Y., Thomas, L., Hug, F., Johnston, V. & Coombes, B. K. Quantifying cervical and axioscapular muscle stiffness using shear wave elastography. *J. Electromyogr. Kinesiol.* **48**, 94-102(2019).

104 Ishiwatari, N., Fukuoka, M. & Sakai, N. Effect of protein denaturation degree on texture and water state of cooked meat. *Journal of Food Engineering* **117**, 361-369(2013).

105 Pearcey, G.E., Bradbury-Squires, D.J., Kawamoto, J.E., Drinkwater, E.J., Behm, D.G. & Button, D.C., Foam rolling for delayed-onset muscle soreness and recovery of dynamic performance measures. *J. Athl. Train.* **50**, 5-13(2015).

106 Hotfiel, T., Freiwald, J., Hoppe, M.W., Lutter, C., Forst, R., Grim, C., Bloch, W., Hüttel, M. & Heiss, R., Advances in delayed-onset muscle soreness (DOMS): Part I: Pathogenesis and diagnostics. *Sportverletzung· Sportschaden* **32**, 243-250(2018).

107 Kishimoto, K., Sakuraba, K., Kubota, A. & Fujita, S. The Effect of Concentric and Eccentric Exercise on Muscle Hardness. *Juntendo Medical Journal* **64**, 371-378(2018).

108 Niitsu, M., Michizaki, A., Endo, A., Takei, H. & Yanagisawa, O. Muscle hardness measurement by using ultrasound elastography: a feasibility study. *Acta Radiol.* **52**, 99-105(2011).

109 Murayama, M., Nosaka, K., Inami, T., Shima, N. & Yoneda, T. Biceps brachii muscle hardness assessed by a push-in meter in comparison to ultrasound strain elastography. *Sci. Rep.* **10**, 1-10(2020).

110 Lacourpaille, L., Nordez, A., Hug, F., Couturier, A., Dibie, C. & Guilhem, G., Time-course effect of exercise-induced muscle damage on localized muscle mechanical properties assessed using elastography. *Acta Physiologica* **211**, 135-146(2014).

111 Peake, J. M., Neubauer, O., Della Gatta, P. A. & Nosaka, K. Muscle damage and inflammation during recovery from exercise. *J. Appl. Physiol.* **122**, 559-570(2017).

112 Nelson, N. Delayed onset muscle soreness: is massage effective? *Journal of bodywork and movement therapies* **17**, 475-482(2013).

113 Lippold, O. in *Ciba Found. Symp.* 234-248 (Wiley Online Library).